

**IDENTIFICATION AND CHARACTERIZATION OF TRAPS IN
InGaAs SHORT WAVELENGTH INFRARED PHOTODETECTORS BY DEEP
LEVEL TRANSIENT SPECTROSCOPY**

A THESIS SUBMITTED TO
THE GRADUATE SCHOOL OF NATURAL AND APPLIED SCIENCES
OF
THE MIDDLE EAST TECHNICAL UNIVERSITY

BY

NARDIN AVISHAN

IN PARTIAL FULFILLMENT OF THE REQUIREMENTS
FOR
THE DEGREE OF MASTER OF SCIENCE
IN
ELECTRICAL AND ELECTRONICS ENGINEERING

MAY 2016

Approval of the thesis:

**IDENTIFICATION AND CHARACTERIZATION OF TRAPS IN
InGaAs SHORT WAVELENGTH INFRARED PHOTODETECTORS BY
DEEP LEVEL TRANSIENT SPECTROSCOPY**

submitted by **NARDIN AVISHAN** in partial fulfillment of the requirements for the degree of **Master of Science in Electrical and Electronics Engineering Department, Middle East Technical University** by,

Prof. Dr. Gülbil Dural Ünver _____
Dean, Graduate School of **Natural and Applied Sciences**

Prof. Dr. Gönül Turhan Sayan _____
Head of Department, **Electrical and Electronics Eng.**

Prof. Dr. Cengiz Beşikci _____
Supervisor, **Electrical and Electronics Eng. Dept., METU**

Examining Committee Members:

Prof. Dr. Mehmet Parlak _____
Physics Dept., METU

Prof. Dr. Cengiz Beşikci _____
Electrical and Electronics Eng. Dept., METU

Assist. Prof. Dr. Selçuk Yerci _____
Micro and Nanotechnology. Dept., METU

Assist. Prof. Dr. Serdar Kocaman _____
Electrical and Electronics Eng. Dept., METU

Assist. Prof. Dr. Ali Kemal Okyay _____
Electrical and Electronics Eng. Dept., Bilkent Uni.

Date: 13/05/2016

I hereby declare that all information in this document has been obtained and presented in accordance with academic rules and ethical conduct. I also declare that, as required by these rules and conduct, I have fully cited and referenced all material and results that are not original to this work.

Name, Last name: Nardin Avishan

Signature:

ABSTRACT

IDENTIFICATION AND CHARACTERIZATION OF TRAPS IN InGaAs SHORT WAVELENGTH INFRARED PHOTODETECTORS BY-DEEP LEVEL TRANSIENT SPECTROSCOPY

Avishan, Nardin

M. S., Department of Electrical and Electronics Engineering

Supervisor: Prof. Dr. Cengiz Beşikci

May 2016, 108 pages

Unintentionally added impurities during the epitaxial growth and lattice defects may cause deep level traps in the bandgap of semiconductors. They can strongly affect the electrical and optical properties of semiconductors. Studying these energy levels and providing feedback to the material growth and device fabrication processes are important in order to identify the performance limiting mechanisms and optimize the characteristics of semiconductor devices. Deep Level Transient Spectroscopy (DLTS) technique is commonly used for this purpose. In this thesis, the electrical properties of traps in molecular beam epitaxy (MBE) grown $In_xGa_{1-x}As$ with In mole fractions (x) of 0.53 and 0.83 are identified and characterized. The epilayers were grown on InP substrate. One electron trap at $E_c - 0.33$ eV and one hole trap at $E_v + 0.15$ eV were detected in the lattice-matched $In_{0.53}Ga_{0.47}As/InP$ p-i-n photodiodes with different absorber doping densities. Two hole traps with energy levels of $E_v + 0.10$ eV and $E_v + 0.31$ eV were detected in the lattice-mismatched $In_{0.83}Al_{0.17}As/InP$ heterojunction p-i-n photodetector grown with a

linearly graded $\text{In}_x\text{Al}_{1-x}\text{As}$ buffer layer. The results were compared with the trap characteristics reflected by the G-R component of the dark current in the photodetectors fabricated with the epilayer structure and good agreement was obtained. The dominant trap degrading the detector characteristics was found to display extended defect characteristic with a capture cross section of $\sim 5.3 \times 10^{-16} \text{ cm}^2$, density of $1.8 \times 10^{15} \text{ cm}^{-3}$ and activation energy of 0.31 eV.

Keywords: InGaAs, Short Wavelength Infrared, Photodetector, DLTS, Deep Level Traps

ÖZ

InGaAs KISA DALGABOYU KIZİLÖTESİ FOTODEDEKTÖRLERDEKİ TUZAKLARIN DERİN SEVİYE GEÇİCİ SPEKTROSKOPİ YÖNTEMİYLE BELİRLENMESİ VE KARAKTERİZASYONU

Avishan, Nardin

Yüksek Lisans, Elektrik ve Elektronik Mühendisliği Bölümü

Tez Yöneticisi: Prof. Dr. Cengiz Beşikci

Mayıs 2016, 108 sayfa

Epitaksiyel büyütme sırasında malzemeye katılan amaç dışı safsızlık maddeleri ve örgü hataları yarı iletkenlerde derin seviye tuzaklarına yol açabilmektedir. Bu tuzaklar yarı iletkenlerin elektriksel ve optik özelliklerini önemli ölçüde etkileyebilmektedirler. Bu enerji seviyelerinin incelenip, malzeme büyütme ve aygit fabrikasyonu proseslerine geri besleme sağlanması yarı iletken aygitların performansını sınırlayan parametrelerin belirlenmesi ve karakteristiklerinin optimizasyonu açısından önemlidir. Derin Seviye Tranzient Spektroskopi (DLTS) tekniği bu amaçla yaygın olarak kullanılmaktadır. Bu tezde, moleküller ışın epitaksisi (MBE) ile büyütülmüş olup, 0.53 ve 0.83 In mol katsayılarına (x) sahip olan $\text{In}_x\text{Ga}_{1-x}\text{As}$ malzemesindeki tuzakların elektriksel karakteristikleri tespit ve karakterize edilmiştir. Epikatmanlar InP taban üzerinde büyütülmüştür. Değişik emici katman katkılama yoğunluklarına sahip olan örgü uyumlu $\text{In}_{0.53}\text{Ga}_{0.47}\text{As}/\text{InP}$ p-i-n

fotodiyotlarda enerji seviyeleri sırasıyla $E_c - 0.33$ eV ve $E_v + 0.15$ eV olan bir elektron ve bir delik tuzağı tespit edilmiştir. Kompozisyonu doğrusal değiştirilmiş $In_xAl_{1-x}As$ tampon katmanı ile büyütülen örgü uyumsuz $In_{0.83}Al_{0.17}As/In_{0.83}Ga_{0.17}As/InP$ heteroeklem p-i-n fotodedektörde ise enerji seviyeleri $E_v + 0.10$ eV ve $E_v + 0.31$ olan iki delik tuzağı gözlemlenmiştir. Bu sonuçlar bahis konusu epikatman yapısıyla fabrikasyonu yapılan fotodedektörün karanlık akımının G-R bileşeninin yansığı tuzak karakteristikleriyle karşılaştırılmış ve uyumlu oldukları tespit edilmiştir. Dedektör karakteristiklerini kötülestiren etkin tuzağın genişlemiş örgü hatası karakteristiği gösterdiği ve yakalama kesitinin, yoğunluğunun ve aktivasyon enerjisinin sırasıyla $\sim 5.3 \times 10^{-16} \text{ cm}^2$, $1.8 \times 10^{15} \text{ cm}^{-3}$ ve 0.31 eV olduğu bulunmuştur.

Anahtar Kelimeler: InGaAs, Kısa Dalgaboyu Kızılıötesi, Fotodedektör, DLTS, Derin Seviye Tuzakları

Dedicated to my parents for being the reason who I am today.

ACKNOWLEDGMENTS

First, I would like to express my sincere thanks to my supervisor Prof. Dr. Cengiz Beşikci for his excellent guidance and advice and for providing the motivation and support that I needed to accomplish this thesis. Thank you so much for believing in my abilities, supporting me, and making this journey such a great experience for me.

I would like to thank Assist. Prof. Dr. Serdar Kocaman for providing support and allocating the necessary resources. Thank you for your valuable insight and guidance.

I would like to express my sincere gratitude to Dr. Tahir Çolakoğlu and Fikri Oğuz for their support and help about using of DLTS setup. It was a great pleasure for me to work with them.

I would like to thank Halit Dolaş for fabrication and preparation of samples. I would like to thank him for his support and invaluable friendship.

I would like to thank Kübra Çırçır, Eray Yurtseven, Muammer Kozan for their friendships and their help when I stuck on a problem. And all the members in Quantum Devices and Nanophotonics Research Labrotory for their friendship.

My days in graduate school will not be complete without mentioning about my friends. I would like to thank Touraj Farsadi for his unlimited help and encouragement. I am also grateful to Ramona Davoudnezhad, Nasim Esmailzadeh, Parisa Sharif, Nardin Saboonchi and Aras Anari for their patience and support through thesis writing period.

I would also like to thank my Parents Mina and Hassan for their endless support and faith in me. They have always strived to provide all the means that were necessary for me to get the best education.

TABLE OF CONTENTS

ABSTRACT.....	v
ÖZ.....	vii
ACKNOWLEDGMENTS.....	x
TABLE OF CONTENT.....	xi
LIST OF TABLES.....	xiii
LIST OF FIGURES.....	xiv
CHAPTERS	
1. INTRODUCTION	1
1.1 Basis of Infrared Detection.....	2
1.2 Infrared Photon Detectors.....	6
1.2.1 Extrinsic Detectors.....	8
1.2.2 Intrinsic Detectors.....	8
1.2.3 Quantum Well and Superlattice Structures.....	11
1.3 Short Wavelength Infrared (SWIR) photodetectors	12
1.3.1 Germanium and Silicon SWIR PDs.....	15
1.3.2 Mercury Cadmium Telluride SWIR PDs.....	16
1.3.3 Indium Gallium Arsenide SWIR PDs.....	17
1.3.4 Extended Wavelength InGaAs SWIR Photodetectors	21
1.4 InGaAs SWIR Photodetector Structure.....	22
1.5 Deep Level Transient Spectroscopy (DLTS)	24
1.6 Outline of the Thesis	25
2. DEEP LEVEL TRANSIENT SPECTROSCOPY TECHNIQUE	27
2.1 Defects.....	28
2.2 Generation Recombination Process.....	30

2.2.1 Direct band-to-band recombination.....	31
2.2.2 Auger Band-to-Band Recombination	32
2.2.3 Shockley-Read-Hall Recombination	34
2.2.4 Surface Leakage	36
2.3 C-V measurement.....	37
2.4 Effect of Deep Level Traps on Junction Capacitance	38
2.5 Transient Capacitance Measurements	43
2.6 Principle of DLTS Measurement Method.....	49
2.7 Experimental Set-up.....	62
2.7.1 SULA DLTS.....	64
2.7.2 Temperature Control.....	66
2.7.3 Software Setup.....	67
3. Characterization of In _x Ga _{1-x} As SWIR Photodiodes	69
3.1 Sample Description	69
3.2 C-V Characterization.....	70
3.3 DLTS Measurements.....	72
3.4 DLTS Measurements on Lattice-matched In _{0.53} Ga _{0.47} As/InP Photodetectors .	74
3.5 Trap Characterization of Lattice-mismatched In _{0.83} Ga _{0.17} As Photodetectors ..	75
3.5.1 DLTS Measurements on Defected Material.....	76
3.5.2 Literature Survey on DLTS Measurements on Lattice Mismatched InGaAs80	
3.5.3 DLTS Measurement Results.....	82
3.6 I-V Characterization and Results	92
4. CONCLUSION AND FUTURE WORK	99
5. REFERENCES	101

LIST OF TABLES

TABLES

Table 1-1: Comparison of IR detector technologies [5].....	7
Table 3-1: Summary of the traps detected in samples S1 and S2	75
Table 3-2: Summary of the traps detected in samples S3 and S4.	88

LIST OF FIGURES

FIGURES

Figure 1-1: Electromagnetic spectrum [1].	2
Figure 1-2: Photon spectral exitance vs. wavelength curves of blackbodies at various temperatures [3].	5
Figure 1-3: Atmospheric transmission at sea level along a horizontal path of 2 km [4].....	6
Figure 1-4: CdS photoconductive detector cell schematic, diagram and operation circuit [8].....	9
Figure 1-5: Photovoltaic p-n diode (a) Structure and operation schematic and (b) I-V curve [9].....	10
Figure 1-6: Energy band diagram of a QWIP structure and intersubband transition of electrons in the well [11].....	11
Figure.1-7:.Type-II superlattice infrared photodetector band structure and the formation of artificial bandgap [11].....	12
Figure 1-8: comparison of SWIR and Visible imaging. (a) The SWIR image (left) shows ability of SWIR technology to detect the liquid levels in plastic bottles, which are opaque to the eye. The right image shows the visible image of the bottles. (b) The left image belongs to a hotel through a distance of 2.5 km in a foggy weather, taken by commercial visible camera; the right image belongs to the same place and condition, taken with a SWIR 640x512 pixel camera [13-14].	13

Figure 1-9: (a) The p-i-n diode diagram (b) energy band diagram under applied reverse bias (c) the profile of created electric field in p-i-n photodiode [15].	14
Figure 1-10: The relation between bandgap and cut-off wavelength of $\text{Si}_{1-x}\text{Ge}_x$ and Ge mole fraction [16].	15
Figure 1-11: MCT bandgap value for different mole fractions of CdTe [18].....	16
Figure 1-12: Lattice constant dependence on In mole fraction in $\text{In}_x\text{Ga}_{1-x}\text{As}$ [11]....	17
Figure 1-13: Cut-off wavelength value for different lattice constant values [21].....	18
Figure 1-14: Bandgap energy and cut-off wavelength dependence of $\text{In}_x\text{Ga}_{1-x}\text{As}$ on In mole fraction [11].	19
Figure 1-15: Contrasting the responsivity of $\text{In}_{0.53}\text{Ga}_{0.47}\text{As}$ and irradiant of night sky [25].	20
Figure 1-16: Comparison between responsivity spectra of $\text{In}_{0.53}\text{Ga}_{0.47}\text{As}$ photodetector before (blue plot) and after (yellow plot) elimination of the InP substrate [26].....	21
Figure 1-17: Epilayer structure of an $\text{In}_{0.53}\text{Ga}_{0.47}\text{As}$ photodetector.	23
Figure 1-18: Absorption (at 1.55 μm) by $\text{In}_{0.53}\text{Ga}_{0.47}\text{As}$ at different thicknesses [11].	23
Figure 2-1: Illustrating the difference between electron trap, hole trap and G-R center due to carrier capture probability [37].	30
Figure 2-2: Recombination mechanism of an electron hole pair with same wave vector [38].	32
Figure 2-3: Auger recombination process. The released energy due to electron recombination interacts with, A) an electron in conduction band and excited electron remains there, CHCC b) a hole in valence band and causes recombination of hole	

with an electron in LH band, CHLH c) a hole in valence band and causes recombination of hole with an electron in split-off band [38].	33
Figure 2-4: How a G-R center with E_T energy level acts within the bandgap [40] ..	34
Figure 2-5: Energy band diagram of a Schottky barrier with a donor level trap.....	39
Figure 2-6: a) Energy band diagram of a Schottky barrier with a donor trap level under reverse bias. b) Effect of the applied reverse bias on the electric field in depletion region [41].....	41
Figure 2-7: A Schottky diode for (a) zero bias (b) reverse bias at $t=0$, (c) reverse bias as $t \rightarrow \infty$.The applied voltage and resultant capacitance transient are shown in (d) [33].	44
Figure 2-8: Capacitance transient under thermal emission of carriers from majority carrier traps [33].....	46
Figure 2-9: Effects of saturating injection pulse on n ⁺ -p junction and minority carrier trap level [34].....	50
Figure 2-10: Effects of majority carrier pulse on n ⁺ -p junction and majority carrier trap level [34].....	51
Figure 2-11: Effect of temperature on capacitance transient time and speed [41]. ...	52
Figure 2-12: Rate window concept (basic idea of DLTS) [34].	53
Figure 2-13: Illustration of how a double boxcar is used to define the rate window [34].	54
Figure 2-14: DLTS spectra for (a) <i>t1</i> fixed, <i>t2</i> varied, (b) <i>t2</i> fixed, <i>t1</i> varied [33].	59
Figure 2-15: Typical experimental DLTS spectra for hole traps in n-GaAs and five different emission rate windows achieved by varying values of <i>t1</i> and <i>t2</i> [34].	60
Figure 2-16: Arrhenius plot for traps detected in GaAs. (Thermal emission rate with respect to temperature) [34].	61

Figure 2-17: Block diagram of a DLTS system [36].	63
Figure 2-18: Set-up used for DLTS measurements [43].	64
Figure 2-19: Schematic of SULA DLTS equipment [42].	65
Figure 2-20: Closed cycle cryostat.....	67
Figure 3-1: Structure details for lattice-mismatched $\text{In}_{0.83}\text{Ga}_{0.17}\text{As}$ SWIR photodiodes S3 and S4.	70
Figure 3-2: C-V characteristic for S3.....	71
Figure 3-3: C-V characteristic for S4 (majority carrier concentration and built-in voltage are obtained from 1/C₂-V_{bias} plot).	72
Figure 3-4: DLTS spectra for $\text{GaAs}_{0.74}\text{P}_{0.26}:\text{EL2}$ trap, illustrating the effect of S factor for a deep level trap with $E_a=0.92\text{eV}$ [56].	78
Figure 3-5: Theoretical fit to the experimental DLTS spectra for a dislocation defect in plastically deformed n-type Silicon with different dislocation densities [58].	79
Figure 3-6: DLTS spectra for S3 (the plot illustrates two minority trap levels).....	82
Figure 3-7: a) DLTS spectra for S3, b) Arrhenius plot and the properties of the observed minority carrier trap in sample S3.	84
Figure 3-8: DLTS spectra for deep level trap due to dislocation defects.....	84
Figure 3-9: Theoretical fit to the experimentally obtained DLTS spectra. Broadening factor S is different for each spectra.	85
Figure 3-10: a) DLTS spectra for S4, b) Arrhenius plot and the properties of the observed minority carrier trap in sample S4.	87
Figure 3-11: Amplitude of the DLTS peak point for the first hole trap in S3 versus filling pulse width.	89

Figure 3-12: Amplitude of the DLTS peak points for the second hole trap in S3 versus filling pulse width.....	90
Figure 3-13: Temperature point of DLTS spectra peaks versus filling pulse width..	91
Figure 3-14: The IV-T characterization for S3.....	93
Figure 3-15: Distinguishing the dark current components by dark current modeling a) at the operation temperature of 300K. b) at the operation temperature of 200K [32]......	96
Figure 3-16: Variation of the G-R lifetime with respect to the temperature [32].....	97

CHAPTER 1

INTRODUCTION

Infrared detectors, which convert infrared radiation into electrical output, form one of the most important group of sensors in civil and defense system applications. In the civilian area, these sensors play a major role in applications such as medical thermography, fire detection, remote sensing etc. Infrared detector technology is an active research area that progresses every day. Accordingly, characterization of detectors plays a crucial role in order to optimize the detection and imaging performance. There are various performance factors for photodetectors such as the responsivity, noise, detectivity and noise equivalent power (NEP). Defects and traps in detector semiconductor layers strongly affect the dark current and characteristics of these detectors. Therefore, the identification of the traps in detector structures is critical for achieving desirable device characteristics. Deep Level Transient Spectroscopy (DLTS) is one of the powerful techniques yielding the density, energy level and the capture cross section of the traps in materials. This method is based on transient capacitance measurements on rectifying contacts (p-n or Schottky junctions). The method is described in detail in Chapter 2.

Photodetectors operating in the short wavelength infrared (SWIR) band offer many applications and a big market growing very rapidly. Some of these applications are process control, remote sensing, food sorting and hyperspectral imaging. Reducing the dark current and increasing the performance of these detectors is one of the current hot topics in the infrared detector research area. The objective of this thesis is to identify and characterize the electrically active traps in the InGaAs SWIR photodetectors grown on InP substrates with molecular beam epitaxy (MBE). The

main motivation of the study is gathering useful data that can be utilized in studies towards dark current reduction in SWIR detectors. $\text{In}_x\text{Ga}_{1-x}\text{As}$ with different In mole fractions in the absorber layer are investigated in this work for this purpose.

1.1 Basis of Infrared Detection

Sir William Herschel empirically detected invisible radiation right after the red end of the magnetic spectrum for the first time in 1800. Figure 1-1 presents infrared region, which is the invisible radiation field right after visible light range and before radio waves.

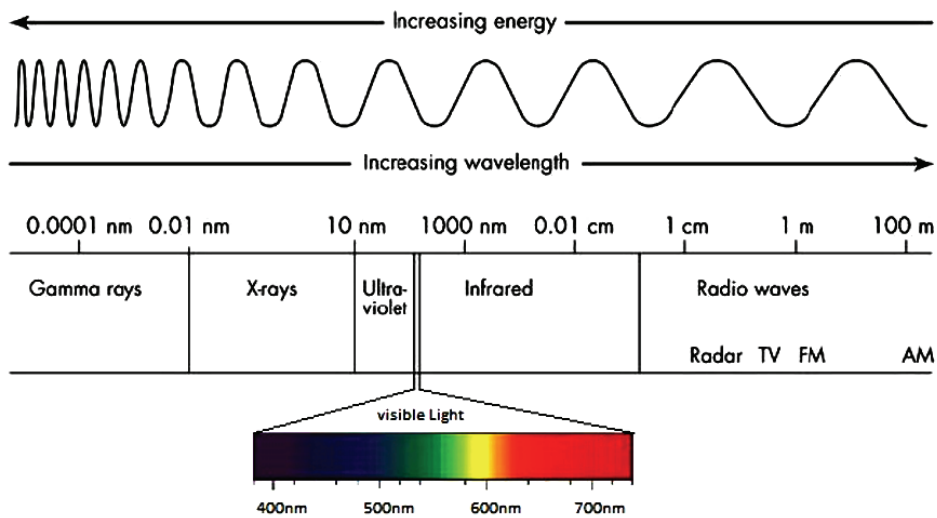


Figure 1-1: Electromagnetic spectrum [1].

Infrared radiation can be divided into six divisions with respect to wavelength range as;

- Near infrared (NIR), $0.7\text{-}1 \mu\text{m}$
- Short wavelength infrared (SWIR), $1\text{-}3 \mu\text{m}$
- Medium wavelength infrared (MWIR), $3\text{-}6 \mu\text{m}$
- Long wavelength infrared (LWIR), $6\text{-}15 \mu\text{m}$
- Very long wavelength infrared (VLWIR), $15\text{-}30 \mu\text{m}$
- Far infrared (FIR), $30\text{-}1000 \mu\text{m}$

All objects emanate infrared radiation for temperatures higher than the absolute zero. Materials interact with radiation in three different forms [2];

- 1) reflection (ρ)
- 2) absorption (α)
- 3) transmission (T)

Blackbodies absorb all radiation without either reflection or transmission. Some pioneer work was done on energy transport with respect to the wavelength emitted from blackbodies at different temperatures in the late 19th century. *Kirchhoff's law* forms the relation between the radiant emissivity of the object and its absorption [3]. Reflection, absorption and transmission are the results of interaction between the object and the incident radiation. The relation among those is known as *Kirchhoff's law* and is written as follows,

$$\rho + \alpha + T = 1 \quad (1-1)$$

where,

$$\rho(\text{reflectance}) = \frac{\text{reflected energy}}{\text{incident energy}} \quad (1-2)$$

$$\alpha(\text{absorbance}) = \frac{\text{absorbed energy}}{\text{incident energy}} \quad (1-3)$$

$$T(\text{transmittance}) = \frac{\text{transmitted energy}}{\text{incident energy}} \quad (1-4)$$

Emissivity for blackbodies is equal to 1 while it is independent of wavelength. Depending on its temperature, a blackbody emits the maximum radiation at a certain wavelength. Emissivity of gray-body (object) is the ratio of the radiation power

emitted from a matter's unit area (Exitance (M)) to the radiation power emitted from unit area of the blackbody at the same temperature.

The amount of the radiation and the wavelength of peak emission radiated by a blackbody are the functions of its temperature. Planck's Law in equation 1-5 represents the relation between the spectral exitance and the temperature of a blackbody[3];

$$M_{p(\lambda,T)} = \frac{2\pi hc^2}{\lambda^5} \frac{1}{\left(e^{\frac{hc}{\lambda kT}} - 1\right)} \quad (1-5)$$

where, $M_{p(\lambda,T)}$ (photons/cm²-sec-μm) is spectral exitance, h is Planck's constant, c is light's speed, T is the temperature in Kelvin and k is Boltzmann's constant. Figure 1-2 shows the relation between exitance and wavelength for blackbodies at various temperatures.

Several concepts can be deduced from Plank's law. The most important of them is the Wien's displacement law. The peak emission wavelength (λ_{peak}) for a certain blackbody temperature T can be obtained using Wien's displacement law.

Wien's displacement law is expressed by Equation 1-6.

$$\lambda_{peak} = \frac{2898\mu m \cdot K}{T} \quad (1-6)$$

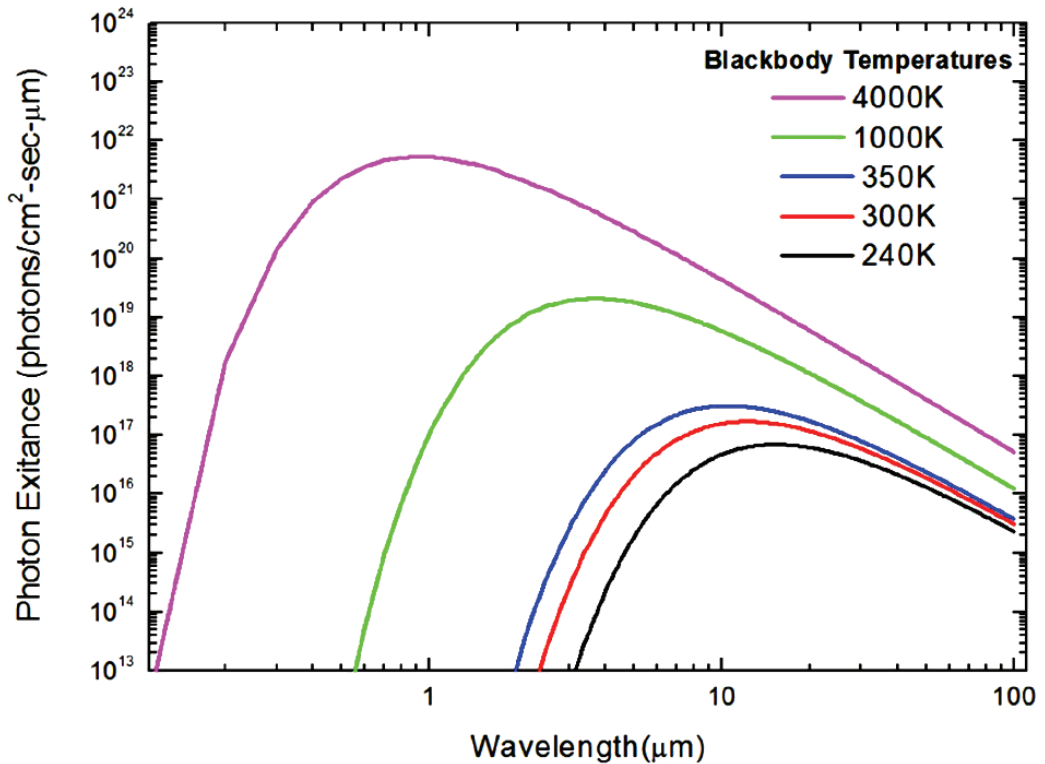


Figure 1-2: Photon spectral exitance vs. wavelength curves of blackbodies at various temperatures [3].

Air is the known propagation medium for blackbody radiation. Atmospheric transmission can be affected by many parameters such as climate conditions, humidity and air composition. Transmitted radiation through atmospheric contents can be defined based on scattering and absorption. Figure 1.3 shows transmission versus wavelength plot in horizontal path at sea level. IR transmission varies for each IR range due to the existence of gas molecules at the atmosphere. The application environment determines the IR band used for thermal imaging.

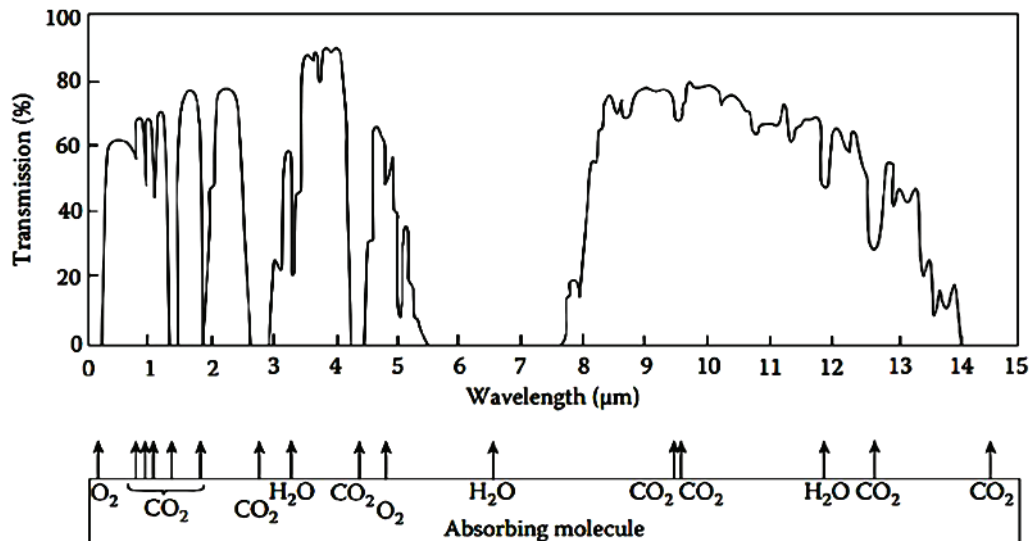


Figure 1-3: Atmospheric transmission at sea level along a horizontal path of 2 km [4].

1.2 Infrared Photon Detectors

Progress in IR detector technology is connected mainly to semiconductor IR detectors, which are included in the class of photon detectors. In this class of detectors, the radiation is absorbed within the material by interaction with electrons. The observed electrical output signal results from the changed electronic energy distribution. They exhibit both perfect signal-to-noise ratio performance and a very fast response. However, to achieve this, the photon detectors require cryogenic cooling. Cooling requirements are the main obstacle to the more widespread use of IR systems based on semiconductor photodetectors making them relatively bulky, heavy and expensive. Photon detectors are divided into various types based on nature of interplay. The main types are:

- a) Intrinsic detectors,
- b) Extrinsic detectors,
- c) Photo emissive (metal silicide Schottky barriers) detectors,
- d) Quantum well and superlattice detectors.

Table 1-1 lists the advantages and disadvantages of IR detectors based on various technologies.

Table 1-1: Comparison of IR detector technologies [5].

Technology	Advantages	Disadvantages
Thermal	Light, rugged, reliable, and low cost for operating at room temperature	Lower detectivity Slow response (in the order of ms)
Photon Intrinsic		
IV-VI	Available low-band gap materials Well studied	Poor mechanical properties Large permittivity
II-VI	Easy band-gap tailoring Well-developed theory and experiment. Multi-color detectors	High cost in growth and processing
III-V	Good material and dopants properties Advanced technology Possible monolithic integration	There does not exist many different materials especially for thermal imaging
Extrinsic	Very long wavelength operation Relatively simple technology	Extremely low temperature operation
Free carriers	Low-cost, high yields Large and close packed 2D arrays	Low quantum efficiency Low temperature operation
Quantum well and Superlattice Structures		
Type I	Matured material growth Good uniformity over large area Multicolor detectors	Low quantum efficiency
Type II	Theoretical expectations estimating better performance when compared with conventional photovoltaic detectors	Complicated design and growth Sensitive to the interfaces Passivation and reproducibility problems

1.2.1 Extrinsic Detectors

In extrinsic PDs, a large bandgap semiconductor is doped to create impurity levels in the semiconductor's bandgap. Photons excite the carriers from impurity level, which is tuned to be close to the conduction band. The excited carriers contribute to the photocurrent through the device. The cut-off wavelength of the detector is determined by the energy difference between the impurity level and bottom of the conduction band. Si:In, Si:Ga, Ge:Cu and Ge:Hg are some of the extrinsic detector materials [6].

1.2.2 Intrinsic Detectors

Intrinsic PDs absorb the radiation whose energy is equal to or greater than the bandgap of its active material. In order to have high absorption efficiency, absorber material should have a direct bandgap. For materials with indirect bandgap, electrons should absorb phonon besides the photon to jump into the conduction band state. Intrinsic detectors can be constructed in two ways: photoconductive and photovoltaic detectors [7].

Photoconductive (PC) detectors are based on the generation of free carriers due to the radiation absorption. Absorbed radiation creates electron hole pairs. Excited electrons transfer from valence band to the conduction band. The increase in free electrons of conduction band result in higher conductivity, which leads to a change in electrical current. Changes in current value and conductivity can be obtained by an external electrical circuit and applying an external bias. Figure 1-4 illustrates a photoconductor and its read-out circuitry.

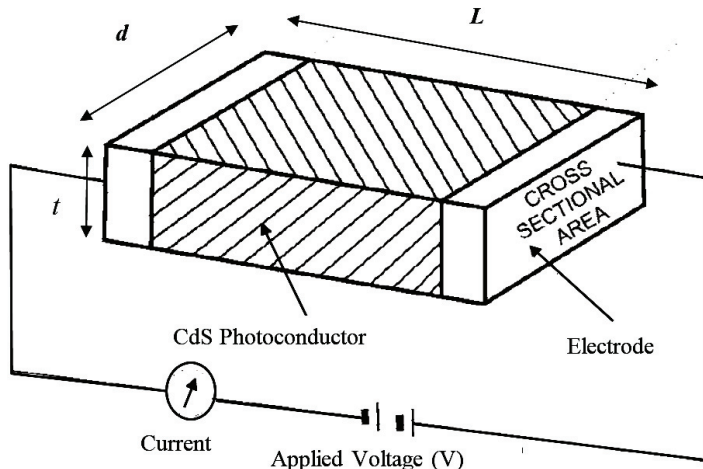


Figure 1-4: CdS photoconductive detector cell schematic, diagram and operation circuit [8].

Photovoltaic (PV) detectors are also based on carrier generation under illumination; but an external bias is not necessary to collect the free carriers. PN junctions are mainly used for PV detectors. By absorbing radiation, free carriers are created in n- and p-type material. Generated carriers sweep to the other side due to the built-in potential in the depletion region, where p- and n-type materials are connected to each other. Figure 1-5 (a) shows a PV cell structure and its operation schematic. Figure 1-5 (b) illustrates the I-V curve of the PV cell under the presence and absence of the illumination.

When photovoltaic diode is not under illumination the only current existing in the junction is the leakage current (dark current). After illumination, photocurrent owing to radiation absorption will be added to the leakage current.

The dark current mechanisms can be listed as;

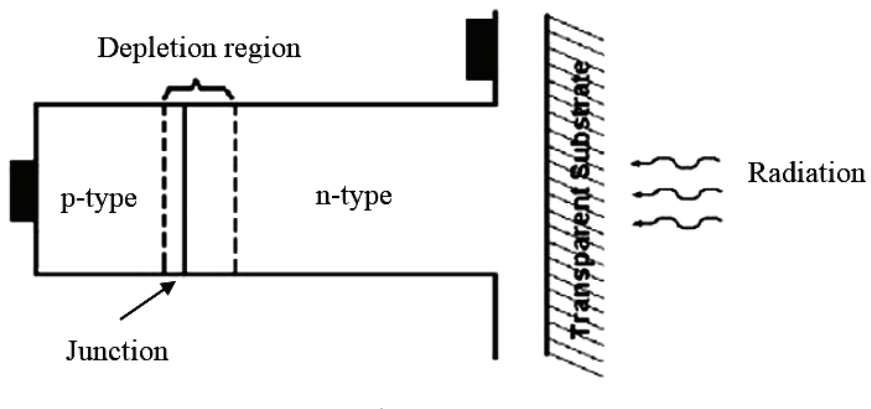
- G-R current (due to generation-recombination process in depletion region)
- Surface Leakage
- Tunneling

- Ohmic Leakage
- Diffusion current

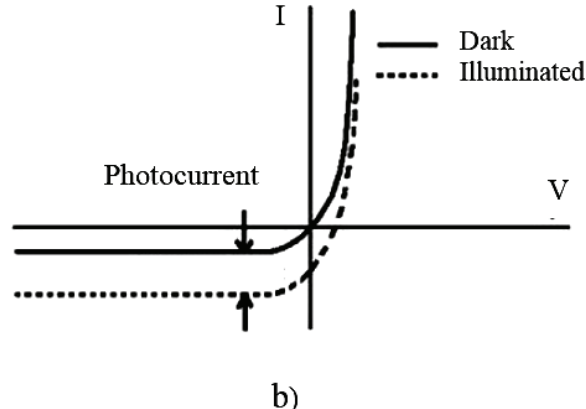
The photocurrent generated in photovoltaic diode can be expressed as;

$$I_p = qA g_{opt} (L_p + L_n + W) \quad (1-7)$$

where g_{opt} is carrier generation rate, A is area of photodiode, L_p and L_n are diffusion length of holes and electrons in n and p sides of photodiode.



a)



b)

Figure 1-5: Photovoltaic p-n diode (a) Structure and operation schematic and (b) I-V curve [9].

1.2.3 Quantum Well and Superlattice Structures

Superlattice detectors were first introduced by Leo Esaki [10]. Superlattice detectors are made of different semiconductors with different bandgaps. They have periodic structures in the order of angstroms. Superlattice detectors can be divided into two groups, namely type I and type-II, based on positioning of valence band and conduction band of different type of semiconductors.

Type-I superlattices are known as Quantum Well Infrared Photodetectors (QWIPs). Structure of QWIPs is based on a small bandgap material placed between large bandgap materials. Figure 1-6 illustrates construction of quantum wells due to barrier formation by employing large bandgap semiconductors. After illumination, photon excitation occurs in the quantum well. The excited electrons contribute in the current flow.

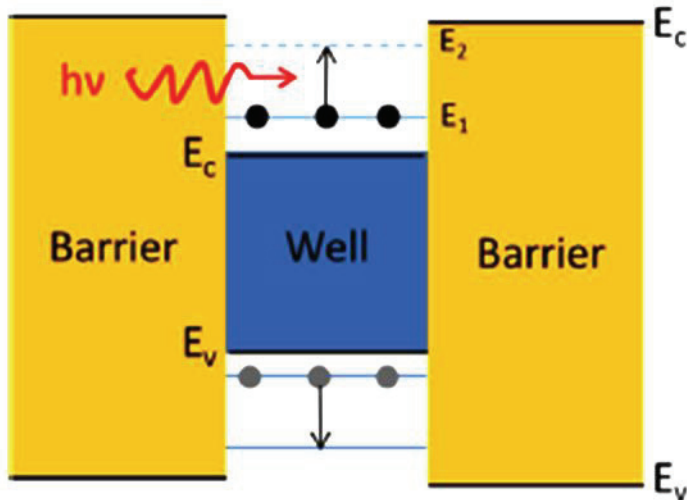


Figure 1-6: Energy band diagram of a QWIP structure and intersubband transition of electrons in the well [11].

Type-II superlattices are based on the formation of a virtual bandgap by employing two different type of semiconductors with different energy band levels. InAs and InGaSb are two favorite alloys for type-II superlattice fabrication. As shown in

Figure 1-7, artificial hole and electron bands are generated due to the difference between energy levels of InAs conduction band and InGaSb valence band.

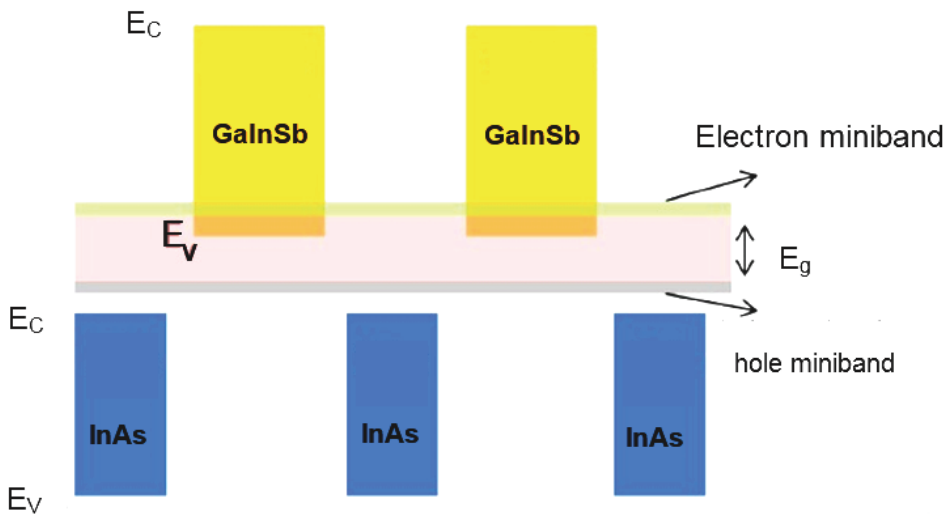


Figure 1-7: Type-II superlattice infrared photodetector band structure and the formation of artificial bandgap [11].

1.3 Short Wavelength Infrared (SWIR) photodetectors

Infrared radiation in the wavelength range of $0.9 - 2.5 \mu\text{m}$ is known as short wavelength infrared radiation. The detectors acting in this range of wavelength is known as SWIR photodetectors. SWIR detector technology is one of the active research areas due to its wide application in different fields. They have industrial applications such as telecommunication, spectroscopy, space science, process control, night vision and defense [11].

While, SWIR imaging is similar to visible imaging, it provides some advantages. Scattering by atmosphere is lower for SWIR radiation with respect to the visible light because of the longer wavelength. In addition, these PDs are suitable for inconvenient weather conditions. They can operate in hazy or foggy weather. Determining the moisture and humidity uniformity or liquid level over opaque materials are possible by using SWIR detectors due to absorption of SWIR by moist.

Ability to detect reflected radiation, fierce through paintings, higher sensitivity are some of the notable properties. Figure 1-8 provides some examples for the above-mentioned advantages of SWIR photodetectors [12,13,14].

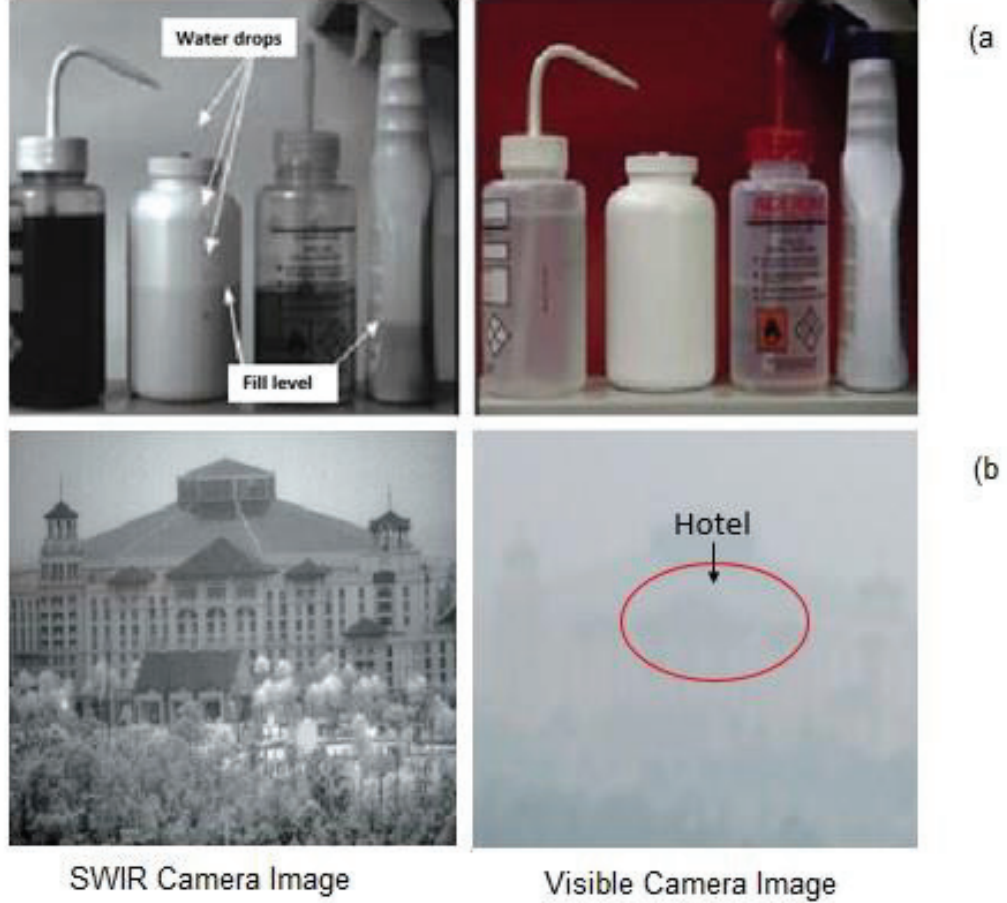


Figure 1-8: comparison of SWIR and Visible imaging. (a) The SWIR image (left) shows ability of SWIR technology to detect the liquid levels in plastic bottles, which are opaque to the eye. The right image shows the visible image of the bottles. (b) The left image belongs to a hotel through a distance of 2.5 km in a foggy weather, taken by commercial visible camera; the right image belongs to the same place and condition, taken with a SWIR 640x512 pixel camera [13-14].

Conventional SWIR FPAs consist of p-n junction photodiodes. These photodiodes can be either homojunctions or heterojunctions. In the homojunction structure, the same semiconducting material with different dopants is used in the p- and n-sides of

the diode. The heterojunction structure means that materials used for n and p sides are different semiconductors. SWIR FPAs can be fabricated in the form of p-i-n diodes in addition to p-n diodes. In this type of structure, an intrinsic or low-level doped semiconductor is placed between n⁺ and p⁺ sides of the junction. This layer is known as absorber or active layer where free carriers are generated via absorbing the photon energy. The low response time and the higher quantum efficiency are the advantages of the p-i-n diodes compared to p-n diodes. Figure 1-9 shows the structure and energy band diagram of PDs under reverse bias.

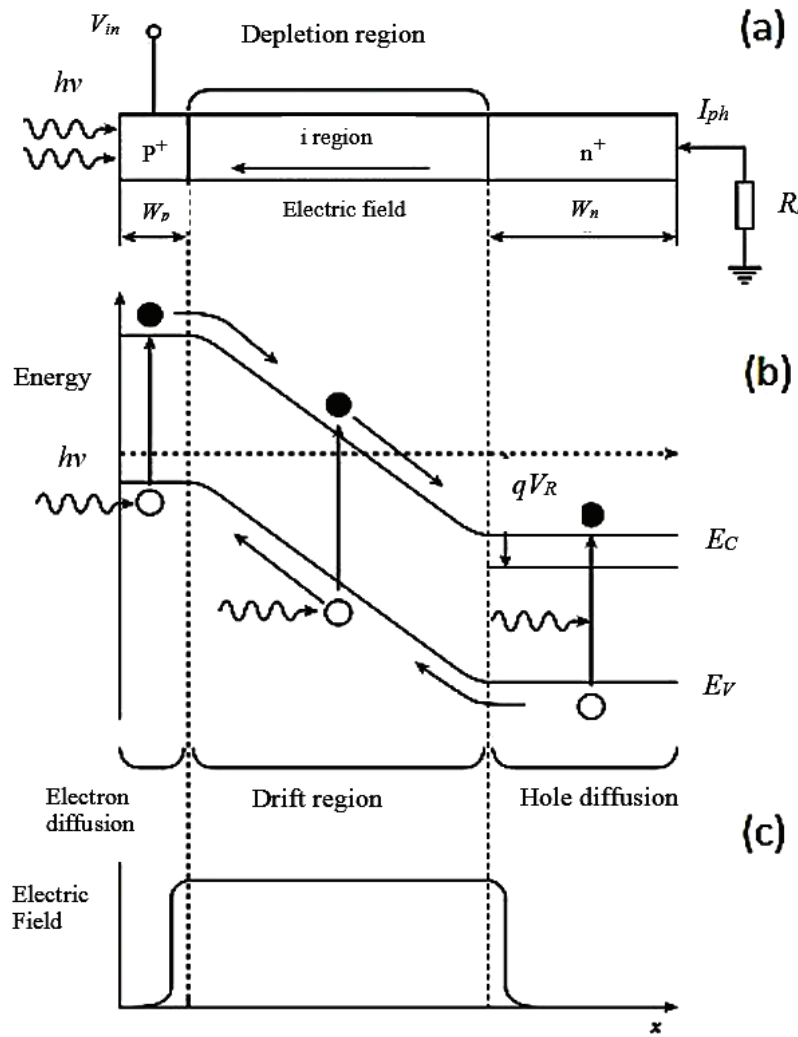


Figure 1-9: (a) The p-i-n diode diagram (b) energy band diagram under applied reverse bias (c) the profile of created electric field in p-i-n photodiode [15].

1.3.1 Germanium and Silicon SWIR PDs

Ge/Si, $\text{Si}_{1-x}\text{Ge}_x/\text{Si}$, HgCdTe/CdZnTe and $\text{In}_x\text{Ga}_{1-x}\text{As}/\text{InP}$ are the most favorite materials for SWIR photodiode fabrication. Lattice mismatch between Ge and Si is the main problem for Ge/Si structure that decreases the photodiode performance. Insecure GeO_2 is the other problem that affects properties associated with passivation [15]. On the other hand, $\text{Si}_{1-x}\text{Ge}_x$ is an alloy which can be grown on Si substrate. The required bandgap for a definite cut-off wavelength can be obtained by changing the mole fraction of Ge [15]. The relations among the mole fraction, bandgap and cut-off wavelength are shown in Figure 1-10. It is possible to grow the alloy with required thickness by employing epitaxy methods.

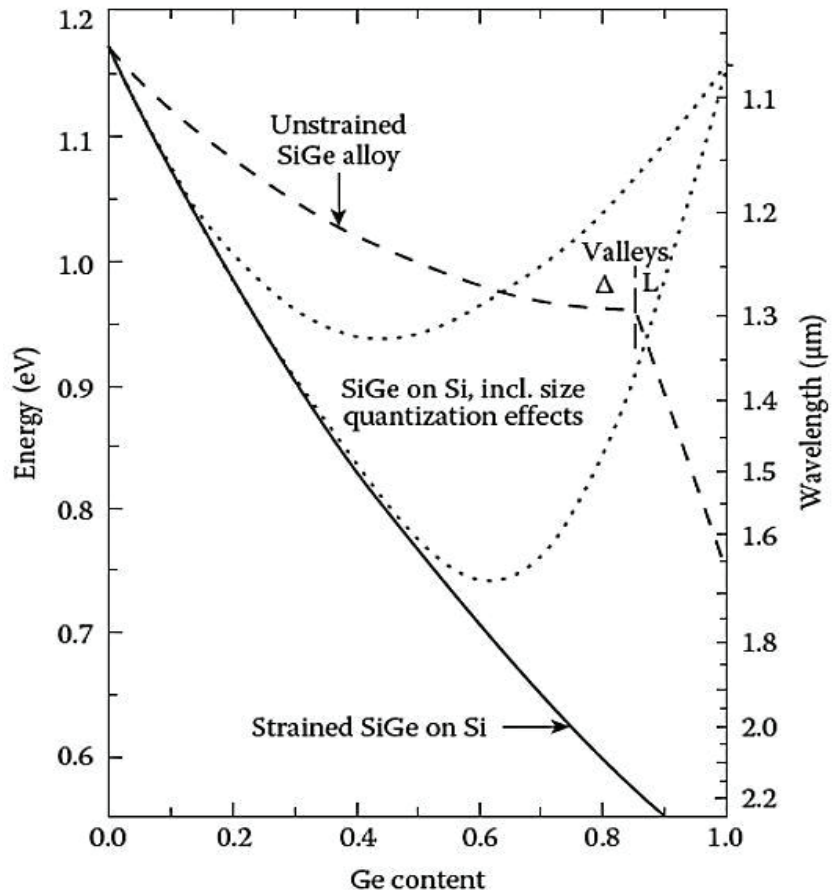


Figure 1-10: The relation between bandgap and cut-off wavelength of $\text{Si}_{1-x}\text{Ge}_x$ and Ge mole fraction [16].

1.3.2 Mercury Cadmium Telluride SWIR PDs

Mercury Cadmium Telluride ($\text{Hg}_{1-x}\text{Cd}_x\text{Te}$, aka MCT) was first introduced by Lawson et al [17]. It can be used for various photodetectors operating in different wavelength ranges. It is possible to get the required bandgap by changing the mole fraction of CdTe. The relation between CdTe mole fraction and the bandgap of the alloy is illustrated in Figure 1-11. The advantage of this compound is that, it can operate in almost whole IR band.

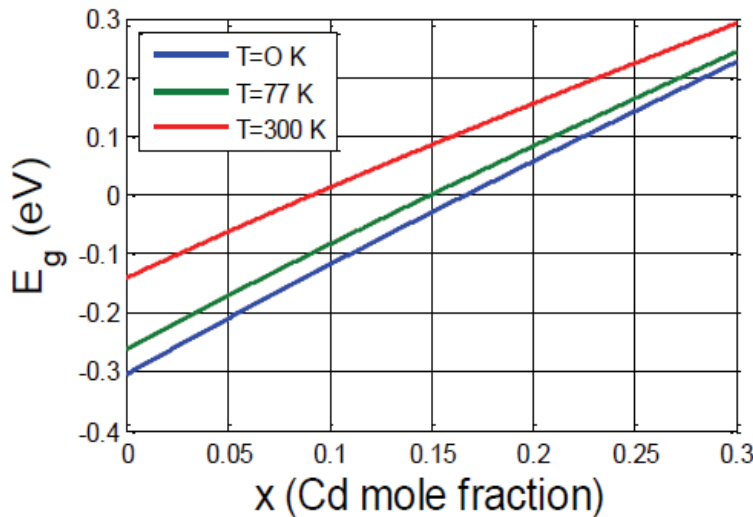


Figure 1-11: MCT bandgap value for different mole fractions of CdTe [18].

$\text{Hg}_{1-x}\text{Cd}_x\text{Te}$ alloy is a direct bandgap semiconductor. It can be epitaxially grown on CdZnTe. It is possible to provide relatively high quantum efficiency (~90%) by employing this material. CdZnTe is an excellent substrate for MCT, however it is costly and limited for sizes more than $8\times 8 \text{ cm}^2$. In order to overcome these limitations, other materials such as GaAs and Si are suggested which can be used as the substrate for MCT FPAs where, lattice mismatch for HgCdTe/Si and HgCdTe/GaAs are 19% and 14.3%. High lattice mismatch results in deficient structures, decreasing the performance of photodetectors considerably [19,20].

1.3.3 Indium Gallium Arsenide SWIR PDs

$\text{In}_x\text{Ga}_{1-x}\text{As}$ is one of the favorite semiconductor compounds for infrared detector technologies due to its optical and electrical properties. It is an III-V compound semiconductor consisting of InAs and GaAs alloys. The lattice constant of the compound varies between 6.058 \AA (for $x=0$ resulting GaAs) and 5.653 \AA (for $x=1$ resulting InAs). InP is the suitable substrate for the epitaxial growth of $\text{In}_x\text{Ga}_{1-x}\text{As}$ which is lattice matched at the In mole fraction of 0.53. Detectors epilayers can be produced by employing most of the epitaxial growth techniques such as Metal-Organic Chemical Vapor Deposition (MOCVD), Atomic Layer Epitaxy (ALE), Molecular Beam Epitaxy (MBE), Liquid Phase Epitaxy (LPE), and Hydride-Transport Vapor Phase Epitaxy (VPE). Lattice constant dependence on mole fraction is illustrated in Figure 1-12. The relation between lattice constant and cut-off wavelength is shown in Figure 1-13.

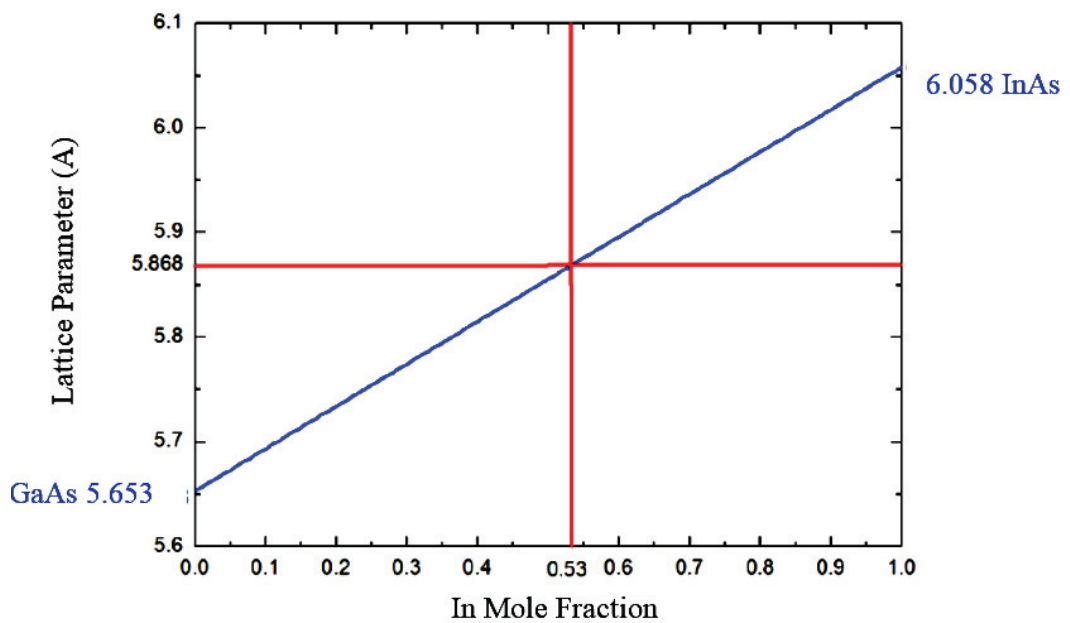


Figure 1-12: Lattice constant dependence on In mole fraction in $\text{In}_x\text{Ga}_{1-x}\text{As}$ [11].

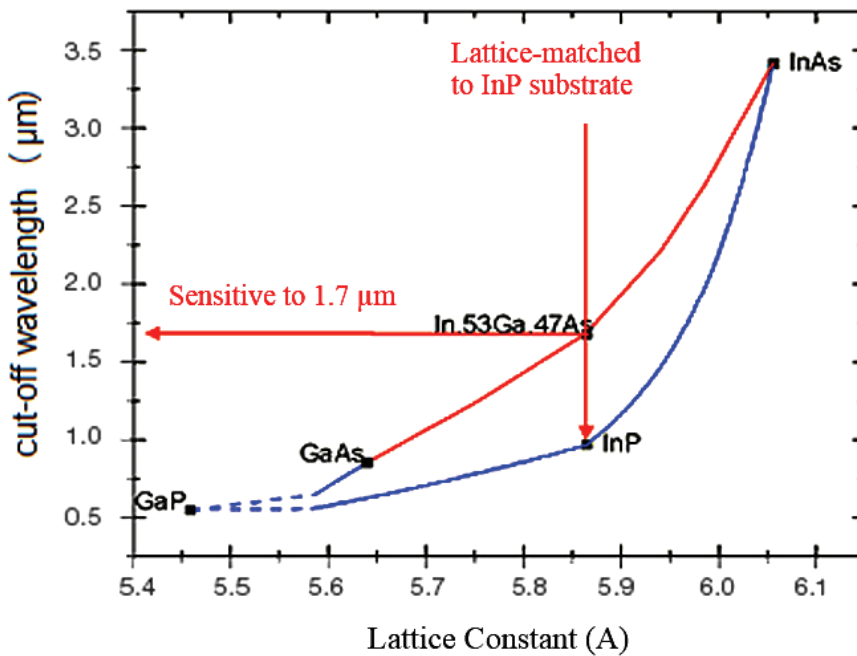


Figure 1-13: Cut-off wavelength value for different lattice constant values [21].

The energy bandgap of the alloy varies from 0.354 eV for $x=1$ (InAs) to 1.424 eV for $x=0$ (GaAs) at room temperature. Bandgap energy for specific temperature T and In mole fraction (x) can be calculated by equation 1-8. Figure 1-14 shows the bandgap energy and cut-off wavelength dependence on In mole fraction x .

$$E_{g(x,T)} = 0.42 + 0.625x - \left(\frac{5.8}{T+300} - \frac{4.19}{T+27} \right) 10^{-4} T^2 x \quad (1-8)$$

$$- \frac{4.19 \times 10^{-4}}{T+271} T^2 + 0.475x^2$$

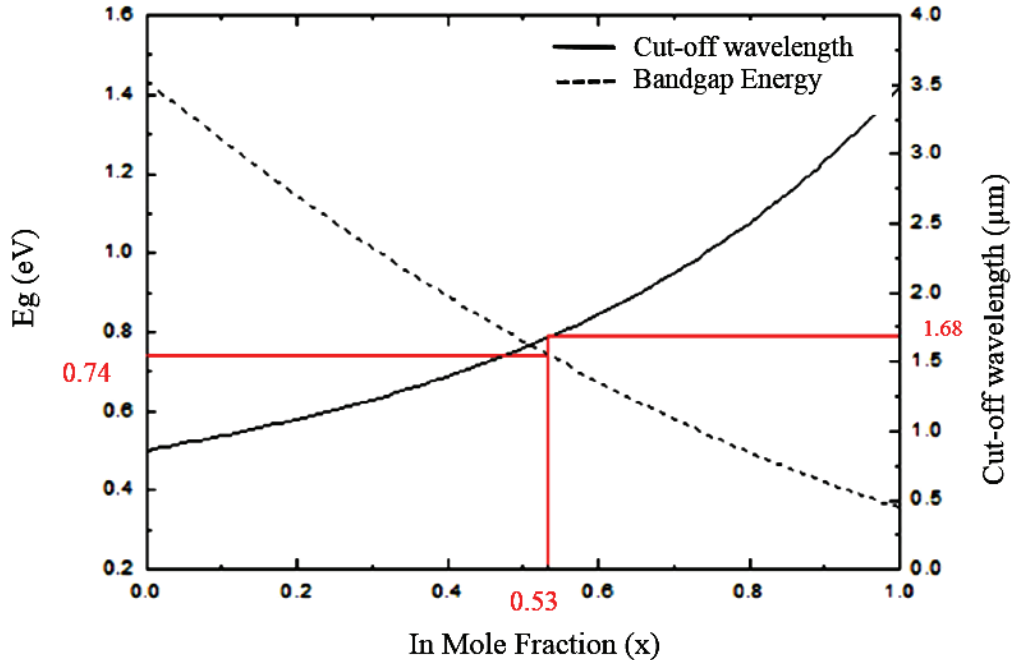


Figure 1-14: Bandgap energy and cut-off wavelength dependence of $\text{In}_x\text{Ga}_{1-x}\text{As}$ on In mole fraction [11].

Perfect lattice match between $\text{In}_{0.53}\text{Ga}_{0.47}\text{As}$ and InP, in addition to its perfect optical and electrical properties make it one of the favorite semiconductor compounds. $\text{In}_{0.53}\text{Ga}_{0.47}\text{As}$ has a considerably large absorption coefficient, high electron mobility and cut-off wavelength of 1.68 μm at room temperature [21].

The dark current of the $\text{In}_{0.53}\text{Ga}_{0.47}\text{As}/\text{InP}$ SWIR photodetectors is quite small at room temperature (in the order of nA/cm^2). Metallurgical properties of the absorber layer material can seriously affect the amount of the dark current. For instance, crystal defects existing in low quality material lead to Shockley-Read-Hall (SRH) mechanism increasing the dark current [23]. $\text{In}_{0.53}\text{Ga}_{0.47}\text{As}$ SWIR PDs can be fabricated based on both p-i-n and avalanche photodiode structures. The possibility of extension of the cut-off wavelength up to 2.7 μm by increasing mole fraction to $x=0.82$ is the other feature of $\text{In}_{0.53}\text{Ga}_{0.47}\text{As}$ SWIR PDs [24].

The spectral responsivity of $\text{In}_{0.53}\text{Ga}_{0.47}\text{As}$ SWIR photodiode is compared to the irradiance of night sky in Figure 1-15. The cut-off wavelength of the photodiode is

very close to the peak emission wavelength of nightglow. As a result, this photodiode is suitable for night vision applications.

Cut-on wavelength of the photodetector is defined by the InP substrate with bandgap energy of 1.34 eV. The InP substrate absorbs wavelengths below 0.9 μm . It is possible to broaden the responsivity and shift it to lower wavelengths by reducing or eliminating the substrate. Figure 1-16 shows the difference between responsivity of $\text{In}_{0.53}\text{Ga}_{0.47}\text{As}$ photodiode before and after substrate removal.

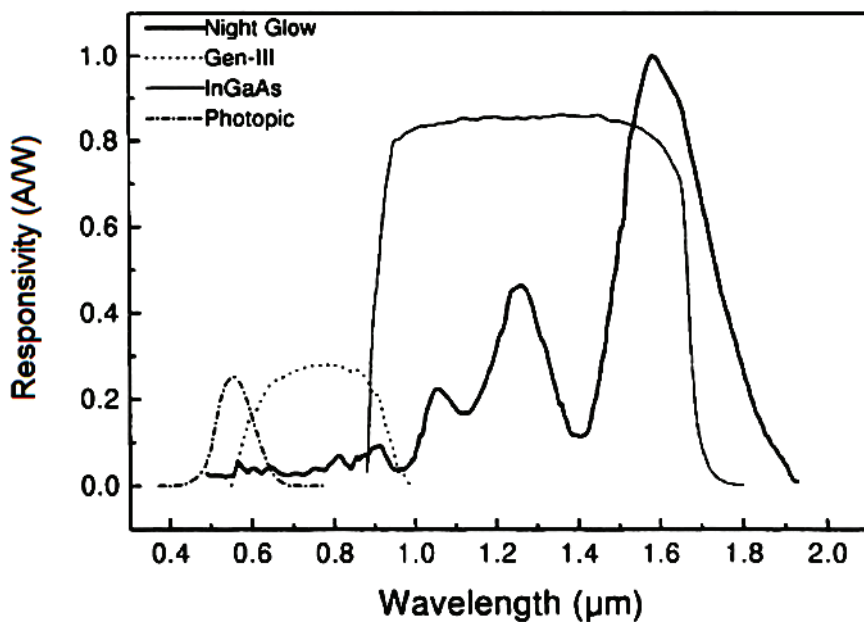


Figure 1-15: Contrasting the responsivity of $\text{In}_{0.53}\text{Ga}_{0.47}\text{As}$ and irradiant of night sky [25].

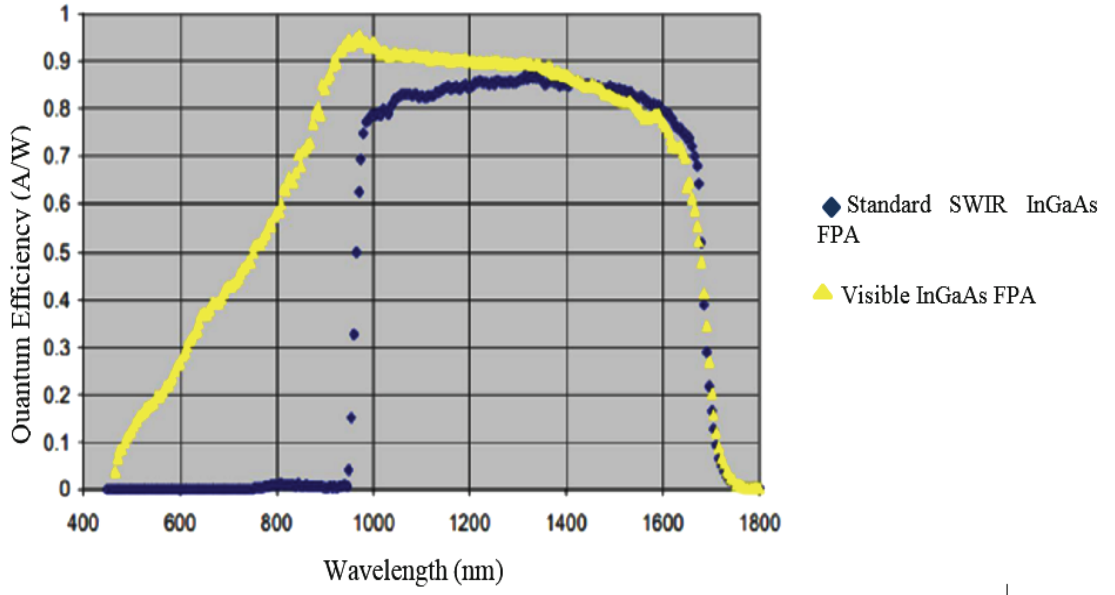


Figure 1-16: Comparison between responsivity spectra of $\text{In}_{0.53}\text{Ga}_{0.47}\text{As}$ photodetector before (blue plot) and after (yellow plot) elimination of the InP substrate [26].

1.3.4 Extended Wavelength InGaAs SWIR Photodetectors

For mole fraction of $x=0.83$, the cut-off wavelength of $\text{In}_x\text{Ga}_{1-x}\text{As}$ absorber layer extends up to $2.7\mu\text{m}$. In that case, the lattice mismatch between $\text{In}_{0.83}\text{Ga}_{0.17}\text{As}$ and InP substrate reaches 2% that leads to some changes in the photodiode properties. Dark current of these photodiodes at the room temperature is much larger being in the orders of mA/cm^2 . High quality material with less crystal defects can strongly decrease the amount of the bulk dark current. Presence of the impurities increases the dark current value by introducing generation-recombination centers and increasing the amount of the G-R component. The unavoidable dislocation defects due to the large lattice mismatch raise the dark current as well. While, large dark current is one of the major challenges of this kind of detectors, their performance is comparable with the lattice-matched SWIR detectors if they are sufficiently cooled [27].

1.4 InGaAs SWIR Photodetector Structure

InGaAs SWIR PDs can be fabricated based on planar and mesa structures. All the samples used in this work were fabricated in the mesa structure. The thickness of each epilayer is controlled during the growth process. After growth of all layers, pixels are defined by wet or dry etching process which is known as mesa etching. Because of this step, dangling bonds are created on the pixel walls leading to the creation of surface leakage. Passivating the bonds by employing dielectric materials is the solution for this problem.

In order to have larger quantum efficiency and smaller response time, InGaAs SWIR PDs can be fabricated as p-i-n photodiodes. P-i-n structure can be obtained by embedding the InGaAs absorption layer between p-type and n-type layers with larger bandgaps. The structure of a p-i-n InGaAs photodiode is illustrated Figure 1-17. “Be” doped InP and “Si” doped InP can be used as the p⁺ and n⁺ large bandgap materials. By removing the InP substrate, responsivity spectrum can be broaden to the visible light wavelength range. An etch stop layer of In_{0.53}Ga_{0.47}As is used between the substrate and n⁺-InP in order to control the etching. This layer makes substrate removal process easier. A cap layer of In_{0.53}Ga_{0.47}As is used on top of the structure which facilitates construction of low resistance ohmic contacts. Figure 1-18 shows the absorption of an In_{0.53}Ga_{0.47}As layer at different thicknesses at the wavelength of 1.55μm. Absorption is around 90% for thicknesses in the range of 3-4 μm.

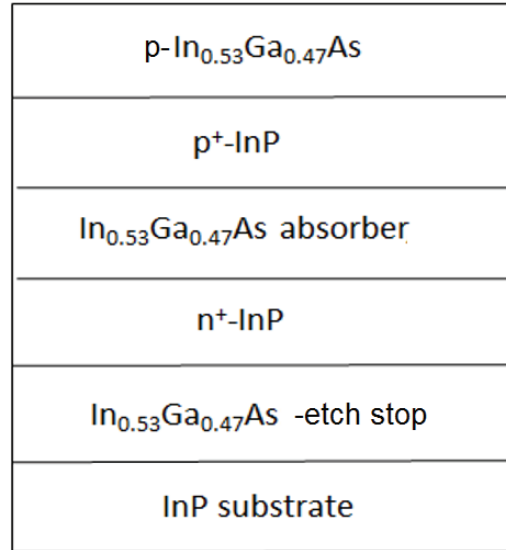


Figure 1-17: Epilayer structure of an $\text{In}_{0.53}\text{Ga}_{0.47}\text{As}$ photodetector.

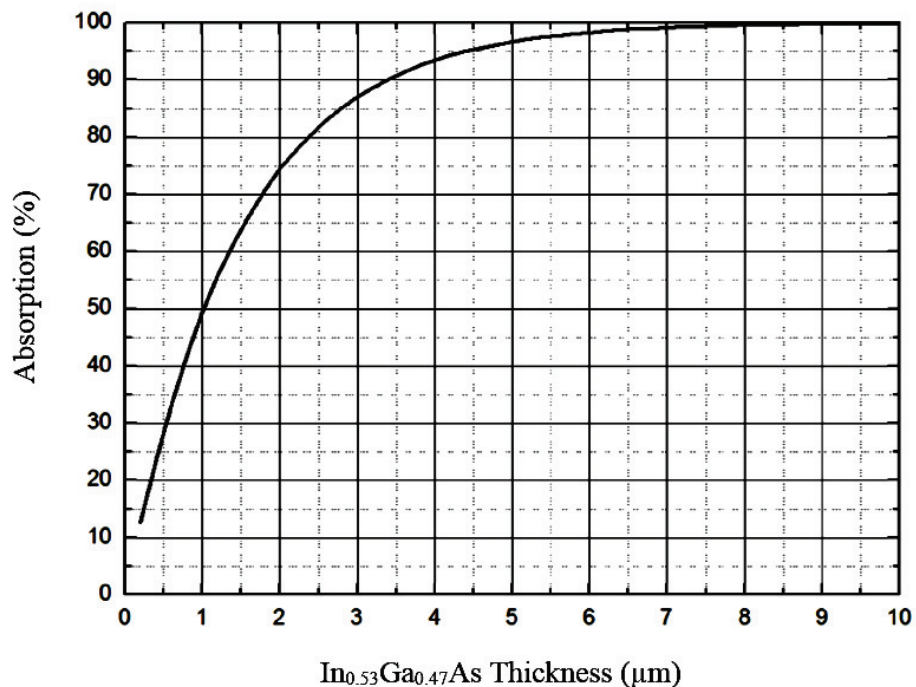


Figure 1-18: Absorption (at $1.55 \mu\text{m}$) by $\text{In}_{0.53}\text{Ga}_{0.47}\text{As}$ at different thicknesses [11].

Extended wavelength $\text{In}_x\text{Ga}_{1-x}\text{As}$ photodetectors with different epilayer structures have been investigated by various research groups. Martinelli *et al.* [28] studied a structure which consists of graded $\text{In}_x\text{Ga}_{1-x}\text{As}$ layer as the buffer layer. The absorber layer is n-type $\text{In}_{0.82}\text{Ga}_{0.18}\text{As}$ with a cut-off wavelength of $2.6 \mu\text{m}$. Later, Olsen *et al.* [29] have employed a step graded $\text{InAs}_y\text{P}_{1-y}$ as a buffer layer which decreased the dark current. Some investigations have been done to improve the performance of the linear graded $\text{InAs}_y\text{P}_{1-y}$ buffer layer by Hondt *et al.* [30]. Zhao-Bing *et al.* [31] utilized linearly graded $n^+ \text{-In}_x\text{Al}_{1-x}\text{As}$ with $x:0.52 \rightarrow 0.85$ as the buffer layer. A large format (640×512) $\text{In}_{0.83}\text{Ga}_{0.17}\text{As}$ FPA with linearly graded $\text{In}_x\text{Al}_{1-x}\text{As}$ buffer was fabricated and characterized by the research group at the Quantum Devices and Nanophotonics Research Laboratory of the Electrical and Electronics Engineering Department of the Middle East Technical University [32]. The research group has identified the performance limiting mechanisms through detailed electrical and optical characterization of the FPA pixels. The detectors displayed desirable characteristics at both pixel and FPA levels.

1.5 Deep Level Transient Spectroscopy (DLTS)

Presence of the defects in the semiconductors is an unavoidable issue. They can considerably affect the electrical properties of the material. Defects can be related to the external impurity atoms or crystal properties. They can be divided into two main groups as shallow level and deep level defects.

In order to control the electrical properties such as the conductivity and the lifetime, dopant atoms are intentionally added to the semiconductor materials. They can be classified as shallow level defects. They create an extra energy level in the bandgap close to the valence band or the conduction band. Shallow level characteristics can be obtained by employing the electrical and optical measurements. The properties such as the density of traps can be determined electrically, while features such as energy level of traps can be measured optically.

The contribution of the unwanted dopants into the semiconductor alloys during the fabrication and growth process is inevitable. These external dopants, such as Oxygen

in Si, and the crystalline defects (such as vacancies and dislocations) are classified as deep level defects. They introduce deep energy levels that controls the generation-recombination rate and the lifetime of the free carriers. The optimization of the semiconductor devices requires the characterization of these defects [33].

Deep Level Transient Spectroscopy method is firstly introduced by Lang at 1974 [34]. This method is based on the high-frequency capacitance transient thermal scanning. DLTS is used for investigating the existing traps in semiconductors. The capacitance measurements in this technique result in the positive and negative peaks on a flat baseline as a function of temperature. Traps in semiconductors and their properties can be identified by studying these peaks. The sign of the peaks determines the type of the traps in the form of majority or minority traps. The trap concentration is proportional to the peak amplitude. The temperature point correlated to the peaks depends on the thermal emission properties of the traps. In addition, the characteristics such as the activation energy, concentration profile, and electron or hole-capture cross sections for each trap can be obtained according to the measurement results. The DLTS method is comparable with the other capacitance measurement techniques such as thermally stimulated capacitance (TSCAP), edge region TSCAP, admittance spectroscopy, and photocapacitance. Lang [35] recalls DLTS in a paper and discusses about the method more elaborately and comprehensively. DLTS method and its principles are discussed in Chapter 2.

For the last three decades, many modifications have been applied to DLTS method and different methods such as Double-Correlation DLTS (DDLTS), Constant Capacitance DLTS (CC-DLTS), Constant Voltage DLTS (CV-DLTS), Optical DLTS (ODLTS) and Reverse Pulse DLTS (RDLTS) were introduced [36].

1.6 Outline of the Thesis

The characterization of the traps existing in the semiconductors has a crucial role in the dark current and characterization of the photodetectors. In the present work, electrically active traps in three different $\text{In}_x\text{Ga}_{1-x}\text{As}$ SWIR photodiode samples were characterized and their relation with the detector dark current was investigated.

In Chapter 2, the DLTS method is discussed in detail. In chapter 3, the experimental work is presented and the results are discussed. Chapter 4 finalizes this thesis by summing up the accomplishments during this study and illustrating the future work related to this research work.

CHAPTER 2

DEEP LEVEL TRANSIENT SPECTROSCOPY TECHNIQUE

Identifying the properties of traps existing in the forbidden bandgap of semiconductor materials is important, since they affect the electrical properties strongly. For this purpose, a sensitive and fast method with reliable results is needed. This method should be able to distinguish the majority and minority traps and the method should provide information such as the concentration, capture cross section and activation energy of the traps. Deep Level Transient Spectroscopy (DLTS) is the most suitable method which includes all the above-mentioned features. Especially the spectroscopy features make it possible to precisely identify the traps existing in the sample under the measurement. Other methods such as thermally simulated current (TSC), thermally stimulated capacitance (TSCAP), edge region TSCAP, admittance spectroscopy, and photo capacitance were introduced previously, but they do not offer all of the DLTS measurement advantages.

DLTS method is based on the high-frequency capacitance transient measurement in the depletion layer of a p-n junction. The capacitance transient of the junction is a function of temperature and the thermal activity of traps. Accordingly, by thermal scanning the junction during the capacitance measurement, the spectra of the capacitance change of the junction versus temperature can be obtained. This spectrum defines the kind of the trap and its properties exclusively.

Since Lang introduced DLTS in the year 1974 [34], many different revisions of the method have been suggested. The derivation method of the spectra from the capacitance transient measurement results is the main difference between the suggested methods. The performance of the DLTS measurement set-up improved considerably by employing the microcomputers. The improvements include faster information processing, reduction in the number of thermal scanning and the high signal to noise ratio.

In this chapter, the DLTS measurement method and its systematic application is discussed in detail. Firstly, a short introduction to the different trap types and the generation-recombination processes are presented. Next, C-V measurement technique is described. The effects of the deep level traps on the capacitance and transient capacitance of the junction are reviewed. Finally, the principles of the DLTS method are explained.

2.1 Defects

The presence of the defects in different kinds of the materials and crystals is an undeniable fact. Defects can be divided into two main groups: a) Shallow-level impurity (due to the dopant atoms) and b) Deep-level impurity (related to the lattice defects and unwanted impurity atoms). During the last decades, there is a great focus on the fabrication of the high quality semiconductors. Many accurate technologies are developed for this purpose leading to a significant progress in electrical devices. The production of the high quality semiconductors became possible by accurate control over the doping density, the mole fraction and the purity of material with sensitive growth technologies. The mole fraction control is performed in order to obtain the proper material properties such as the optimum lattice constant and bandgap [33].

- a) ***Shallow Level Impurity:*** In order to get the n- or p-type materials, dopants are added to the semiconductors during the doping process. Ionization energy is the required energy for a free carrier to transfer from the shallow level to

the conduction or valence band. It can be determined by electrical and optical experimental methods.

- b) ***Deep-Level Impurity:*** Lattice defects and unwanted impurities create deep level traps in the bandgap. They are divided into two general subgroups as; a) point defects and b) dislocation defects. Point defects relate to the unwanted foreign atoms and the vacancies in the crystal structure. Dislocation defects relate to the lattice defects such as the stacking faults and edge dislocations. These defects introduce traps lying deep within the bandgap. While, the shallow levels generate free carriers, deep levels trap the electrons and the holes. Accordingly, they are known as the recombination centers that control the lifetime of the carriers. Deep level traps can be distinguished as the electron or hole traps by considering their interaction with the free carriers of the conduction and valence band. The traps that interact with the free electrons of the conduction band are known as the electron traps. Hole traps relate to the traps collaborating with the existing holes in the valence band. The traps located at the midgap or very deep in the bandgap that can trap both electrons and holes are known as the generation-recombination centers.

The emission probability of the deep levels shows an exponential dependence on its energy level with respect to the conduction or valence band. The most effective centers are the generation-recombination centers located at the midgap with equal electron and hole emission probability. For low temperatures, the traps located at the upper half of the bandgap act as electron traps and the traps of downer midgap act as hole traps. Figure 2-1 illustrates the difference between an electron trap, a hole trap and a G-R center. Wider arrows correspond to the higher probability of carrier capture. Note that at the high temperatures, traps can exhibit more complicated manner.

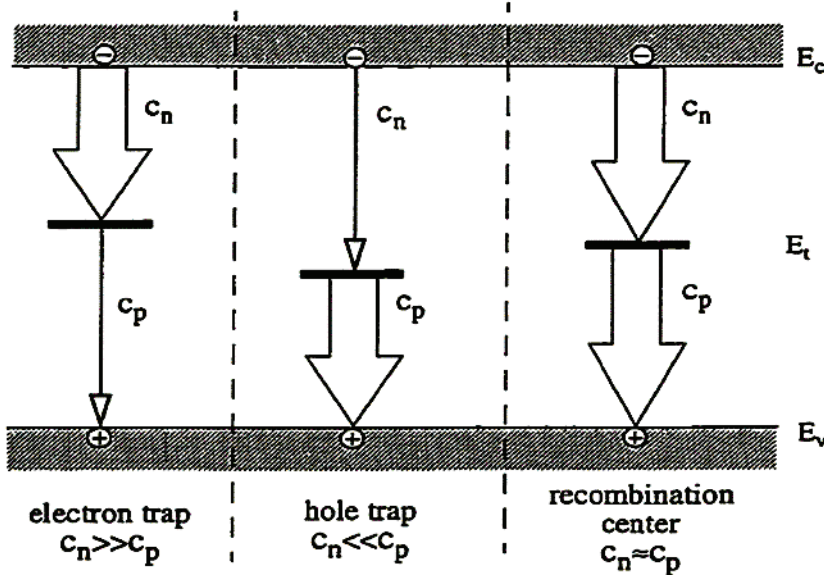


Figure 2-1: Illustrating the difference between electron trap, hole trap and G-R center due to carrier capture probability [37].

Determining the properties of the deep levels is not as easy as the shallow level impurities. The point defects offer specific and discontinuous energy levels while the surface defects such as dislocations create continuous energy levels. Therefore, dislocation defects exhibit more complicated behavior. Identifying different kinds of deep levels is possible by the DLTS measurement.

Small recombination lifetime is required for some optoelectronic devices such as the fast switches and LEDs. In such devices the deep level impurities can be beneficial. Accordingly, impurities are intentionally introduced in order to decrease the lifetime. Adding impurities can cause contribution of the unwanted atoms into the semiconductors. For such a case, precise control over the impurities is required. Finally, it can be concluded that determining the trap properties is very important for optimizing the electrical and optoelectrical devices.

2.2 Generation Recombination Process

The creation of the electrons and holes is called generation process, where the annihilation of the electron and hole pairs is known as recombination process.

Generation and recombination processes occur through the bandgap of the semiconductors. There are four general generation-recombination mechanisms [38];

- a) Band-to-band Recombination
- b) Auger Recombination
- c) Shockley-Read-Hall (SRH) Recombination.
- d) Surface Recombination

Definition of the equilibrium state and steady state is required for explaining the generation process. The equilibrium state refers to the state that the device is not subjected to any external forces such as the electric field. When devices are exposed to the external forces for a long time, the parameters and electrical properties become independent of time. This situation is known as steady state.

The generation process occurs in two ways. The first type of generation is known as the thermal generation. It occurs in both the equilibrium and non-equilibrium states. The second type of the generation takes place under the non-equilibrium states. It is due to the external forces such as illumination or carrier injection.

2.2.1 Direct band-to-band recombination

Direct band-to-band recombination is also known as the radiative recombination. During this process, a free electron from the conduction band transfers to the valence band and annihilates a hole. The electron transfer occurs through losing energy in the form of the photon energy ($h\nu$). Figure 2-2 illustrates the mechanism clearly.

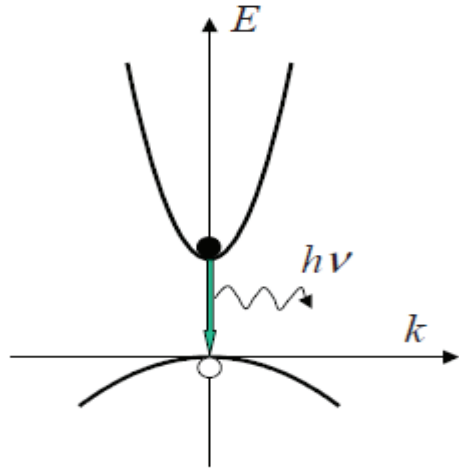


Figure 2-2: Recombination mechanism of an electron hole pair with same wave vector [38].

The rate of the process depends on the electron concentration of the conduction band and hole concentration of the valence band. It can be defined as,

$$R = r(T)n(t)p(t) \quad (2-1)$$

where $n(t)$ is the electron concentration of the conduction band, $p(t)$ is the valence band hole concentration, and $r(T)$ is the recombination coefficient in terms of $\text{cm}^3\cdot\text{s}$

2.2.2 Auger Band-to-Band Recombination

Auger recombination process is based on the recombination of the conduction band electrons with holes in the valence band. The released energy due to the recombination process through Auger mechanism interacts with a third carrier. The third particle can be a hole or electron which is known as the Auger electron or Auger hole. By considering the type of the third particle the mechanism can be divided into the three main types as a) CHCC, b) CHLH, c) CHSH. Figure 2-3 illustrates the difference between these mechanisms.

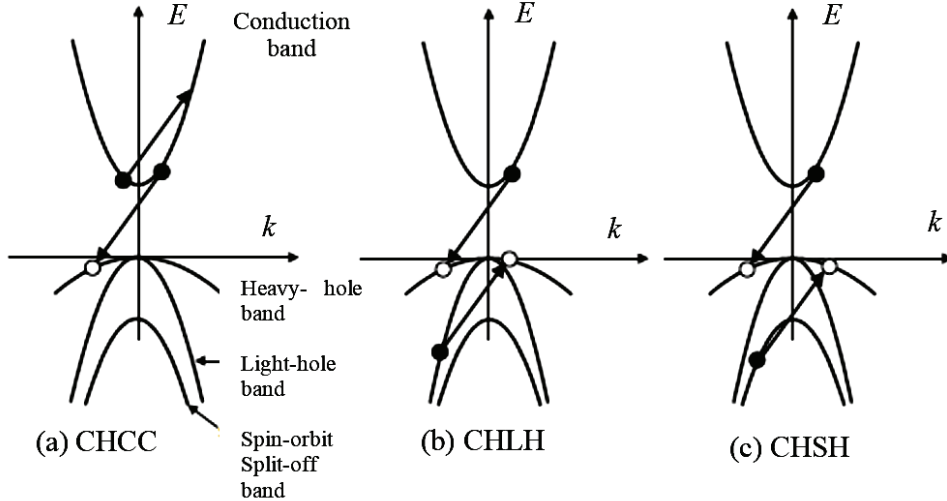


Figure 2-3: Auger recombination process. The released energy due to electron recombination interacts with, A) an electron in conduction band and excited electron remains there, CHCC b) a hole in valence band and causes recombination of hole with an electron in LH band, CHLH c) a hole in valence band and causes recombination of hole with an electron in split-off band [38].

The first type of the Auger recombination is called CHCC mechanism. In this process, the un-bonded energy due to the electron recombination interacts with another electron carrier in the conduction band. This interaction results in the excitation of the electron to a higher level in the conduction band.

The other two processes are based on the interaction of the released energy with a hole in the valence band. During the second process, called CHLH, released energy interacts with a hole in the valence band. It leads to excitation of an electron from the light hole band (LH) to the heavy hole band (HH). For the last type, namely CHSH, the interaction between the released energy and the hole in valence band results in the excitation of the electron from the split-off band to the HH band.

The total recombination rate for Auger mechanism can be obtained by adding the recombination rate of the three mechanisms. The result can be written as [38]

$$R = R_{CHCC} + R_{CHLH+CHSH} = r_1 n^2 p + r_2 np^2 \quad (2-2)$$

where r_1 is the recombination coefficient for the CHCC process and r_2 is the recombination coefficient for CHLH and CHSH mechanisms with excited holes at the valence band.

2.2.3 Shockley-Read-Hall Recombination

Lattice defects and impurities introduce energy levels through the bandgap. These energy levels can help with the generation-recombination process by capturing or emitting free carriers. This non-radiative process introduced by Shockley, Read and Hall in 1952 was named Shockley-Read-Hall (SRH) recombination mechanism [39].

Four different behaviors can be exhibited by a G-R center located within the bandgap with an energy level of E_T . They are listed as

- a) Capturing an electron from the conduction band (c_n)
- b) Emitting an electron to the conduction band (e_n)
- c) Capturing a hole from the valence band (c_p)
- d) Emitting a hole to the valence band (e_p)

The four listed mechanisms are illustrated in Figure 2-4. Electron recombination center is a level with higher probability for (a) and (b). Otherwise, for higher probability for (c) and (d), the trap is called as a hole recombination center.

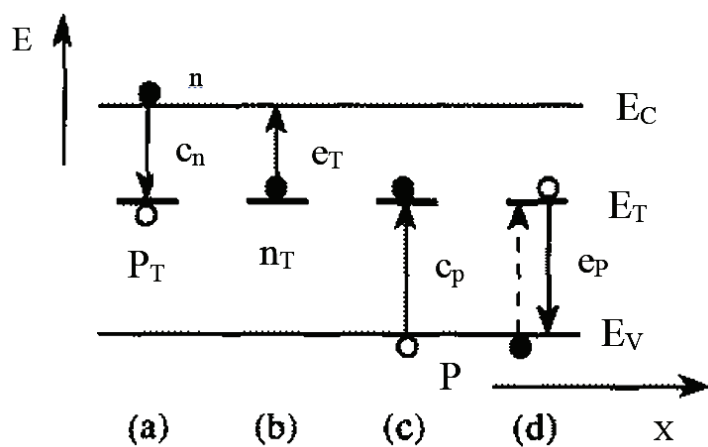


Figure 2-4: How a G-R center with E_T energy level acts within the bandgap **Hata! Başvuru kaynağı bulunamadı..**

The recombination rate of an electron recombination center (R_c) depends on the electron density of the conduction band, density of empty states in the trap ($N_T(1 - f)$) and the speed of the electron interaction with the center ($\sigma_n v_{th}$) where σ_n is the capture cross section, and v_{th} is the thermal velocity. The recombination rate can be expressed as[38]

$$R_c = v_{th} \sigma_n n N_T (1 - f) \quad (2-3)$$

The electron generation rate of the G-R center (G_c) depends on the density of the occupied states in the center and the probability of the electron emission (e_n). It can be expressed as

$$G_c = e_n N_T f \quad (2-4)$$

In the same way, the recombination and generation rate for a hole recombination state can be written as,

$$R_v = v_{th} p N_T f \quad (2-5)$$

$$G_v = e_p N_T (1 - f) \quad (2-6)$$

The electron and hole emission probabilities can be obtained by [38],

$$e_n = v_{th} \sigma_n n_T \quad (2-7)$$

$$e_p = v_{th} \sigma_p p_T \quad (2-8)$$

where n_T and p_T are electron and hole density of traps defined as

$$n_T = N_c \exp \left(\frac{E_T - E_c}{kT} \right) \quad (2-9)$$

$$p_T = N_v \exp\left(\frac{E_v - E_T}{kT}\right) \quad (2-10)$$

In the above expressions, N_v and N_c are the effective densities of states in the valence band and the conduction band. E_c and E_v correspond to the energy levels of the conduction and valence band edges.

The electron and hole recombination lifetimes can be obtained as [38],

$$\tau_{p_0} = \frac{1}{v_{th} \sigma_p N_T} \quad (2-11)$$

$$\tau_{n_0} = \frac{1}{v_{th} \sigma_n N_T} \quad (2-12)$$

2.2.4 Surface Leakage

Surface defects in the crystals generate energy levels distributed throughout the bandgap in the vicinity of the surface. Recombination process through these states takes place at the surface of the semiconductors while all the other recombination processes are bulk mechanisms. The surface recombination is some kind of the SRH recombination. It can be analyzed just like the SRH recombination process. The density of the surface recombination centers are named as $(N_T)_s$. Surface recombination rate is defined as the amount of the recombined carriers per unit area with respect to the time ($\text{cm}^{-2} \cdot \text{s}^{-1}$) and can be expressed as [38],

$$(R - G_t)_s = S_n \Delta n \quad (2-13)$$

where S_n is the surface recombination velocity ($\text{cm} \cdot \text{s}^{-1}$) which is defined as [38]

$$S_n = v_{th} \sigma_n \sigma_p (N_T)_s \frac{n_0 + p_0 + \Delta n}{\sigma_n(n_0 + n_T + \Delta n) + \sigma_p(p_0 + p_T + \Delta n)} \quad (2-14)$$

2.3 C-V measurement

In order to obtain the trap characteristics, it is necessary to know the shallow doping concentration of the specimen. The doping density of semiconductors can be obtained by C-V measurements. Accordingly, the experimental measurement steps for identification of traps should be based on the C-V measurement. This measurement will be followed by C-T measurements.

The depletion region approximation will be accurate for large enough reverse bias. By assuming that there is not any trap in the semiconductor bandgap, changes in the $1/C^2$ versus voltage can be expressed by Equation 2-15 [38,33].

$$1/C^2 = 2(V_R + V_{bi}) / Aq\epsilon N_D \quad (2-15)$$

where A is the area and ϵ expresses the permittivity that depends on the material. By assuming that the sample is uniformly doped with concentration of N_D , Equation 2-15 can be rewritten as;

$$N_D = \frac{2}{Aq\epsilon_s} \left(\frac{d \left(\frac{1}{C^2} \right)}{dV_r} \right)^{-1} \quad (2-16)$$

N_D can be obtained from the slope of the linear plot of $1/C^2$ versus reverse bias voltage. The intersection point of the fitting curve of $1/C^2$ and the x-axis corresponds to v_{bi} . The depletion region approximation will not be accurate for very small v_r or the junction under forward bias. In that case, Equation 2-15 becomes a rough approximation. Under forward bias, the junction capacitance equation can be written as [40]

$$\frac{1}{C^2} = \frac{2}{q\epsilon_s N_d} \frac{v_{bi} - v_f - \frac{kT}{q} + \frac{kT}{q} \exp(\frac{v_f - v_{bi}}{kT/q})}{[1 - \exp(\frac{v_f - v_{bi}}{kT/q})]} \quad (2-17)$$

where v_f is the applied forward bias over the junction. According to 2-17 there is not a linear relationship between $\frac{1}{C^2}$ and v_f . In this case, in order to get the built-in voltage, the following equation can be deduced [40]

$$v_{bi} = v_f - \frac{kT}{q} + \frac{kT}{q} \exp\left(\frac{v_f - v_{bi}}{kT/q}\right) \quad (2-18)$$

It is possible to employ the C-V measurements to get the doping profile for the semiconductors with non-uniform doping as well. In order to get more accurate doping profile more reverse bias steps are needed. It is possible to show that for each value of the applied reverse bias, the doping concentration for the specific depletion region width can be obtained from Equation 2-19 given as

$$N_d(W) = \frac{2}{q\epsilon_s} \left[\frac{d\left(\frac{1}{C^2}\right)}{dv_r} \right]^{-1} \quad (2-19)$$

where W is the depletion region width.

The doping profile can be obtained by repeating the C-V measurement for the various depletion region widths due to the different reverse bias voltage values.

2.4 Effect of Deep Level Traps on Junction Capacitance

Deep levels existing in the depletion region affect the junction capacitance of a p-n diode. In order to survey the effects of deep levels, an n-type Schottky diode with a donor trap with the concentration of N_T , positioned at E_T energy level is assumed. Consider the energy band diagram of this junction illustrated in Figure 2-5. If a

reverse bias is applied to the junction, (following forward bias), the width of the depletion region is increased and a larger portion of the traps remain above the Fermi level. The filled traps with energies above the Fermi level start to emit electrons. Electron emission from the traps increases the positive charge in the depletion region and calls for a decrease in the depletion region until all traps above E_F emit electrons. The reduction in the depletion region results in a transient increase in the depletion capacitance of the junction. The deep level divides the depletion region into two parts. Intersection point of Fermi level and deep level trap is the boundary of the two parts [41].

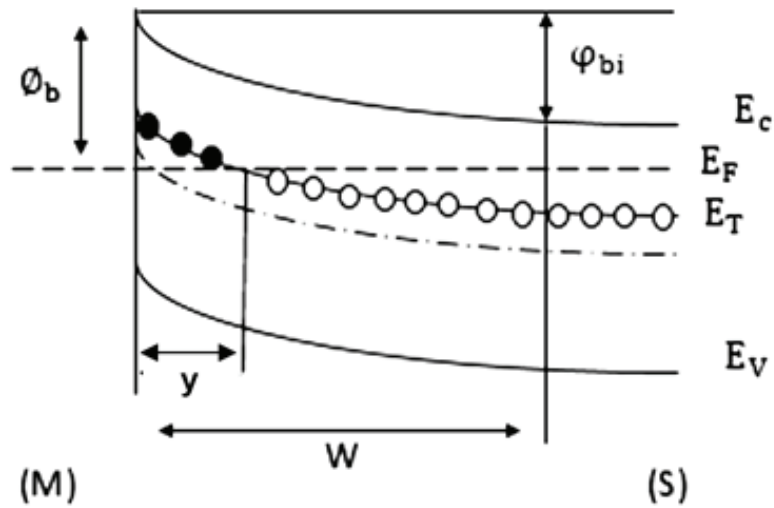


Figure 2-5: Energy band diagram of a Schottky barrier with a donor level trap.

The part between the intersection point and depletion region edge is called transition region and it can be obtained from equation below [40];

$$\lambda = W - y = \sqrt{2}L_D \left(\frac{E_F - E_T}{kT} \right) \quad (2-20)$$

where, L_D is called the Debye length of the semiconductor and can be obtained from;

$$L_D = \sqrt{\frac{\epsilon_s kT}{q^2 N_d}} \quad (2-21)$$

Debye length is a material parameter in the semiconductors. It depends on the semiconductor type, temperature and the impurity concentration. It refers to a length over which the electric field influences the charge density. It is reversely proportional to the doping density.

Generally, for a C-V measurement, summation of a large DC voltage and a small AC voltage is needed. The junction will be under reverse bias by applying the large DC voltage, which creates depletion region. AC voltage is applied to the junction in order to measure the depletion region capacitance by measuring the phase difference. The applied AC voltage leads to the fluctuation of the depletion region edges in the boundaries, which were identified by the applied DC voltage. Amount of this fluctuation depends on the amplitude of the AC voltage. While according to equation 2-20, λ is independent of the applied voltage for the small amplitudes of AC voltage, W and y change with the AC voltage variations. This change causes in the fluctuation of the intersection point of the Fermi level and the trap level [40]. If thermal emission rate of traps are much larger than the AC voltage frequency, the traps around the y point will be able to catch the voltage variations by capturing and emitting electrons frequently [40]. In that case, the change in the depletion region width (ΔW) and the change in the y point position (Δy) are defined by the variations of the applied reverse bias (Δv_r). Electrical charge value in the depletion region changes by $q(N_d \Delta w + N_T \Delta y)$ [36]. Figure 2-6 illustrates the energy band diagram for a Schottky diode and the effect of the applied reverse bias on the electric field in the depletion region.

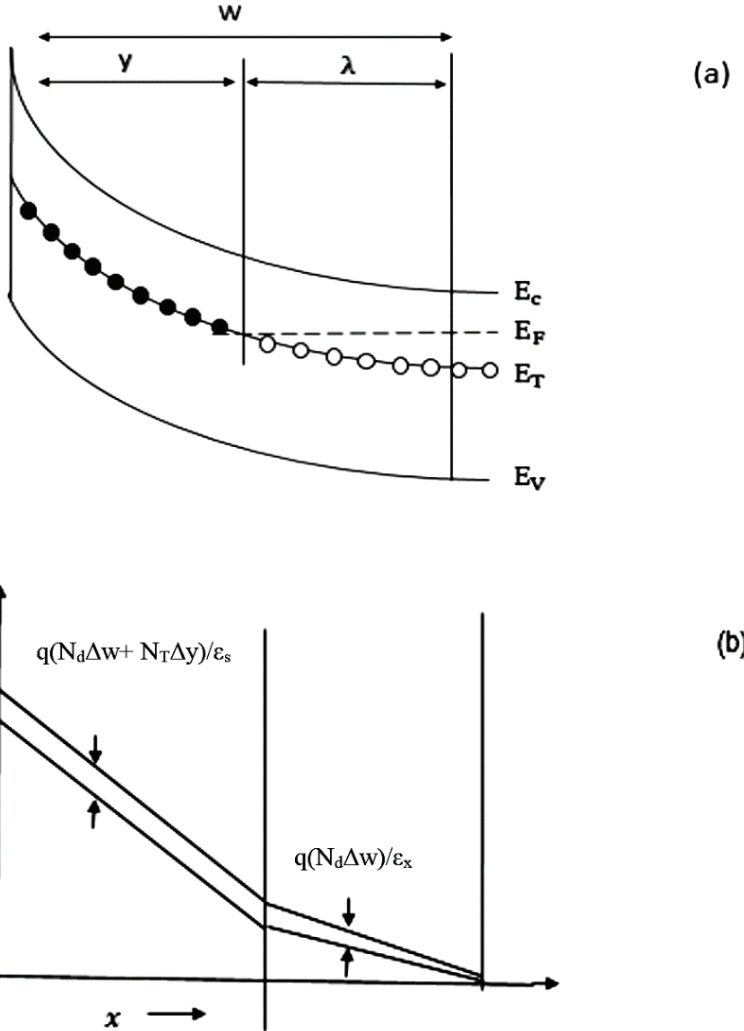


Figure 2-6: a) Energy band diagram of a Schottky barrier with a donor trap level under reverse bias. b) Effect of the applied reverse bias on the electric field in depletion region [41].

As mentioned previously, the depletion region width (w) and the y point are steady for small bias voltage variations (small Δv_r). In that case, Δw becomes equal to the Δy and leads to a modification in the electric charge amount by $q(N_d + N_T)\Delta w$.

The traps with the thermal electron emission rate much smaller than AC voltage frequency located around the y point cannot follow the voltage variations and remain full. In that case, the bias voltage variations Δv_r leads to a change in the electrical charge value about $qN_d\Delta w$ [40].

Generally, the junction capacitance per area can be obtained by [40]

$$C = \left[\frac{\varepsilon_s q A N_d}{2(V_r + \varphi_{bi})} \right]^{1/2} \left(1 + \frac{e_n^2}{e_n^2 + \omega^2} \frac{N_T}{N_d} \right) \quad (2-22)$$

where, ω is the angular frequency of the applied voltage over the junction and e_n is the thermal electron emission rate of the traps. In order to obtain accurate value for Equation 2-22, depletion region approximation is assumed.

In Equation 2-22, two parameters have to be considered. First parameter is the ratio of the trap concentration to the doping concentration $\left(\frac{N_T}{N_d}\right)$. The second one is the AC voltage frequency with respect to the thermal emission rate of the electrons.

For $N_T \ll N_d$, the traps can be neglected, which is the common condition for most of the experiments, and Equation 2-22 converts to Equation 2-15. In that case, it is possible to obtain N_d from C-V measurement with a negligible error. C_∞ Shows the capacitance for this condition and can be obtained from [40];

$$C_\infty = \left[\frac{\varepsilon_s q A N_d}{2(V_r + \varphi_{bi})} \right]^{1/2} \quad (2-23)$$

For $\omega \ll e_n$, capacitance depends on the trap concentration. The capacitance for this case is called C_0 defined as [40]

$$C_0 = \left[\frac{\varepsilon_s q A N_d}{2(V_r + \varphi_{bi})} \right]^{1/2} \left(1 + \frac{N_T}{N_d} \right) = C_\infty \left(1 + \frac{N_T}{N_d} \right) \quad (2-24)$$

Equations 2-24 and 2-23 illustrate the maximum and minimum boundaries of the capacitance value for different frequencies. The difference of the two equations is given as;

$$\Delta C = C_\infty \frac{N_T}{N_d} \quad (2-25)$$

For $N_T \ll N_d$, this difference can be written as $\Delta C \cong 0$; otherwise ΔC has a considerable value.

Another considerable point about equation 2-22 is the fact that the equation is used to obtain steady state capacitance. It does not cover transient capacitance. The transient capacitance will be studied at the next section. It is important to mention that, for large trap concentrations ($N_d \ll N_T$), the C-V measurement should be done under much more accurate conditions.

2.5 Transient Capacitance Measurements

Presence of the trap levels and the thermal emission of the carriers from traps originates the transient capacitance of the junction. By applying reverse bias pulse, the depletion region width increases. The part of the traps existing in the depletion region with energy levels higher than the Fermi level starts emitting carriers. As a result, the transient capacitance of the junction changes due to the electrical charge variation of the depletion region with respect to time. Figure 2-7 presents the depletion region changes after the electron emission from traps. This time-varying depletion region width leads to a time-varying capacitance. Capacitance variations depend on many parameters, but generally, it is an exponential decay. Figure 2-7 shows the energy band diagram of a Schottky diode with an n-type semiconductor and a trap level of E_T under zero bias and reverse bias.

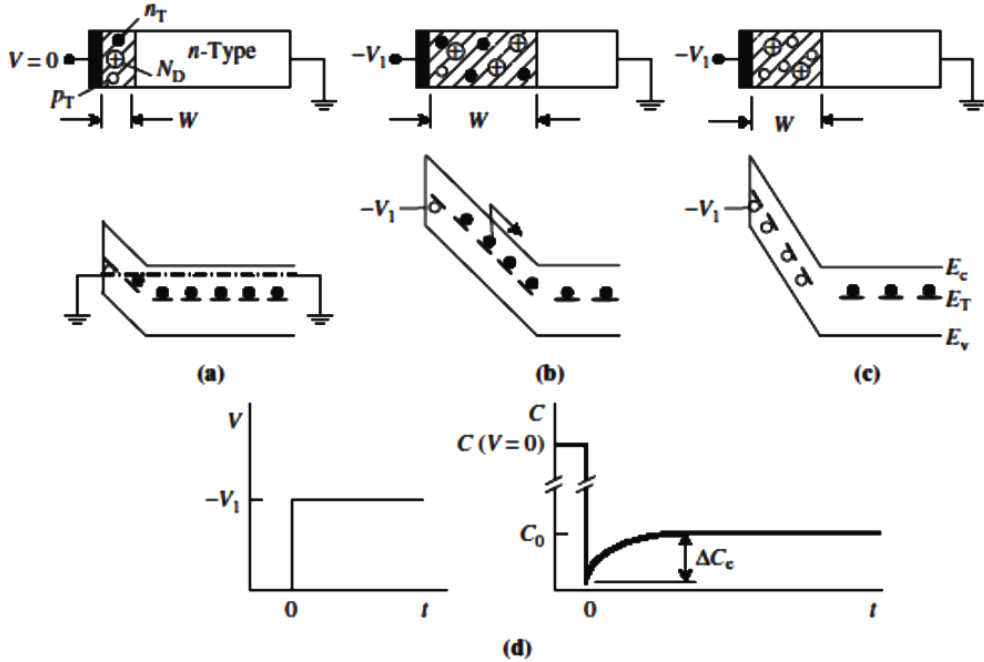


Figure 2-7: A Schottky diode for (a) zero bias (b) reverse bias at $t=0$, (c) reverse bias as $t\rightarrow\infty$. The applied voltage and resultant capacitance transient are shown in (d) [33].

Occupied trap concentration can be obtained by [36];

$$n_T(t) = n_T(0) \exp\left(-\frac{t}{\tau}\right) \quad (2-26)$$

$$+ \frac{(e_p + c_n n) N_T}{e_n + c_n n + e_p + c_p p} \left(1 - \exp\left(-\frac{t}{\tau}\right)\right)$$

where $n_T(0)$ is the density of the occupied G-R centers at $t=0$ and $\tau = 1/(c_n + c_n n + e_p + c_p p)$. The density at steady-state condition ($t \rightarrow \infty$) depends on both electron and hole densities and the emission and capture rates as follows

$$n_T = \frac{e_p + c_n n}{e_n + c_n n + e_p + c_p p} N_T \quad (2-27)$$

Most of the deep-level measurements are performed based on Equations 2-27 and 2-26 [36].

For n-type semiconductor, hole density (p) can be neglected. Let e_p to be neglected for the trap located at upper half of the band gap with $e_n \gg e_p$. Then, Equation 2-26 can be rewritten and simplified for the time dependence of n_T and the initial emission period as given below

$$n_T(t) = n_T(0) \exp\left(-\frac{t}{\tau_e}\right) \approx N_T \exp\left(-\frac{t}{\tau_e}\right) \quad (2-28)$$

By assuming depletion region approximation, it is possible to neglect the recombination process of the electrons and the generation-recombination process of the holes in the depletion region for n-type sample. Following equation can be deduced as a result [36]

$$\frac{\partial n_T}{\partial t} = -e_n n_T = -G_n \quad (2-29)$$

where n_T is the density of the occupied states, e_n is the emission rate of the electrons and G_n is the generation rate of the electrons. Equation 2-28 illustrates that the density of the occupied states is an exponential function of time. The time constant can be written as $\tau = 1/e_n$. By assuming $n_T(0) = N_T$ [36]

$$n_T(t) = N_T \exp(-e_n t) \quad (2-30)$$

For donor type traps, traps become positively charged due to the electron emission. The positive charge density of traps is defined as below;

$$p_T(t) = N_T - n_T(t) = N_T [1 - \exp(-e_n t)] \quad (2-31)$$

Accordingly, while transient voltage applied over the junction remains constant, the junction capacitance changes ($\Delta C(t)$). The junction capacitance depends on the charge density variations of the depletion region ($p_T(t)$) by

$$\Delta C(t) = \alpha p_T(t) = \alpha N_T [1 - \exp(-e_n t)] \quad (2-32)$$

Figure 2-8 shows the capacitance change of the junction in the presence of a majority carrier trap under the applied zero bias and reverse bias. At the beginning, junction is under reverse bias and it is at steady state. The capacitance under this situation is called C_{ss} . At the second step, zero bias is applied and the depletion region gets narrower.

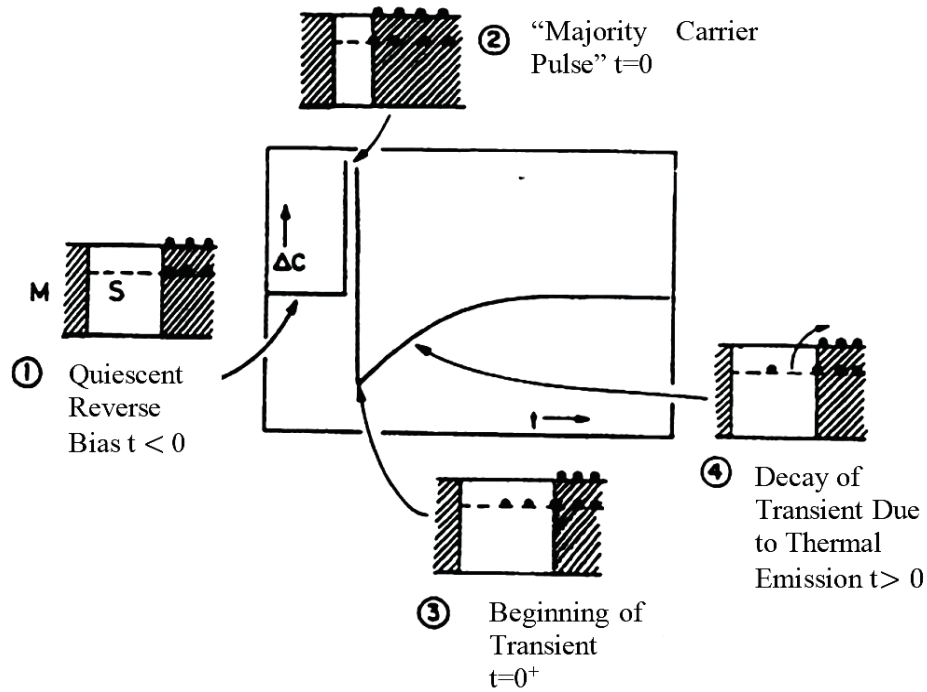


Figure 2-8: Capacitance transient under thermal emission of carriers from majority carrier traps [33].

It is assumed that all the traps outside the depletion region are fully occupied during the zero bias. The capacitance after applying the reverse bias ($C(0)$) can be defined as;

$$C(0) = \left[\frac{\varepsilon_s q A N_d}{2(V_r + \varphi_{bi})} \right]^{1/2} \quad (2-33)$$

Traps get unoccupied due to the thermal emission of the electrons from traps under the reverse bias. Increase in the positive charge density of the depletion region leads to an increment in the capacitance value till it reaches C_{ss} [36].

$$C_{ss} = \left[\frac{\varepsilon_s q A (N_d + N_T)}{2(V_r + \varphi_{bi})} \right]^{1/2} \quad (2-34)$$

The rate of capacitance change from $C(0)$ to C_{ss} is shown in Equation 2-32. The total capacitance change can be referred by ΔC_{tot} and obtained by

$$\Delta C_{tot} = C_{ss} - C(0) = \alpha N_T \quad (2-35)$$

Finally, by combining equations 2-32 and 2-35 the following equation can be expressed [33]

$$C(t) = C_{ss} - \Delta C_{tot} \exp(-e_n t) \quad (2-36)$$

DLTS measurement is performed based on Equation 2-36. The other considerable point is the relationship between the trap density (N_T) and the total capacitance change (ΔC_{tot}). According to Equations 2-34 and 2-33, the following relationship can be deduced [33]

$$C_{ss}^2 - C^2(0) = \frac{N_T}{N_d + N_T} C_{ss}^2 \quad (2-37)$$

Now, by taking $C_{ss} - C(0) = \Delta C_{tot}$ into consideration

$$\Delta C_{tot}[C_{ss} + C(0)] = \frac{N_T}{N_d + N_T} C_{ss}^2 \quad (2-38)$$

For $N_T \ll N_d$ (which is generally accurate), it can be concluded that ΔC_{tot} is small enough for satisfying $C_{ss} + C(0) \cong 2C_{ss}$. As a result, the following equation can be obtained

$$\frac{\Delta C_{tot}}{C_{ss}} = \frac{N_T}{2N_d} \quad (2-39)$$

The trap density in DLTS measurements is calculated based on Equation 2-39.

By combining Equations 2-35 and 2-39, Equation 2-32 can be rewritten as [33]

$$\frac{\Delta C(t)}{C_{ss}} = \frac{N_T}{2N_d} [1 - \exp(-e_n t)] \quad (2-40)$$

All the equations brought in this chapter are accurate for the situation where the transition width (λ) is ignored with respect to depletion region width (W_r). Also, the reverse bias voltage should be large enough in order to ignore the depletion region width under zero bias (W_0) compared to W_r . Otherwise, Equation 2-40 should be modified as [40]

$$\frac{\Delta C(t)}{C_{ss}} = \frac{(W_r - \lambda)^2 - (W_0^T)^2}{W_r} \frac{N_T}{2N_d} [1 - \exp(-e_n t)] \quad (2-41)$$

where W_0^T is the distance between the intersection point of E_F and E_T and the junction barrier under zero bias. If the sample under the measurement is a Schottky diode, then, forward bias is generally used instead of zero bias. W_0^T can be ignored in that situation [40]

$$\frac{\Delta C(t)}{C_{ss}} = \frac{(W_r - \lambda)^2}{W_r} \frac{N_T}{2N_d} [1 - \exp(-e_n t)] \quad (2-42)$$

2.6 Principle of DLTS Measurement Method

The capacitance transition is an exponential function of the time. The time constant is inversely proportional to the thermal emission rate of the carriers. The thermal emission rate of the carriers is a function of temperature. Therefore, capacitance transition is a function of temperature. In DLTS method, this dependence is used in order to get the capacitance variation spectra with respect to the temperature. As it was defined previously, this spectrum is a result of a C-T measurement [36].

The thermal emission rate of the carriers should be defined in order to elaborate the method. The parameter can be expressed as [34]

$$e_n = \sigma_n v_{th} N_c \exp\left(-\frac{\Delta E_T}{kT}\right) \quad (2-43)$$

where σ_n is the capture cross section of an electron trap, v_{th} is the thermal velocity of electrons, N_c is the effective density of energy states in the conduction band, ΔE_T is the activation energy of the electron trap level, T is the temperature and k is the Boltzmann constant.

Equation 2-43 is the basic relation for the DLTS method and includes two important parameters of a deep level: σ_n and ΔE_T . On the other hand, it was mentioned that e_n^{-1} is the time constant of the transient capacitance. The trap parameters can be obtained by measuring the transient capacitance, respectively. Since e_n depends on the temperature based on equation 2-43, then, the transient capacitance is a temperature dependent parameter as well. It should be noted that both the exponential dependence of the equation and the dependence of the thermal velocity and conduction band density of the states on the temperature should be taken into the consideration.

Exerting a reverse bias after applied forward bias leads to the capacitance transient. Bias pulse can be applied over p-n junctions (it could be p^+ -n or n⁺-p junction) in two different ways. These procedures are called the injection pulse and a majority carrier pulse. For the first method, a positive voltage is utilized over the diode. While, diode is under forward bias, minority carriers are injected. It causes occupation of both majority and minority carrier traps. This pulse is called saturating injection pulse. Figure 2-9 illustrates the trap level status and depletion region of an n⁺-p junction before, during and after the pulse application. It also illustrates the capacitance transient due to the minority carrier traps [34].

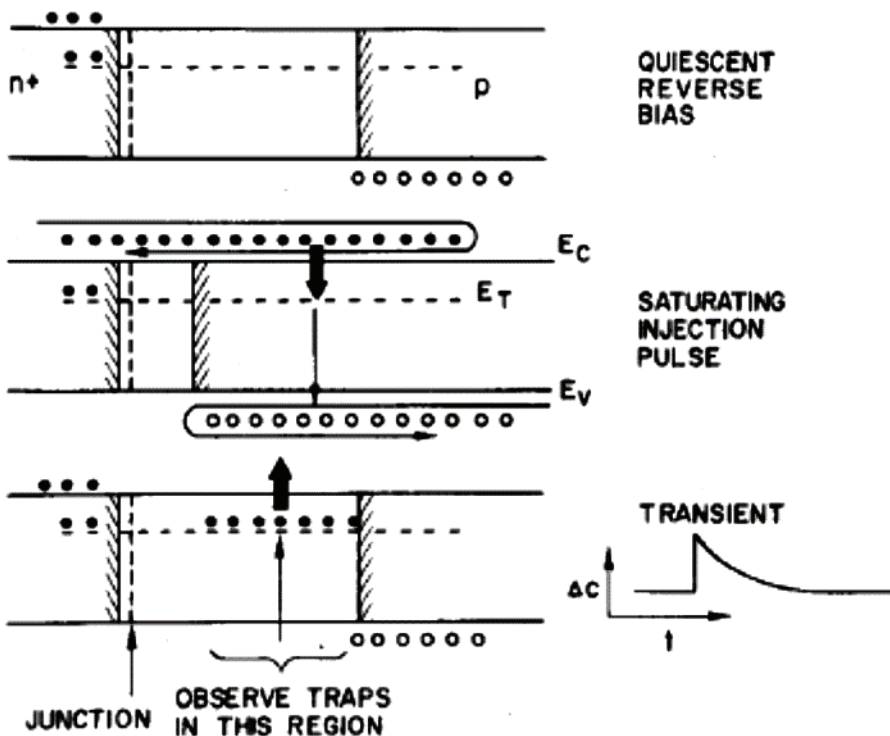


Figure 2-9: Effects of saturating injection pulse on n⁺-p junction and minority carrier trap level [34].

For the second type of the bias pulse, called majority carrier pulse, a zero bias or negative bias pulse is applied over the diode. In fact, during the process, the reverse bias decreases and the depletion region width becomes narrower. In this condition,

there is not any current flow over the diode, thus, just the majority traps become occupied.

Figure 2-10 presents the trap level status and depletion region of an n^+ -p junction, before, during and after the majority carrier pulse application. It also illustrates capacitance transient due to majority carrier traps [34].

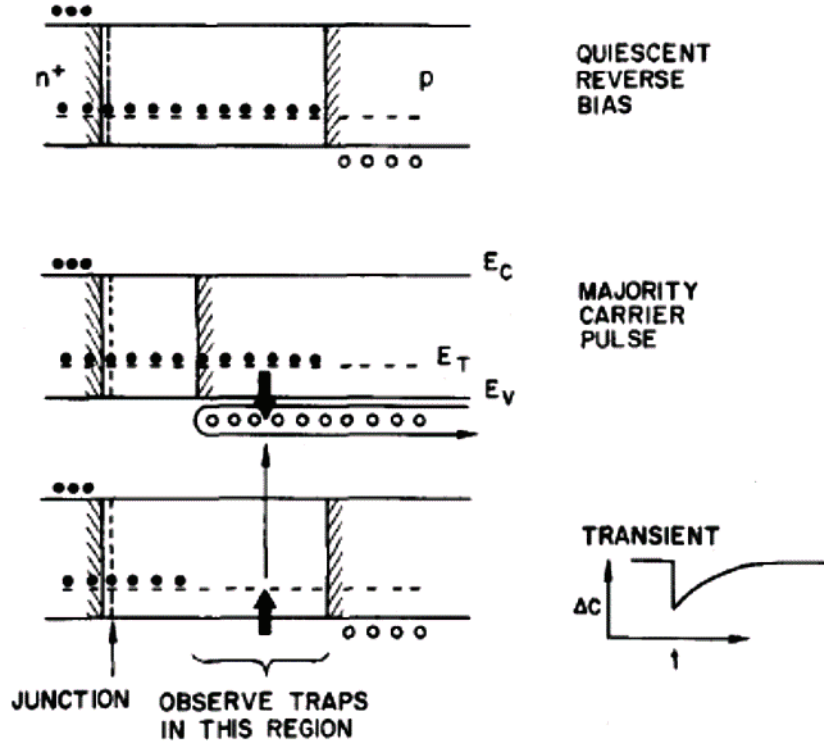


Figure 2-10: Effects of majority carrier pulse on n^+ -p junction and majority carrier trap level [34].

Overall, in order to provide capacitance transient for a quiescent junction under reverse bias, for the first step, a saturating injection pulse or a majority carrier pulse should be applied. Generally, this pulse is called filling pulse because of the occupation of the traps by carriers. For the second step, a reverse bias is applied over the junction. Traps start emitting carriers under reverse bias leading to capacitance transient.

In DLTS measurements, capacitance transient can be obtained by applying periodic filling pulses while temperature changes in a defined range. Thermal emission rate e_n is small for low temperatures. It means that emission time constant of traps ($\tau_e = e_n^{-1}$) is high, which results in slow and long transients. On the other hand, e_n becomes larger for higher temperatures. It leads to a small emission time constant of the traps and capacitance transient time. It causes fast and short capacitance transient. Figure 2-11 shows this dependence.

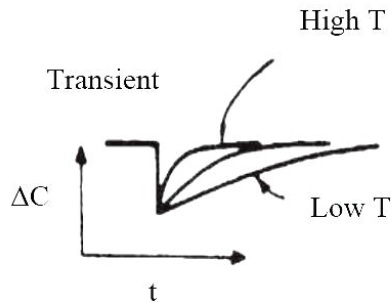


Figure 2-11: Effect of temperature on capacitance transient time and speed [41].

The basic idea for the DLTS method is to employ an emission rate window for capacitance measuring. By the thermal scanning of junction under the periodic filling pulses, different values for e_n can be obtained. Maximum value for the capacitance change is observed exactly at the temperature point where the thermal emission rate of the traps is within the emission rate window. It can be concluded that, if emission rate window varies for each thermal scanning, the corresponding emission rate of traps occurs at a different temperature. The dependence of the emission rate of the traps on the temperature is utilized by repeating this experiment for various emission rate windows. Figure 2-12 explains the emission rate window in DLTS method.

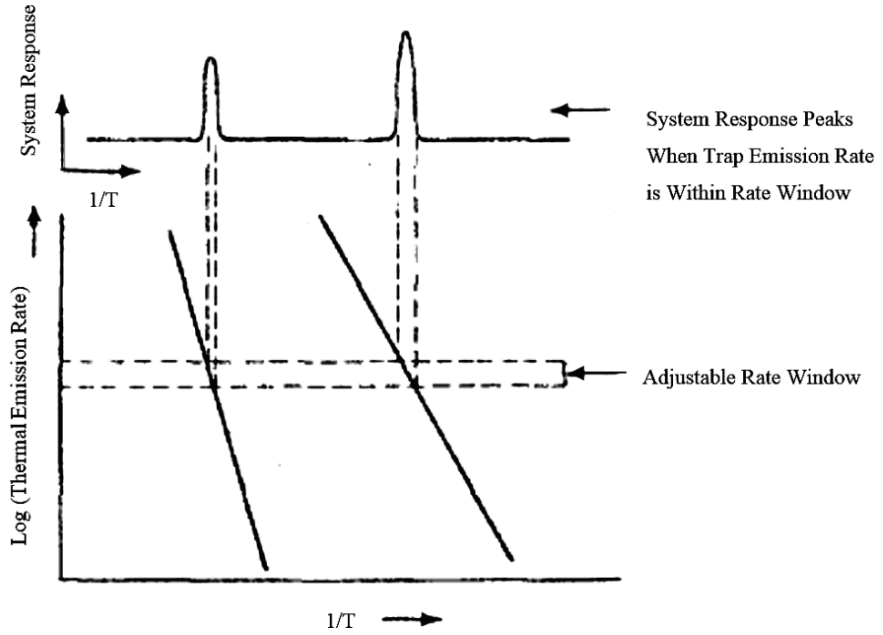


Figure 2-12: Rate window concept (basic idea of DLTS) [34].

The activation energy diagrams for two separated traps are provided at the lower part of Figure 2-12. Upper part presents the results for a well-defined emission rate window obtained by the capacitance transient measurement setup. Peak response point of the measurement can be observed at two different temperatures, which means in two different emission rates [34].

Different methods are introduced for defining the emission rate window, which is one of the most important differences among the DLTS measurement set-ups. The first method was defined by Lang, which is known as double boxcar averaging. In this method, capacitance transient for two different time values are measured by a fast capacitance meter. Normalized DLTS signal, which is a function of temperature, can be defined as;

$$S(T) = \frac{C(t_2) - C(t_1)}{\Delta C_{tot}} \quad (2-44)$$

where t_1 and t_2 are the time values which define the emission rate window.

At low temperatures with slow and long transition, measured capacitances at t_1 and t_2 are very close. The $S(T)$ signal value will be small for such a condition. This is accurate for high temperatures as well, because at these temperatures capacitance transient is very fast and the values of the capacitance for t_1 and t_2 are close. The capacitance difference at t_1 and t_2 can be considerable for moderate temperatures. The $S(T)$ signal will have a maximum value at a certain temperature point. This maximum point position depends on values of t_1 and t_2 . The $S(T)$ signal is the spectra of capacitance differences versus temperature. By surveying the peak points of this spectrum, significant trap parameters can be obtained.

Figure 2-13 shows that the maximum point position of the signal changes by varying values of t_1 and t_2 , which means variation of emission rate window.

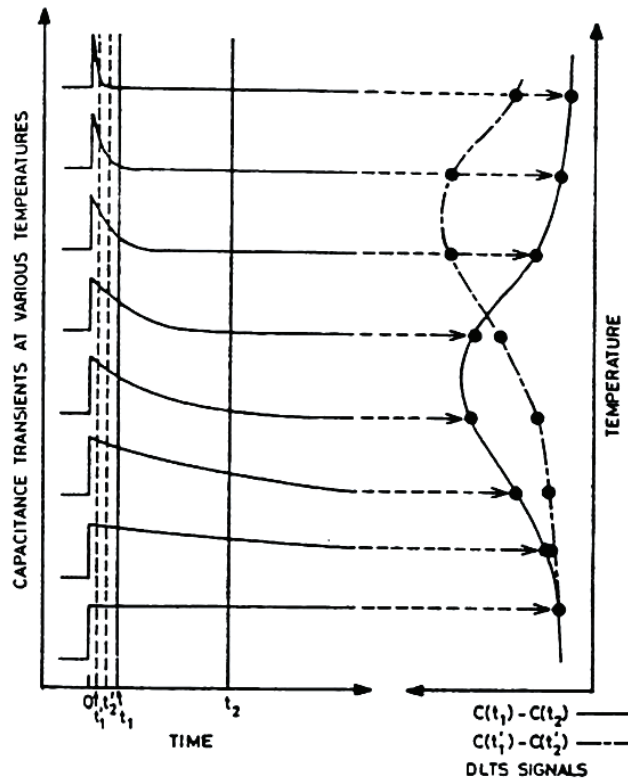


Figure 2-13: Illustration of how a double boxcar is used to define the rate window [34].

In order to get the relationship between the emission rate window and $S(T)$, the signal should be written with respect to the thermal emission rate. By inserting Equation 2-36 into Equation 2-44, the following equation can be obtained [36]

$$S(T) = \exp(-e_n t_1) - \exp(-e_n t_2) \quad (2-45)$$

The dependence of $S(T)$ to the temperature through e_n can clearly be seen in Equation 2-45. Indeed Equation 2-45 is the mathematical definition of Figure 2-13. The temperature point related to the peak point is called T_{max} . Properties of the peak point of the DLTS signal can be obtained by taking the derivative of Equation 2-45 with respect to e_n . The maximum value of e_n related to the DLTS spectra peak at T_{max} is called e_{nmax} . By considering $\frac{\partial S(T)}{\partial e_n} = 0$, the following equation can be obtained

$$e_{nmax} = \frac{\ln(t_2/t_1)}{t_2 - t_1} \quad (2-46)$$

Equation 2-46 illustrates the definition of the emission rate window value (which relates to e_{nmax}) at measurement times t_2 and t_1 . It denotes the peak position of the DLTS signal.

By inserting Equation 2-46 into Equation 2-45, the peak amplitude of normalized DLTS signal can be deduced as [36]

$$S(T_{max}) = \left(1 - \frac{t_1}{t_2}\right) \exp\left[-\frac{\ln(t_2/t_1)}{t_2 - t_1}\right] \quad (2-47)$$

Trap density can be obtained by measuring the peak amplitude of the DLTS signal. The peak amplitude of signal (ΔC_{max}) can be defined as;

$$\Delta C_{max} = [C(t_2) - C(t_1)]|_{T=T_{max}} \quad (2-48)$$

Following equation can be written based on Equation 2-44;

$$\Delta C_{max} = \Delta C_{tot} S(T_{max}) \quad (2-49)$$

Density of the traps can be calculated by taking Equation 2-39 into account;

$$N_T = \frac{2\Delta C_{tot}}{C_{ss}} N_d \quad (2-50)$$

By combining Equations 2-50 and 2-49 [36]

$$N_T = \frac{2\Delta C_{max}}{S(T_{max}) C_{ss}} N_d. \quad (2-51)$$

where C_{ss} and N_d can be obtained by C-V measurement and $S(T_{max})$ can be provided by setting the proper t_2 and t_1 values. Equation 2-51 shows the relation between the trap density and the peak amplitude of the DLTS signal. Activation energy and capture cross section are the two important parameters of traps that can be derived from e_{nmax} measurements [36].

Equation 2-43 can be rewritten in terms of the temperature and the parameters independent of the temperature. For $v_{th} = \left(\frac{3kT}{m^*}\right)^{1/2}$ and $N_c = 2\left(\frac{2\pi m^* k T}{h^2}\right)^{3/2}$,

$$e_n = A_0 \sigma_n T^2 \exp\left(-\frac{\Delta E_T}{kT}\right) \quad (2-52)$$

where A_0 is constant and is defined as

$$A_0 = 2\sqrt{3}\left(\frac{2\pi}{h^2}\right)^{3/2} k^2 m^* \quad (2-53)$$

By employing Arrhenius method, Equation 2-52 can be written as

$$\ln\left(\frac{e_n}{T^2}\right) = \ln(A_0\sigma_n) - \frac{\Delta E_T}{kT} \quad (2-54)$$

According to Equation 2-54 the $\ln\left(\frac{e_n}{T^2}\right)$ plot versus $\frac{1}{T}$ will be a linear plot with the slope of $-\frac{\Delta E_T}{k}$ and the value of the true y-intercept (at $x = 1/T = 0$) will correspond to $\ln(A_0\sigma_n)$. Arrhenius plot can be drawn based on various values of T_{max} for different emission rate windows [34].

Generally, a trap appears as a peak on DLTS signal. Each peak point defines a certain value for T_{max} and e_{nmax} which fits in Equation 2-54 and assigns a point on Arrhenius plot. More data points on Arrhenius plot can be obtained during the thermal scanning of the sample with different emission rate windows. As mentioned before, the Arrhenius plot is a linear plot and two points are enough for calculating the slope and the intercept of the line. However, result will not be accurate in that case. Rapid thermal scanning is used in order to get several points due to the presence of the possible errors because of the measurement conditions. The best-fitted line is chosen in order to calculate the trap parameter by applying curve-fitting technique on points.

Measurement times t_2 and t_1 are chosen as a time range to get high signal to noise ratio in the double boxcar averaging method. Measuring is done at time interval of t_1 and $t_1 + \delta t_1$, and second time interval of t_2 and $t_2 + \delta t_2$. Average capacitance value measured during the first time interval is known as the capacitance of t_1 , and the average capacitance measured during the second time interval is defined as the capacitance of t_2 . The signal to noise ratio will be higher for larger δt values. Otherwise, the capacitance measurement error will be high due to the large temperature and time constant variations during δt . For these conditions, normalized DLTS signal and the thermal emission rate of the peak point of the DLTS signal can be deduced from [36]

$$S(T) = \frac{1}{e_n \delta t} [1 - \exp(-e_n \delta t)][\exp(-e_n t_1) - \exp(-e_n t_2)] \quad (2-55)$$

$$e_{nmax} = \frac{\ln \left[\left(t_2 + \frac{\delta t}{2} \right) / \left(t_1 + \frac{\delta t}{2} \right) \right]}{t_2 - t_1} \quad (2-56)$$

Equation 2-56 is an expression with approximation less than 10%. It can be less for $2 < \frac{t_2}{t_1} < 3$.

The other important discussion for DLTS measurements is selecting a proper emission rate window. It can be done in three modes; (1) t_1 is kept constant and t_2 varies, (2) t_2 is settled constant and t_1 varies, (3) t_1/t_2 is kept constant and, both t_1 and t_2 changes. The last scheme seems to be the most proper one as will be discussed below [34].

For the first method, where t_1 is kept constant and t_2 varies, the peak amplitude of the DLTS will increase by increasing t_2 according to Equation 2-47. On the other hand, for the second method, where t_2 is settled constant and t_1 varies, peak amplitude of DLTS will be smaller for larger t_1 values considering Equation 2-47. Figure 2-14 illustrates the difference with an example.

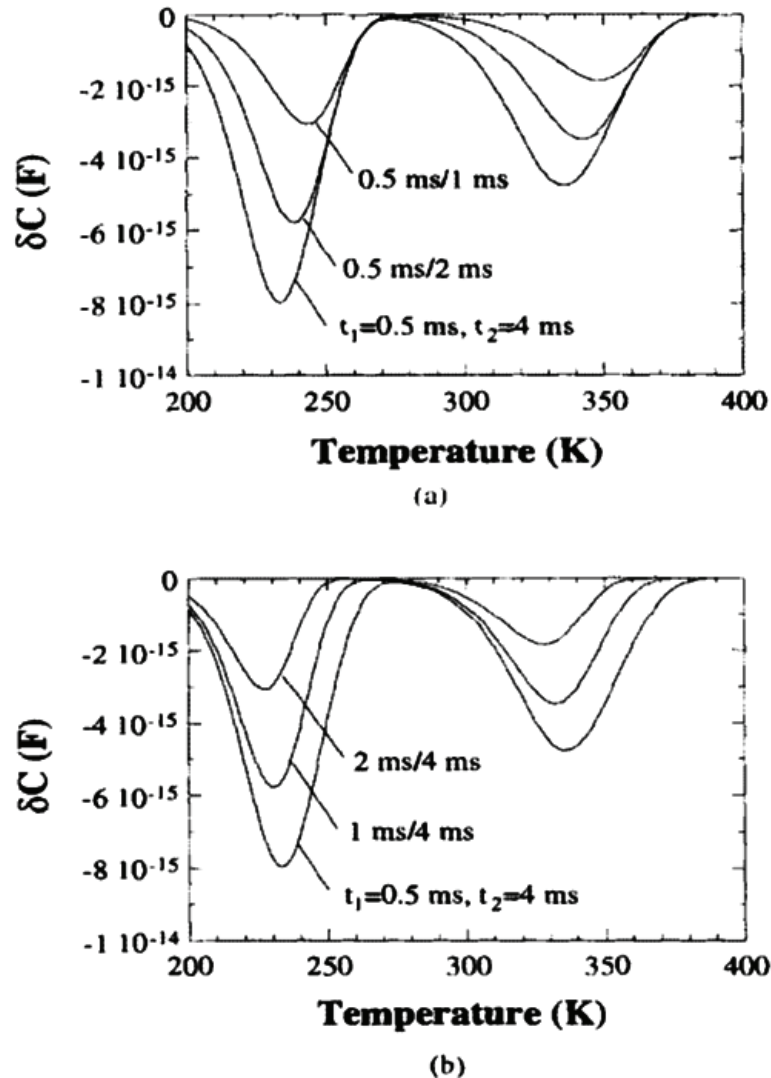


Figure 2-14: DLTS spectra for (a) t_1 fixed, t_2 varied, (b) t_2 fixed, t_1 varied [33].

For a constant t_1/t_2 value, from Equation 2-47, amplitude of the peak points of the DLTS signal $S(T_{max})$ remain same, while the value for the temperature point of the peak (T_{max}) changes [33]. It means that for the third method just the peak position shifts to the higher temperatures for smaller values of the t_1 and t_2 . Figure 2-15 shows the DLTS signal Spectra for n-GaAs illustrating minority traps for five different emission rate windows. Obviously, for constant t_1/t_2 ratio, peaks are fixed in amplitude and varies in position.

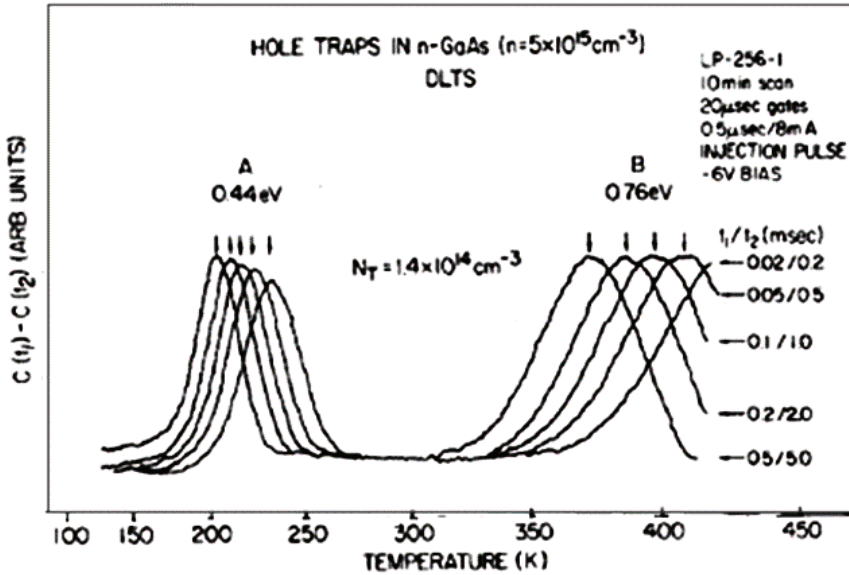


Figure 2-15: Typical experimental DLTS spectra for hole traps in n-GaAs and five different emission rate windows achieved by varying values of t_1 and t_2 [34].

The trap properties can be achieved by employing all the three schemes. The last method seems to be more accessible. The fixed value of the t_1/t_2 ratio and $S(T_{max})$ makes calculations effortless. For constant $\ln(\frac{t_2}{t_1})$, $(e_{nmax})^{-1}$ becomes proportional to the $t_2 - t_1$ considering Equation 2-46.

The other considerable point is selecting the proper value of the t_1/t_2 ratio. Equation 2-47 illustrates that $S(T_{max})$ will be smaller for small t_1/t_2 ratios. It leads to the smaller DLTS peak amplitude (ΔC_{max}) according to Equation 2-49 which is not preferable. Trap determination by DLTS measurement results will be more accurate for larger $S(T_{max})$. As a result, larger t_1/t_2 ratio will be preferred for this purpose. On the other hand, larger t_1/t_2 ratio leads to the smaller values of T_{max} and e_{nmax} based on Equations 2-46 and 2-52. Small t_1/t_2 ratio is suggested since peaks will be shifted to higher temperatures and will become broader. It can be concluded that there is an optimum value for t_1/t_2 ratio which can satisfy both of the above mentioned conditions [33].

Figure 2-16 is the Arrhenius plot obtained for the DLTS spectra peaks illustrated in Figure 2-15. It is achieved by calculating the various points for each peak. The solid lines are achieved by accurate fix-temperature capacitance measurement and the dashed line is a fitting line through the points resulted from DLTS measurements for trap A [34]. The fact that there is a perfect match between results obtained with two different methods is considerable point that shows the high certainty of the DLTS method. The horizontal lines for trap B belongs to the possible errors for the exact peak determination. The activation energy obtained for trap A is 0.76 eV and for trap B is 0.44eV [33]. Calculating the trap density and capture cross section is possible by considering the plots as mentioned before.

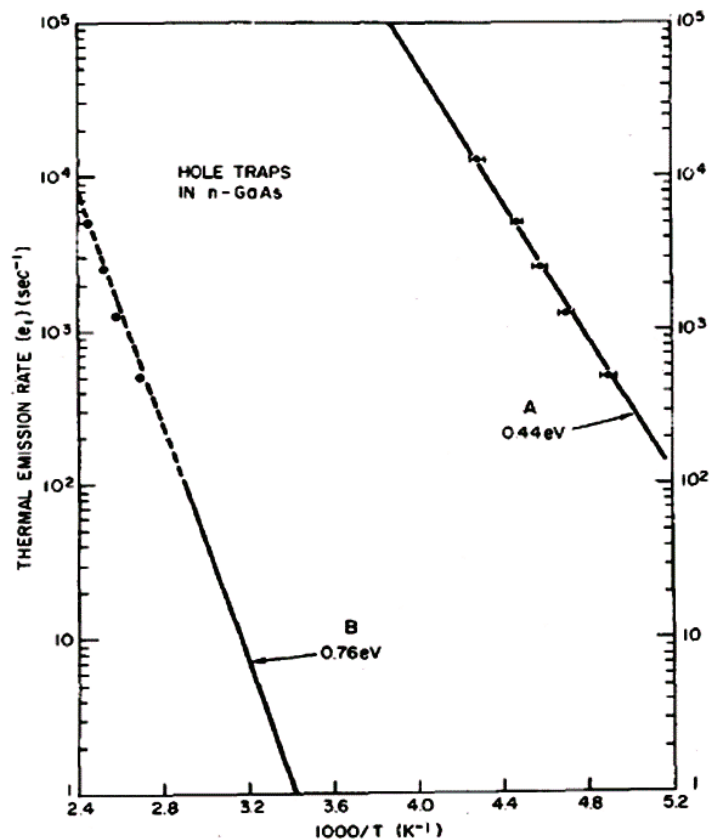


Figure 2-16: Arrhenius plot for traps detected in GaAs. (Thermal emission rate with respect to temperature) [34].

2.7 Experimental Set-up

A block diagram of a typical DLTS system is shown in Figure 2-17. A capacitance meter is used for obtaining the capacitance value. In order to get a higher sensitivity, capacitance meter is generally used in the differential mode with a fixed back-off capacitor [42]. The bias is usually applied through the “external voltage” facility on the instrument. Setting the proper filling pulse and reverse bias by employing a pulse generator and a DC voltage supply is significant for trap observation. During the filling pulse, traps get filled. Accordingly, the filling pulse duration (t_f) should be long enough to guarantee the trap filling. At the edge of the filling pulse, the recording of the capacitance transients is initiated while the voltage is returned to V_r . The period insures that the time during which the diode is reversed biased is long enough such that the capacitance transient reaches its steady-state value. The temperature is then changed, allowing the diode to stabilize, and the process is repeated [42].

The heart of the DLTS is the implementation of the rate window concept. The capacitance transient is fed to a “rate window” which provides maximum output when the trap time constant (τ) is equal to a known present time constant (t_{ref}). The transients are analyzed by the rate window system triggered from the pulse generator and the output signal is displayed on a recorder [42].

The diode is mounted in a variable temperature cryostat in intimate thermal contact with a temperature sensor which provides the signal for the x axis of the recorder [42].

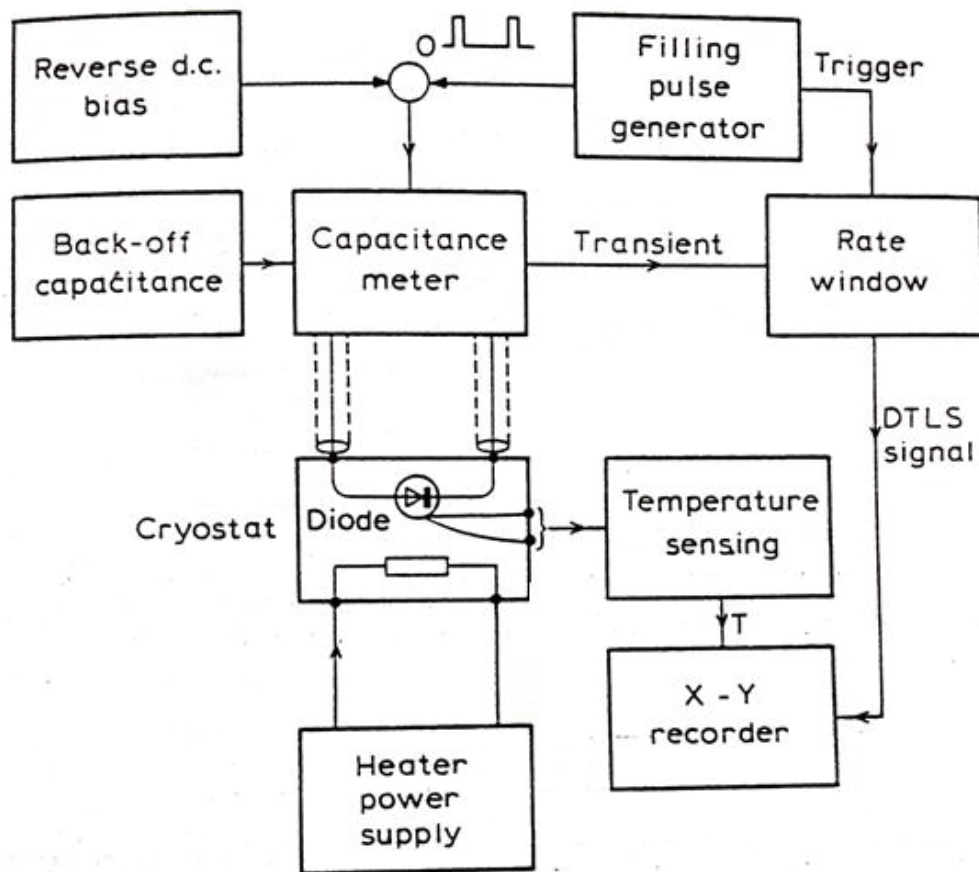


Figure 2-17: Block diagram of a DLTS system [36].

The experimental set-up used in the present work is a Sula DLTS system with temperature range of 10-500K. The experimental set-up is presented in Figure 2-18. The contents can be listed as;

- SULA Deep Level Transient Spectrometer
- Temperature controller
- vacuum chamber and sample holder;
- Computer and software.

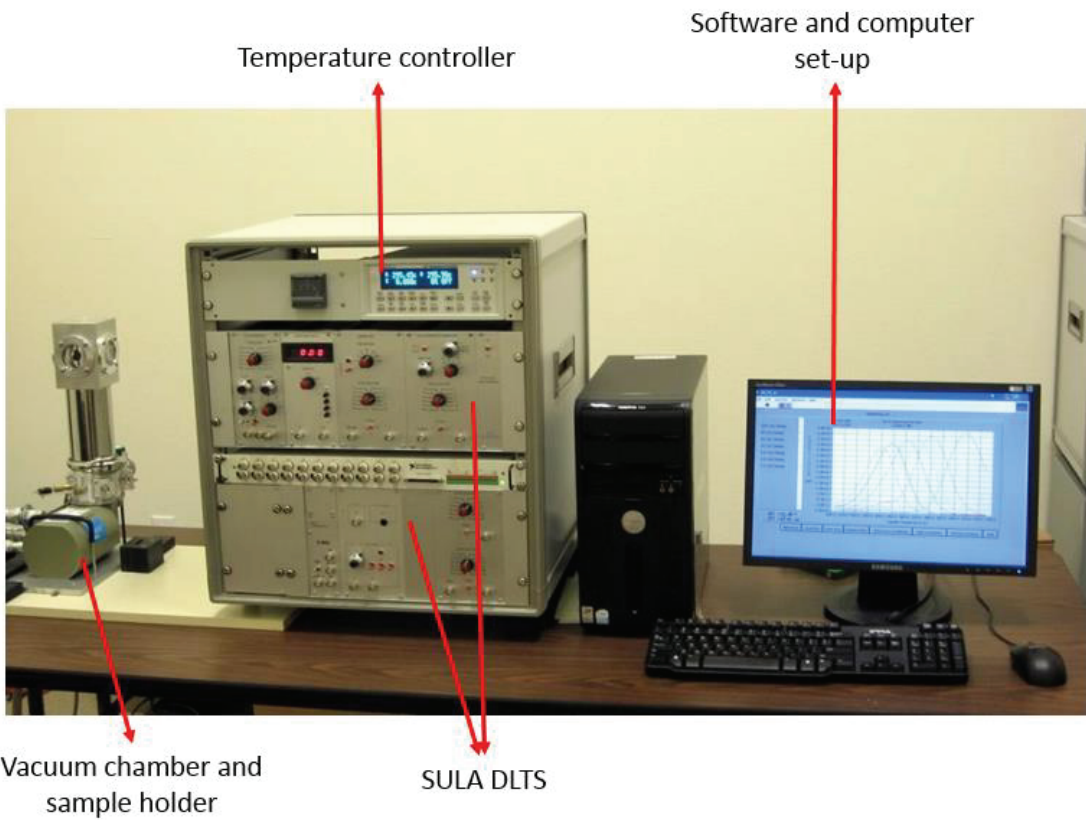


Figure 2-18: Set-up used for DLTS measurements [43].

2.7.1 SULA DLTS

The SULA DLTS have four modules: pulse generator module, capacitance module, correlator and pulse generator/correlator modules. The schematic for DULA DLTS is presented in Figure 2-19.

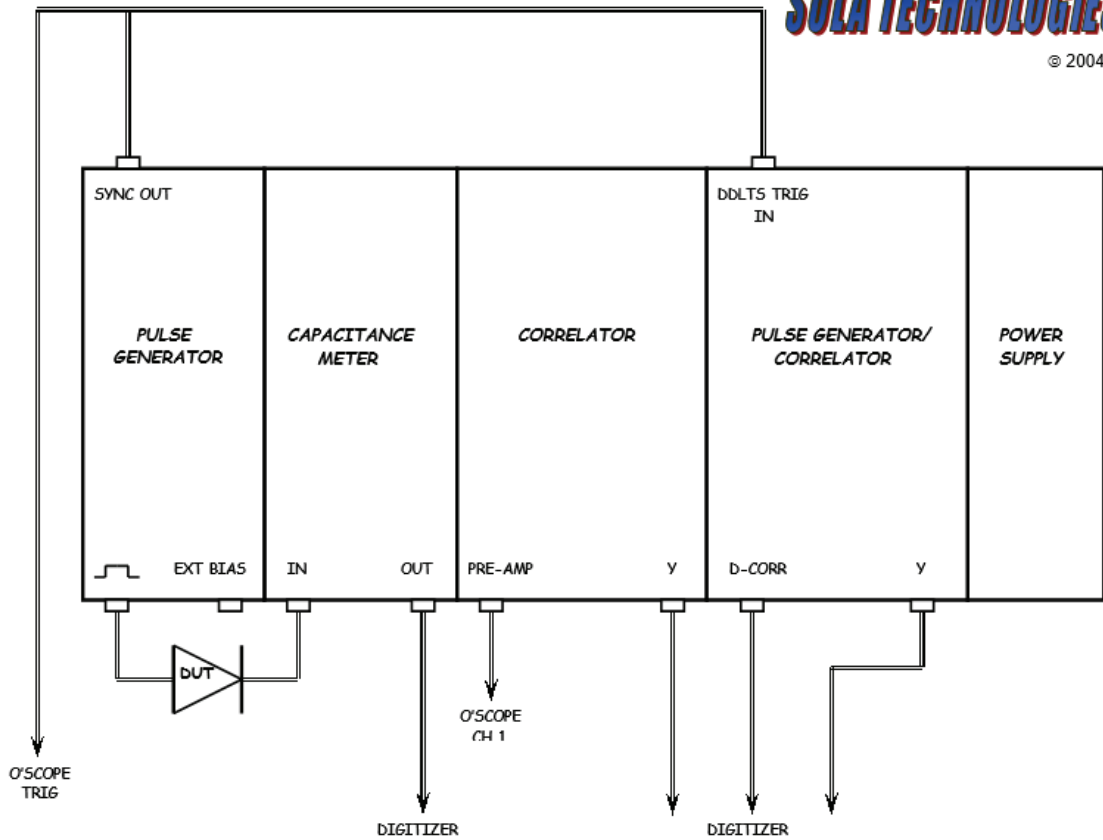


Figure 2-19: Schematic of SULA DLTS equipment [42].

2.7.1.1 Pulse Generator Module

The pulse generator module generates the desired sequence of voltages, by setting the value of the V_{bias} and $V_{amplitude}$.

V_{bias} corresponds to either (1) the DC reverse bias voltage in C-V measurements, or (2) the steady-state bias voltage in pulsed-bias experiments. It can be adjusted in the range of 0 V to -13 V.

V_{amp} corresponds to the bias pulse voltage. The amplitude of the pulse voltage can be arranged from 0V to 13V. It can be settled as negative or positive voltage with respect to the bias voltage. The period and width of the pulse voltage can be adjusted

as well. The pulse period can be adjusted between 50 μ uses and 1000msec. The actual pulse period can be 5-10% larger. The pulse width range covers 1 μ sec to 100 msec.

An external bias can be applied through pulse generator module. This function is useful for automatic C-V plotting (applying a voltage ramp to the sample), automatic deep level profiling and the computer-controlled bias pulsing. When not connected to a low-impedance voltage source, a 50 ohm plug should be connected to the EXT BIAS is terminal [42].

2.7.1.2 Capacitance Meter Module

The Capacitance module is used for monitoring the steady-state capacitance, value of V_{bias} and V_{amp} and leakage current. The leakage current is very important to be less than 150 μ A when doing simple C-V measurements or when the pulse is off, since at this value the capacitance meter undergoes overloading. However, during pulsing periods, the capacitance meter can tolerate large currents [42].

2.7.1.3 Correlator Module

The correlator module allows control and amplification of the capacitance transient. The signal-to-noise ratio is independent of this parameter. The rate windows can be set through this module. Twelve-position rotary switch is used for selecting the time delay between the end of the bias pulse and the onset of the correlation process. Delays can be settled from 0.02ms to 100ms. The rate windows selected with the correlator are accurate to about 2%. This represents a shift of less than 1K in the DLTS Arrhenius plot with essentially no change in slope [42].

2.7.2 Temperature Control

The experiment settings control defines that how the temperature is controlled during an experiment. The start up temperature is the set-point for the temperature process that will be used when Sula DLTS starts running. The maximum temperature limit is the highest set-point that the software will allow. The free run offset is used to preserve linear functionality in the free run experiment mode. In this mode, the software goes to an initial temperature, then changes the set-point to the final value,

plus the offset, and allows the system to record the temperature and correlator outputs continuously. The temperature value is shown in the temperature controller part of the set-up [42]. Figure 2-20 presents the sample holder and closed cycle cryostat for the set-up.



Figure 2-20: Closed cycle cryostat.

2.7.3 Software Setup

A computer system and a software setup is used for monitoring the measurement results. Different measurement such as C-V and C-T measurements, DLTS, DDLTS and MDDLTS measurements and their analysis can be performed and controlled by the defined software. The experiment conditions such as initial and final temperatures, voltage values and delays should be settled by the software.

In the next chapter, the application of the DLTS technique for the identification and characterization of traps in $\text{In}_x\text{Ga}_{1-x}\text{As}$ SWIR photodetectors will be presented.

CHAPTER 3

. Characterization of $In_xGa_{1-x}As$ SWIR Photodiodes

As discussed in the previous chapters, $In_xGa_{1-x}As$ is an important material for imaging sensor arrays operating in the SWIR band. The presence of carrier traps originating from impurities and/or defects in the material results in degradation of the photodetector characteristics by increasing the dark current and the noise of the detector. Therefore, identification of the electrical properties and possible origin of the traps in this material is important for increasing the signal to noise ratio of the imaging arrays by improving the material quality. In the scope of this thesis work, the properties of the traps in $In_xGa_{1-x}As$ are investigated and characterized in detail by the DLTS method. The results of this work are presented in this chapter.

3.1 Sample Description

The characterization work was conducted on p-n junction diodes with $In_xGa_{1-x}As$ absorber layer. The epilayer design, growth and the fabrication of these diode structures were implemented by the other members of the Quantum Devices and Nanophotonics Research Group of the Electrical and Electronics Engineering Department at METU. The epilayers of all the samples were grown by MBE on semi-insulating InP substrates by using Si and Be as the n and p-type dopants, respectively. The samples S1 and S2 were grown with an $In_{0.53}Ga_{0.47}As$ absorber layer, which is lattice matched to the InP substrate. While, the absorber layer of S1 is undoped (unintentionally doped), absorber of S2 is intentionally doped with Si. The absorber layer of samples S3 and S4 is undoped $In_{0.83}Ga_{0.17}As$ which is grown under lattice mismatched conditions. Sample S3 is a heterojunction photodiode with $In_{1-y}Al_yAs$ used as the graded buffer layer as well as n (contact) and p-layers of the

photodetector. Sample S4 is a homojunction photodiode with $\text{In}_x\text{Ga}_{1-x}\text{As}$ used as the graded buffer layer as well as n (contact) and p-layers of the detector. The epilayer structures of samples S3 and S4 are illustrated in Figure 3-1.

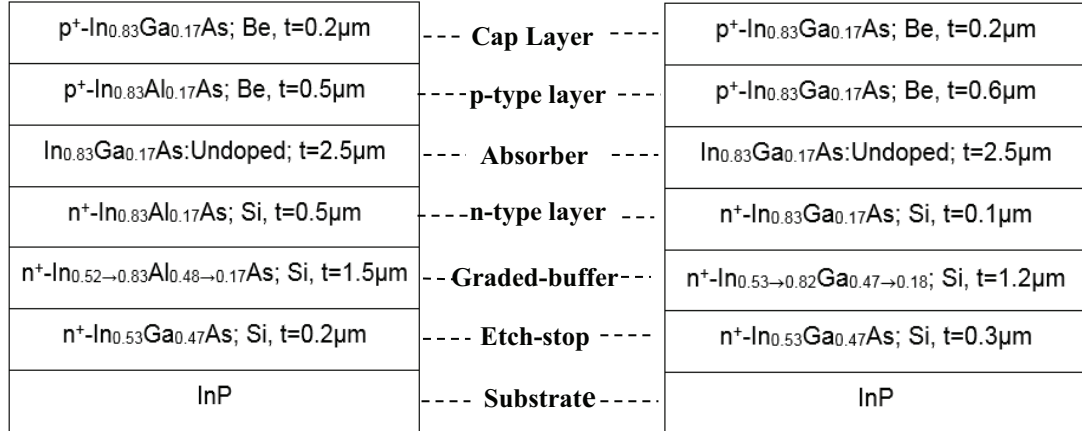


Figure 3-1: Structure details for lattice-mismatched $\text{In}_{0.83}\text{Ga}_{0.17}\text{As}$ SWIR photodiodes S3 and S4.

The detectors used for C-V and DLTS measurements were fabricated with a large area ($200 \times 200 \mu\text{m}^2$) in order to have a large enough capacitance. In order to avoid the surface artifacts which may originate from dry etching, the detector mesas were formed by wet etching.

3.2 C-V Characterization

The doping density can be deduced from the slope of the $1/C^2$ versus V_{bias} plot, and the built-in voltage can be obtained for $\frac{1}{C^2} \rightarrow 0$ as discussed in Chapter 2. The C-V measurement results are presented in this section.

The C-V measurement results for the lattice matched samples S1 and S2 show that the majority carrier density is about $3 \times 10^{15} \text{ cm}^{-3}$ and $8 \times 10^{16} \text{ cm}^{-3}$ for samples S1 and S2, respectively.

The measured majority carrier density for S3 and S4 are both $\sim 9 \times 10^{14} \text{ cm}^{-3}$ which is the unintentional doping density in the lattice mismatched $\text{In}_{0.83}\text{Ga}_{0.17}\text{As}$ absorber layer. Figure 3-2 and Figure 3-3 present the C-V measurement results for S3 and S4 indicating a built-in voltage of ~ 0.3 V for both samples which is in good agreement with the calculation using Equation 2-18. An important observation at this stage is that the lattice mismatched samples grown with different buffer layers ($\text{Al}_x\text{In}_{1-x}\text{As}$ in S3 and $\text{In}_x\text{Ga}_{1-x}\text{As}$ in S4) yield nearly the same unintentional doping density that is sufficiently low.

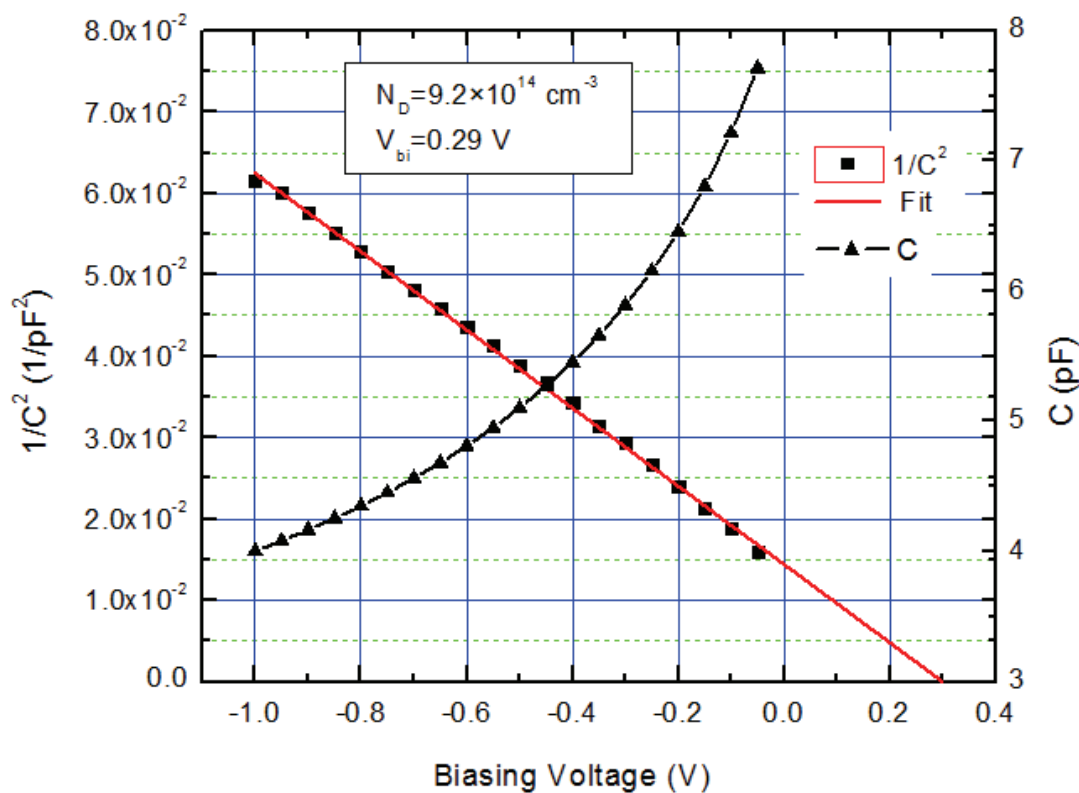


Figure 3-2: C-V characteristic for S3.

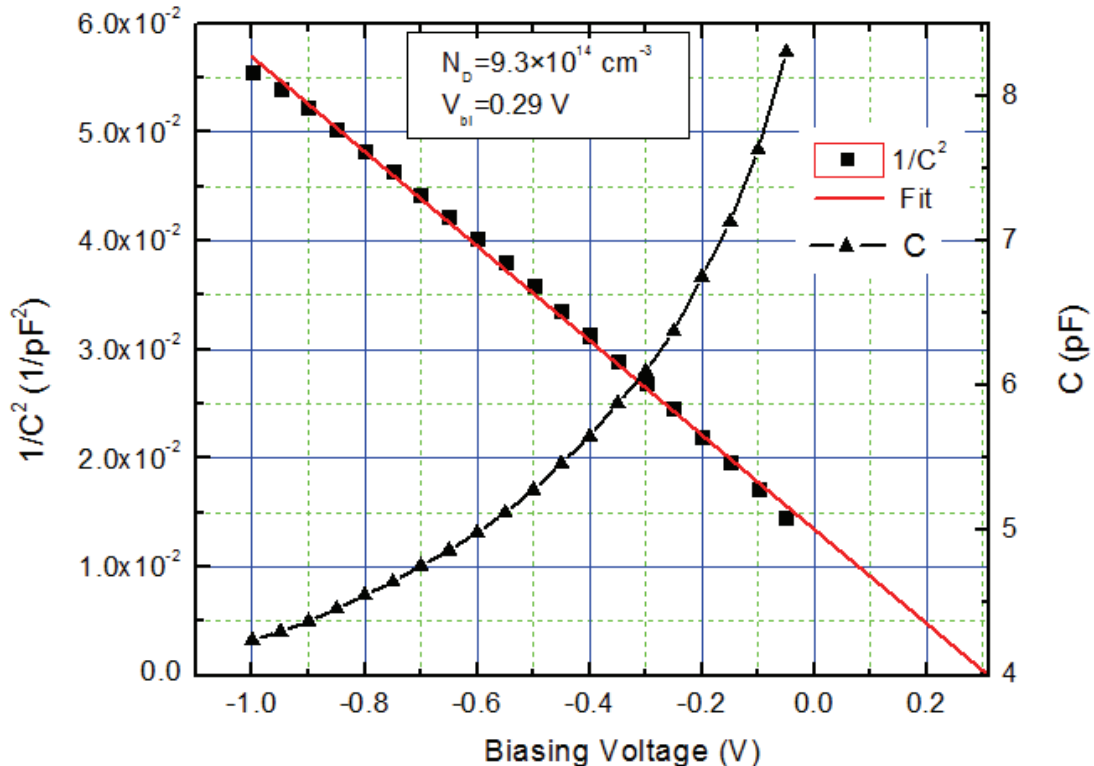


Figure 3-3: C-V characteristic for S4 (majority carrier concentration and built-in voltage are obtained from $1/C^2$ - V_{bias} plot).

3.3 DLTS Measurements

As discussed in Chapter 2, electrically active traps in the absorber layer of photovoltaic detectors may severely degrade the characteristics of the detector by increasing the g-r current. In order to identify the characteristics of the traps in the absorber layers of the samples, DLTS measurements were performed on the samples. A brief literature survey on the trap characteristics in $\text{In}_x\text{Ga}_{1-x}\text{As}$ is provided below before presenting the results of our DLTS measurements.

Deep centers located at around 0.35-0.40 eV above the valence band edge are reported for p^+ - $\text{In}_{0.53}\text{Ga}_{0.47}\text{As}$ [44-47]. These centers are generally related to the Fe impurities. Based on the measurements on $\text{In}_x\text{Ga}_{1-x}\text{As}$ grown on GaAs, it was proposed that small deviation from lattice-matched structures causes two new deep

centers with energy level at E_c -0.1 eV and E_c -0.48 eV on the dislocation or defect scenario[48].

Irvine *et al.* [49] studied MBE grown $In_xGa_{1-x}As$ with $0.045 \leq x \leq 0.18$ on GaAs substrate. They observed majority traps with activation energies of 0.795 eV, 0.763 eV and 0.621eV for $x=0.045$, 0.09 and 0.18. The results of the work are very close to the DLTS measurement results of the MOCVD grown $In_xGa_{1-x}As$ (on GaAs) with $0 \leq x \leq 0.13$ reported by Lang [50] and VPE grown $In_xGa_{1-x}As/GaAs$ studied by Mircea *et al.* [51] These deep levels were attributed to the interaction of the vacancies of GaAs and the dislocations due to the lattice-mismatch.

Trommer *et al.* [52] studied the LPE grown p-i-n diode consisting of an absorber layer of undoped $In_{0.53}Ga_{0.47}As$. The detailed analysis of the dark current for this sample identified a tunneling current through a deep level with the barrier energy of 0.16 ± 0.02 eV. On the other hand, a deep level acting as majority carrier trap with an activation energy of 0.57 ± 0.01 eV and a density of 2×10^{13} cm $^{-3}$ was detected by DLTS measurements.

Chen *et al.* [53] conducted a study on LPE grown Ti doped $In_{0.53}Ga_{0.17}As$ photodiodes. Two trap levels at $E_c-(0.27 \pm 0.02)$ eV and $E_c-(0.39 \pm 0.02)$ eV were observed. The first trap was observed in the undoped $In_{0.53}Ga_{0.17}As$ photodetector, as well. It was concluded that the trap with 0.27 eV activation energy was due to a native defect level, and the trap at $E_c-(0.39 \pm 0.02)$ eV was related to the Ti dopants. The deep level related with Ti had a capture cross section of 2.6×10^{-15} cm 2 and density of 2×10^{15} cm $^{-3}$.

Gfroerer *et al.* [54] reported a deep hole trap with the activation energy of 0.29 eV. The sample used in this work was based on MOCVD grown lattice matched $In_{0.53}Ga_{0.47}As/InP$. Silicon and Zinc were used as dopants for n- and p-type InGaAs. The reported trap density is about 2×10^{16} cm $^{-3}$ which seemed to be large when the quality of the material was considered. According to the high concentration of the traps around the p⁺-n junction, the observed trap was attributed to the Zn point defects.

Kowalczyk *et al.* [48] studied the deep centers in MBE grown $\text{In}_x\text{Ga}_{1-x}\text{As}/\text{InP}$ samples with $x=0.524$ and 0.534 . A majority carrier trap with the activation energy of 0.06 ± 0.03 eV below the conduction band edge, capture cross-section of 9×10^{-19} cm^{-2} and trap density of 5×10^{14} cm^{-3} was detected for MBE grown $\text{In}_{0.524}\text{Ga}_{0.476}\text{As}$ epilayer subjected to tensile strain. Two electron traps with the activation energies of $E_c-(0.1\pm0.02)$ eV and $E_c-(0.48\pm0.02)$ eV, and capture cross-sections of 6.7×10^{-18} cm^{-2} and 1.6×10^{-14} cm^{-2} were reported for $\text{In}_{0.534}\text{Ga}_{0.466}\text{As}$. The density of both traps were calculated to be about 2.5×10^{14} cm^{-3} . In this paper, traps were attributed to the lattice defects caused by the stress changes with the explanation that Fe concentration for undoped MBE grown InGaAs cannot be at the observed levels.

It can be concluded that somehow scattered results are reported in the literature on the characteristics of traps in the $\text{In}_x\text{Ga}_{1-x}\text{As}$ material. This should not be surprising since the characteristics of the traps depend on many factors including the growth conditions and the fabrication process. The main objective of this work is to establish the link between the observed trap characteristics and the performance limits of $\text{In}_x\text{Ga}_{1-x}\text{As}$ detectors which may also be applicable at some degree for the photodetectors fabricated with the other semiconductors.

3.4 DLTS Measurements on Lattice-matched $\text{In}_{0.53}\text{Ga}_{0.47}\text{As}/\text{InP}$ Photodetectors

With the objective of identifying the characteristics of the traps native to the MBE grown material, we present in this section, the traps observed in lattice matched (to InP) $\text{In}_{0.53}\text{Ga}_{0.47}\text{As}$ material through DLTS characterization of samples S1 and S2 which have unintentionally and intentionally doped absorbers, respectively.

The samples were mounted on the sample holder of the closed cycle He cryostat of the DLTS system and the temperature scans were implemented covering the temperature range 10-380 K. The following DLTS measurement conditions were used.

- V_{bias} : -2V, V_{amp} : 2.5V
- Filling pulse width: 1ms
- Pulse period: 20ms

- Delay times: 2ms, 1ms, 0.5ms, 0.2ms and 0.1ms

Table 3-1 summarizes the trap properties observed in samples S1 and S2.

Table 3-1: Summary of the traps detected in samples S1 and S2

Sample Name	Trap type	Activation energy	Trap density	Capture cross-section
S1	Electron trap	0.33 eV	$1.5 \times 10^{14} \text{ cm}^{-3}$	$4.74 \times 10^{-16} \text{ cm}^{-2}$
	Hole trap	0.11 eV	$8.06 \times 10^{13} \text{ cm}^{-3}$	$1.90 \times 10^{-17} \text{ cm}^{-2}$
S2	Electron trap	0.34 eV	$3.5 \times 10^{14} \text{ cm}^{-3}$	$3.24 \times 10^{-16} \text{ cm}^{-2}$
	Hole trap	0.11 eV	$1.74 \times 10^{13} \text{ cm}^{-3}$	$1.04 \times 10^{-17} \text{ cm}^{-2}$

According to the above results, a majority carrier trap located close to the midgap is detected in both samples. The results illustrate that the properties of the electron and hole traps observed for the undoped and doped $\text{In}_{0.53}\text{Ga}_{0.47}\text{As}$ are similar with the trap densities and capture cross sections in the same order. This observation suggests that Si doping does not have considerable effect on the trap characteristics of the material.

3.5 Trap Characterization of Lattice-mismatched $\text{In}_{0.83}\text{Ga}_{0.17}\text{As}$ Photodetectors

Some crystal defects such as dislocations and precipitates lead to the generation of the extended defects in materials grown under lattice-mismatched conditions. While the characteristics of the point defects are well defined, the electrical properties of the extended defects need detailed investigation. Extended defects in the semiconductors may yield deep-lying electronic states in the bandgap, significantly

affecting the charge-carrier density, mobility and the carrier lifetime. Furthermore, their actions as sinks or sources for intrinsic point defects and segregation centers for impurities have created significant detrimental effects in the device technology. Characterization of dislocation traps is possible by employing the DLTS measurements [55]. Before presenting the DLTS measurement results on the lattice mismatched samples, we provide below some background information on the anomalies observed in DLTS signal in the case of defect/dislocation related traps, as well as a brief literature survey.

3.5.1 DLTS Measurements on Defected Material

Point defects are typically known as isolated energy levels while one dimensional energy bands lying deep in the bandgap are attributed to the extended traps [55]. The main feature of the extended defects is their many electron manner with lots of energy states in the bandgap. Extended traps can be divided into two main groups based on their origins [55]:

- Bandlike states related to the atomic structure defects.
- Localized states related to their interaction with point defects

Unlike the point defects, the capacitance transient for extended defects is non-exponential. DLTS spectra for this kind of defects broaden due to the non-exponential capacitance transient. Omling et al. [56] introduced a model for analyzing the broadened DLTS spectra for the extended defects. This model introduces a Gaussian distribution into the capacitance transient as given below [56]

$$C(t) = C(0) \int_0^{\infty} G(E) \times \exp[-e_n(E)t] dE \quad (3-1)$$

where e_n is called the thermal emission rate and it is given by;

$$e_n = \sigma_n v_{th} N_c \times \exp\left(\frac{-\Delta E}{kT}\right) = A_{pf} \times \exp\left(\frac{-\Delta E}{kT}\right) \quad (3-2)$$

$G(E)$ in equation 3-1 is a normalized Gaussian function (centered at E_a). This function is given as [56-58]

$$G(E) = \frac{1}{S\sqrt{2\pi}} \exp\left[-\frac{(E - E_a)^2}{2S^2}\right] \quad (3-3)$$

where S is known as the standard deviation of the Gaussian distribution. Parameters of the obtained DLTS spectra can be deduced by fitting to the above-mentioned Gaussian curve. Accordingly, the parameters prefactor A_{pf} (and σ_n), the activation energy E_a and the $FPHW$ (full peak half width) of the Gaussian enthalpy distribution can be deduced. The $FPHW$ can be defined as [58];

$$FPHW = S\sqrt{2\ln 2} \quad (3-4)$$

The area under the DLTS peak fitted to a Gaussian curve for a well-defined activation energy is independent of the broadening factor S . Therefore, $\Delta T \cdot h(S)$ remains nearly constant where ΔT refers to the FPHW width and $h(S)$ is the peak height. Accordingly, the following relation can be written [56]

$$\Delta T_0 \cdot h(S = 0) = \Delta T \cdot h(S) \quad (3-5)$$

The ratio, $h(S = 0)/h(S)$ is known as the correction factor (κ) for deep level concentration. Omling et al [56] studied on a deep level electron trap in $\text{GaAs}_{1-x}\text{P}_x$. The above model was applied for the trap with strongly non-exponential capacitance transient. Figure 3-4 illustrates the influence of the broadening factor S on the DLTS spectra where E_a and A_{pf} are deduced by fitting to a Gaussian curve. They later studied on dislocation defects in plastically deformed silicon and showed that the model can be applied for dislocation defects as well [57].

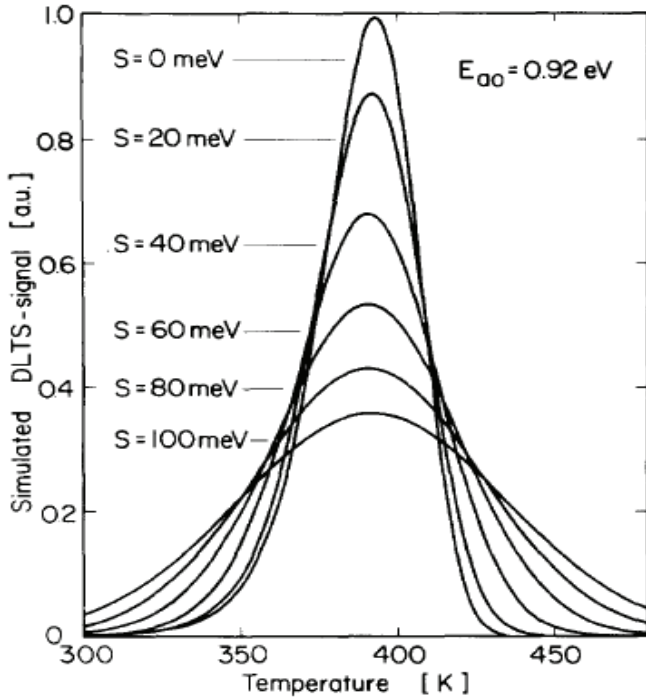


Figure 3-4: DLTS spectra for $\text{GaAs}_{0.74}\text{P}_{0.26}:\text{EL2}$ trap, illustrating the effect of S factor for a deep level trap with $E_a=0.92\text{eV}$ [56].

Cavalcoli *et al.* [58] also studied the dislocation defects in plastically deformed n-type silicon. Two dislocation related traps were identified by employing the model introduced by Omling *et al.* [56]. Figure 3-5 shows the theoretical fit for the experimentally obtained DLTS spectra for a dislocation trap.

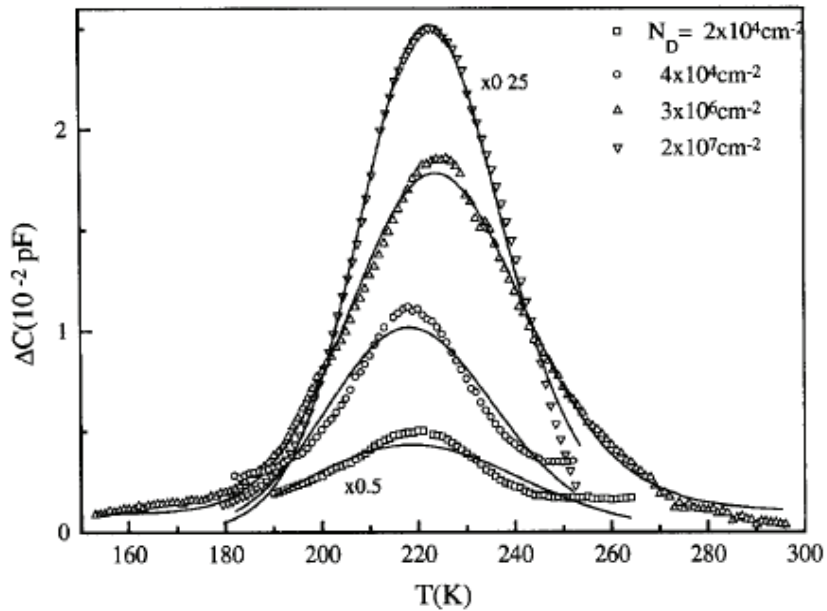


Figure 3-5: Theoretical fit to the experimental DLTS spectra for a dislocation defect in plastically deformed n-type Silicon with different dislocation densities [58].

The logarithmic dependence of the kinetics for the majority charge carriers captured in extended trap states is known as the logarithmic capture law, which is the distinct feature of the DLTS signal related to the extended defects [59]. In contrast to extended traps, point traps or impurities generally exhibit exponential capture kinetics, which is known as the exponential capture law [59]. In the point trap case, the DLTS peak amplitude saturates for large values of filling pulse widths. Considering the direct relationship between the DLTS peak amplitude and the defect concentration, saturation describes the situation when no more free charge carriers are captured in the defect states. Therefore, it determines the trap concentration N_T [59].

Generally, it can be concluded that the peak amplitude of isolated point defects exponentially depends on the logarithm of the filling pulse width. On the other hand, for extended defects, DLTS peak amplitude depends linearly on the $\log(t_p)$. This feature is typically used for distinguishing the extended and point defects [59].

Various studies on different semiconductors illustrate that the shape of the DLTS spectra is one of the different features of the dislocation defects. Broader peaks (symmetric or asymmetric) in the DLTS signal are typically observed for extended defects. However the peaks in the DLTS signal for point defects are generally narrow and symmetrical [59].

Separating the discrete and bandlike states is the other important issue in defect related trap studies, which is possible by surveying the temperature position of the DLTS peak points with respect to the filling pulse variations [59]. By increasing the filling pulse duration (t_p), DLTS peak amplitude increases for both. The behavior of the extended defect related DLTS signals for various filling pulse durations differs in two ways. For discrete defects i) the peak amplitude location remains at the same temperature and ii) the high temperature sides of the DLTS signals are proportional to filling pulse duration by $\Delta C\alpha \log(t_p)$ and coincide after signal normalization. On the contrary, for bandlike defects i) the DLTS peak points shift to the lower temperatures by increasing t_p and ii) the high temperature side of the DLTS signals coincides [59].

3.5.2 Literature Survey on DLTS Measurements on Lattice Mismatched InGaAs

Previous studies on different InGaAs based semiconductor materials reported extended defects due to the crystal defects. Watson *et al.* [60] studied the rectangular Schottky diodes with different lengths. $\text{In}_{0.06}\text{Ga}_{0.94}\text{As}$ was grown by MOVPE epitaxial growth technique on GaAs substrate. The work reported two types of majority traps. While the amplitude of the first trap remained same for diodes with different dimensions, the amplitude of the second trap increased for larger length values. The activation energy and capture cross sections for the first trap were reported as $0.49 \pm 0.02\text{eV}$ and $3 \times 10^{-14} \text{ cm}^2$. The activation energy for the second trap varied between $0.58 \pm 0.03\text{eV}$ and $0.73 \pm 0.02\text{eV}$ for different sample sizes, while the capture cross section varied in the range of $2 \times 10^{-16} \text{ cm}^2$ - $3 \times 10^{-16} \text{ cm}^2$. The linear dependence of the peak amplitudes on the logarithm of filling pulse duration identified dislocation related defects which are known as α - and β - dislocations [60].

Panepinto *et al.* [61] observed the same α - and β - dislocation originated traps for MOVPE grown $\text{In}_{0.14}\text{Ga}_{0.86}\text{As}/\text{GaAs}$ heterojunctions.

Pal *et al.* [62] studied MBE grown $\text{In}_x\text{Ga}_{1-x}\text{As}$ layers on GaAs substrate with x values of 0.10, 0.20 and 0.30. Three traps with activation energies about 0.15 eV, 0.30 eV and 0.50 eV were investigated. The logarithmic dependence of the last trap on the filling pulse duration and the fact that its concentration was higher for compressively strained sample (compared to the virtually unstrained sample) suggested that the trap was related to the dislocations [62].

Wosinski *et al.* [63] studied $\text{InGaAs}/\text{GaAs}$ p^+ -n heterojunction grown by LPE with very small mole fraction of Indium. The electron trap at $E_c - 0.68$ eV and density about 10^{15} cm^{-3} was attributed to electron states associated with dislocations in the GaAs epilayer surface.

Gelczuk *et al.* [64] reported deep level traps in MOVPE grown $\text{In}_{0.042}\text{Ga}_{0.958}\text{As}$ on GaAs substrate. Two out of the five detected electron traps with activation energies of 0.21 and 0.94 eV and capture cross-sections of $2.6 \times 10^{-19} \text{ cm}^2$ and $1.64 \times 10^{-12} \text{ cm}^2$ were classified as point defects. Third defect with activation energy of 0.79 eV and capture cross section of $3.19 \times 10^{-13} \text{ cm}^2$ was related to the E12 center in GaAs epilayer. The other two traps which had the activation energy values of 0.90 eV and 0.85 eV and capture cross sections of $2.77 \times 10^{-11} \text{ cm}^2$ and $1.4 \times 10^{-10} \text{ cm}^2$ were related to threading dislocations and misfit dislocations due to the linear increase in their DLTS peak amplitude with respect to the logarithm of the filling pulse duration.

Gelczuk *et al.* [57,63,64] later studied MOVPE grown $\text{In}_x\text{Ga}_{1-x}\text{As}$ layers on GaAs substrate with x values of 7.5%, 7.7% and 8.6%. Two deep electron traps were reported for each sample. Traps were related to the dislocation defects and their activation energies were reported as 0.5 eV and 0.7 eV. The other properties of the investigated traps were similar.

3.5.3 DLTS Measurement Results

The DLTS spectra obtained on sample S3 is presented in Figure 3-6. This sample is an heterojunction photodiode with $\text{In}_{1-y}\text{Al}_y\text{As}$ used as the graded buffer layer as well as n (contact) and p-layers of the photodetector. The DLTS spectra, Arrhenius plot and the characteristics of the first trap at ~ 100 K for five rate windows are provided in Figure 3-7. The trap has an activation energy of approximately 0.10 eV, density of $3.81 \times 10^{13} \text{ cm}^{-3}$ and capture cross-section of $8.48 \times 10^{-17} \text{ cm}^{-2}$.

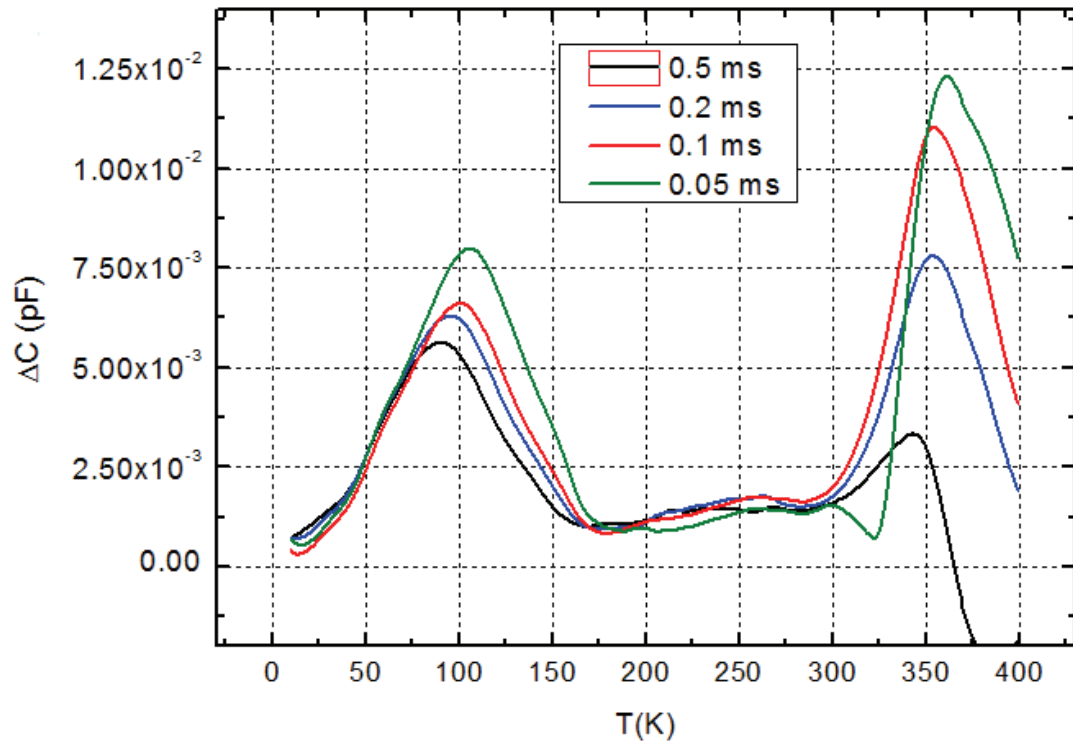


Figure 3-6: DLTS spectra for S3 (the plot illustrates two minority trap levels).

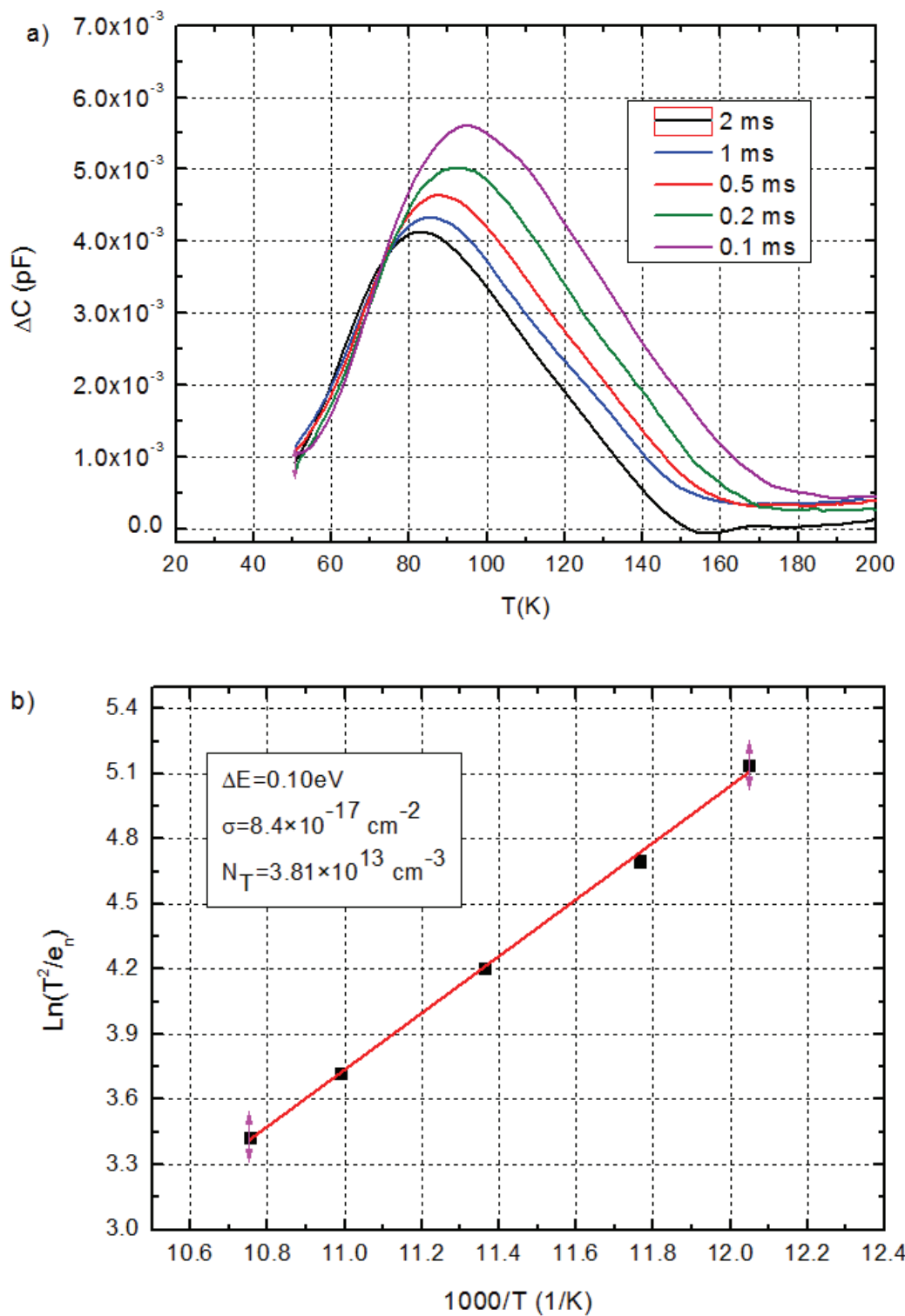


Figure 3-7: a) DLTS spectra for S3, b) Arrhenius plot and the properties of the observed minority carrier trap in sample S3.

The second trap yield peaks at higher temperatures where the dark current becomes relatively large. The DLTS measurement results for the second trap are shown in Figure 3-8. The asymmetric DLTS curves relate the second peak to the dislocation defects with a non-exponential capacitance transient. Therefore, the above-described model should be applied for determining the trap characteristics. Experimentally obtained DLTS peaks were fitted to a Gaussian curve. Figure 3-9 shows the fitting results with different broadening factor for each spectra. As the result of the fitting process, an activation energy of $E_a=0.31$ eV and a capture cross-section of 5.31×10^{-16} cm² were obtained.

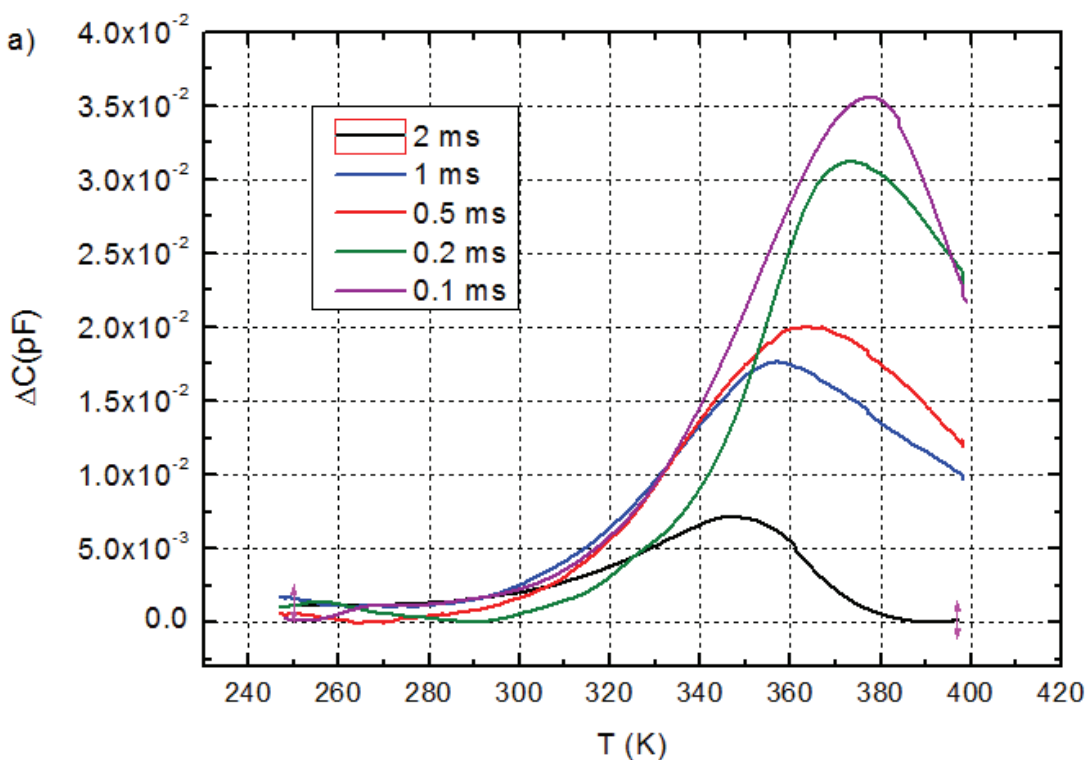


Figure 3-8: DLTS spectra for deep level trap due to dislocation defects.

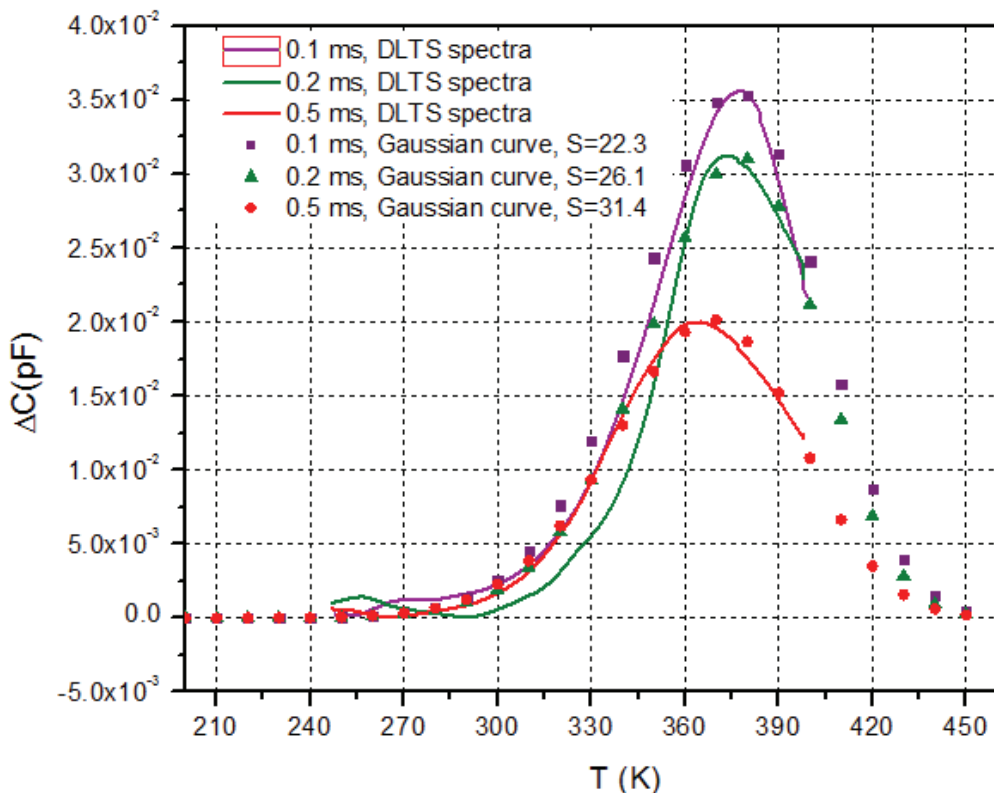


Figure 3-9: Theoretical fit to the experimentally obtained DLTS spectra. Broadening factor S is different for each spectra.

As mentioned before, due to the many electron behavior of the extended traps, the DLTS peak amplitude does not saturate even for large filling times. Peak height of the Gaussian curve for $S = 0$ has the maximum value that refers to the trap density. The correction factor for trap concentration (κ) can be deduced by calculating the ratio $h(S = 0)/h(S)$ where the activation energy and capture cross-section are defined by fitting procedure and S is found to be ~ 22 with a rate window of 0.1 ms. The ratio can be calculated as 5.2 by using this S value in order to obtain the corrected trap concentration. The traditionally calculated N_T by Equation 2-26 should be multiplied with the correction factor κ . Corrected trap concentration of $1.8 \times 10^{15} \text{ cm}^{-3}$ was obtained by employing this method.

Measurements were also performed on sample S4 which is a homojunction diode with $\text{In}_x\text{Ga}_{1-x}\text{As}$ p and graded buffer layers. The dark current of this sample is larger

than the sample S3 due to its homojunction structure. The higher dark current amount limits the temperature range of the DLTS measurement. It was not possible to set the DLTS measurements to the temperatures higher than 370 K due to the dark current limitation. As a result, clear detection and characterization of the second trap located at high temperatures was not possible. On the other hand, the DLTS signal of this trap is similar to that of the trap detected at high temperature in sample S3. The DLTS spectra for the peak located at the lower temperatures is provided in Figure 3-10. The Arrhenius plot shows that the activation energy for the trap is about 0.1 eV, capture cross-section is $8.5 \times 10^{-17} \text{ cm}^{-2}$ and trap density is $1.6 \times 10^{13} \text{ cm}^{-3}$. The results are similar to the characteristics of the first trap detected in S3. These results suggest that the origin of this trap in epilayers grown with different buffer layers are related to the same point defect.

Table 3-2 summarizes the detected minority carrier traps and their properties for S3 and S4. There was not any majority trap detected under reverse bias application (without filling pulse).

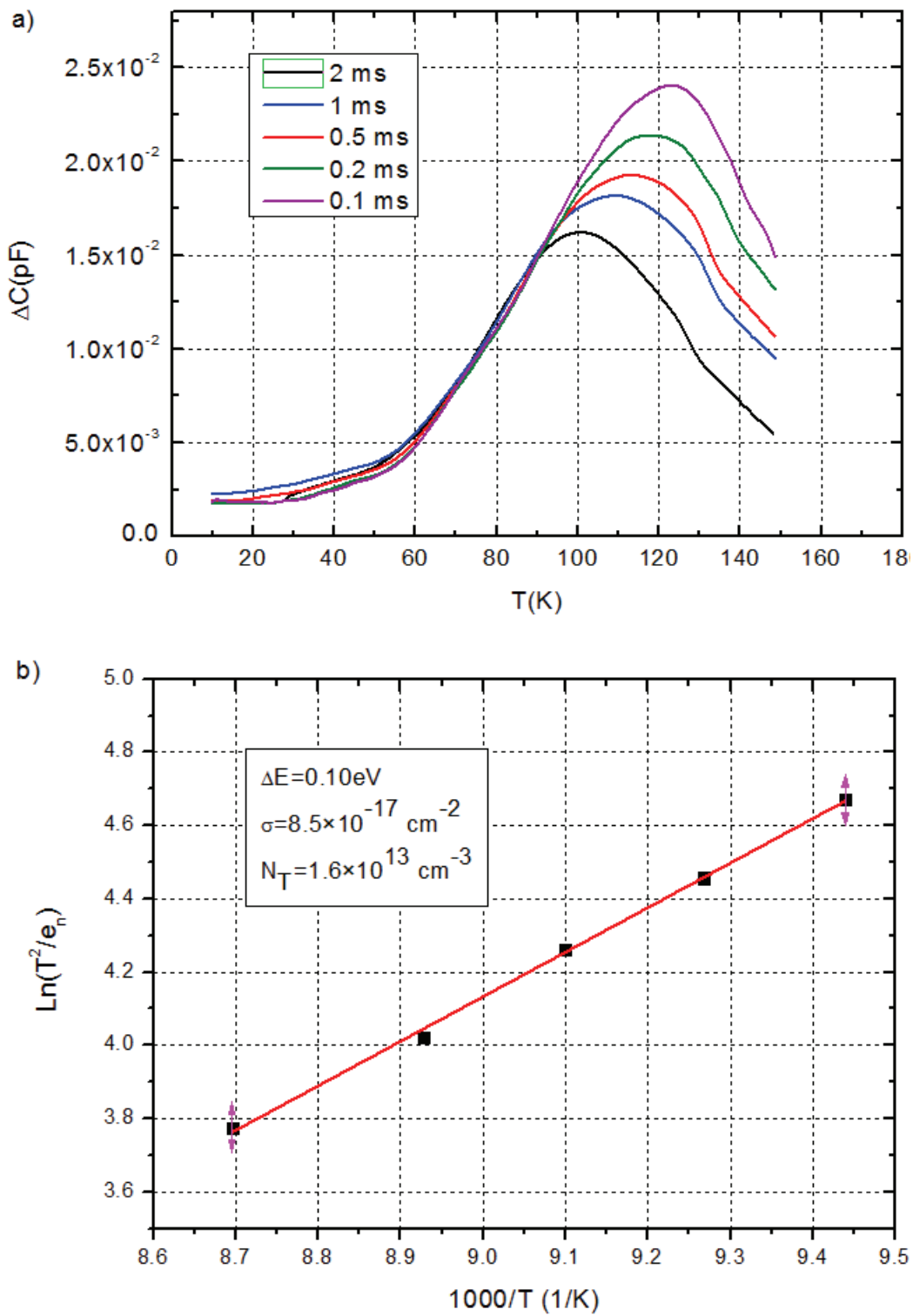


Figure 3-10: a) DLTS spectra for S4, b) Arrhenius plot and the properties of the observed minority carrier trap in sample S4.

Table 3-2: Summary of the traps detected in samples S3 and S4.

Sample Name	Trap type	Activation energy	Trap density	Capture cross-section
S3	1. Hole trap	0.10 eV	$3.81 \times 10^{13} \text{ cm}^{-3}$	$8.4 \times 10^{-17} \text{ cm}^2$
	2. Hole trap	0.31 eV	$1.8 \times 10^{15} \text{ cm}^{-3}$	$5.31 \times 10^{-16} \text{ cm}^2$
S4	1. Hole trap	0.10 eV	$1.6 \times 10^{13} \text{ cm}^{-3}$	$8.5 \times 10^{-17} \text{ cm}^2$

In order to determine the type of the detected traps, measurements were repeated for different filling pulse widths under the same bias voltage, period and time delay. The amplitude of the peak points of the DLTS spectra for different filling pulse widths from 1 μs to 5 ms are provided in Figure 3-10. This figure illustrates that the peak amplitude of the DLTS spectra for the trap with activation energy of 0.1eV observed in sample S3 increases with respect to the logarithm of the filling pulse width ($\log(t_f)$) up to 0.5 ms. Then, it saturates under larger filling pulse durations showing that the trap becomes fully occupied after a certain filling pulse duration. This observation indicates that the trap is an isolated point defect.

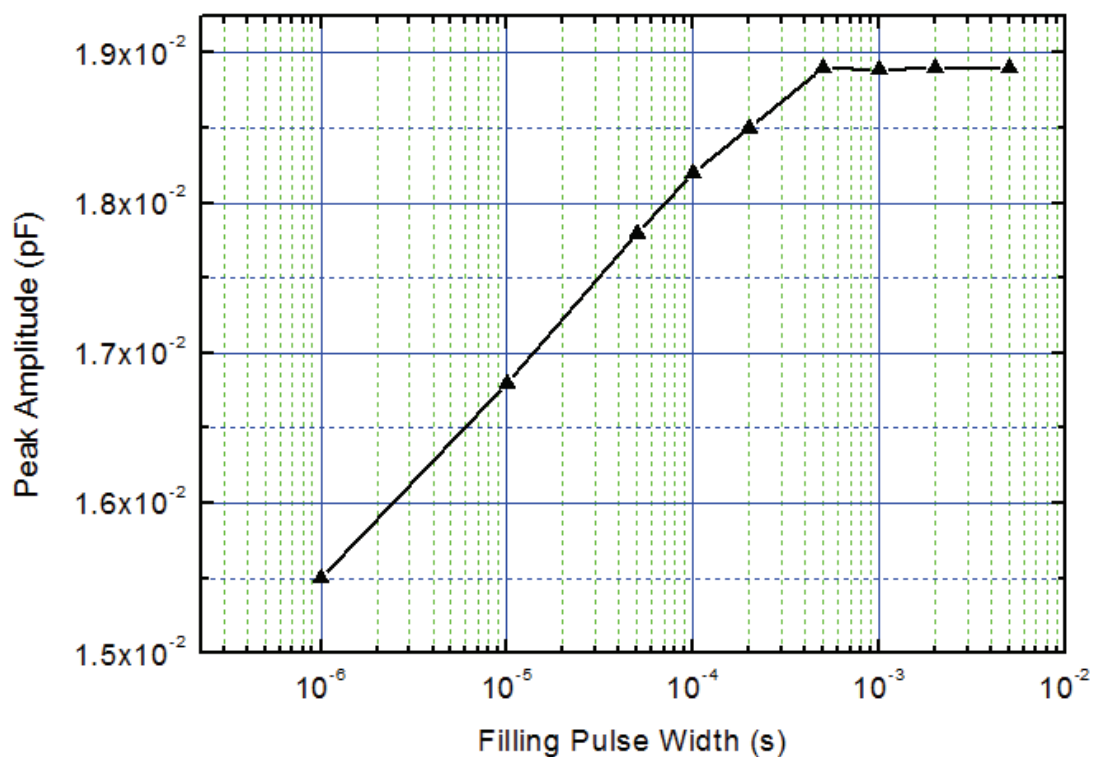


Figure 3-11: Amplitude of the DLTS peak point for the first hole trap in S3 versus filling pulse width.

Figure 3-12 illustrates the changes in the DLTS peak amplitude of the second minority carrier trap with activation energy of 0.31 eV observed in sample S3 with respect to the filling pulse duration. The plot exhibits nearly linear dependence of the DLTS signal peak amplitude on the logarithm of the filling pulse width and the peak amplitude does not saturate. As a result, the observed trap is related to the dislocations due to the lattice-mismatch in the epilayer structure.

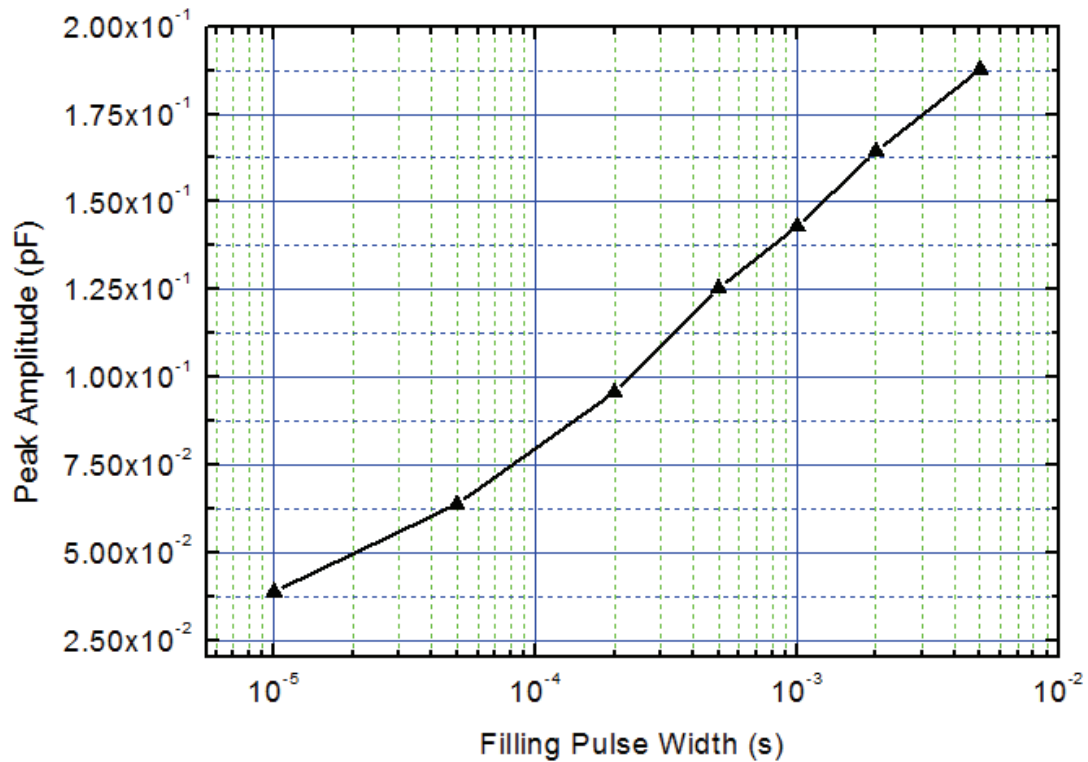


Figure 3-12: Amplitude of the DLTS peak points for the second hole trap in S3 versus filling pulse width.

Figure 3-13 shows the change in the temperature values related to the DLTS peak points with respect to the filling pulse duration. The plot exhibits that the DLTS spectra peak shifts toward lower temperatures by increasing the filling pulse duration. This shift is an indication that the observed extended trap is related with band-like dislocation defects.

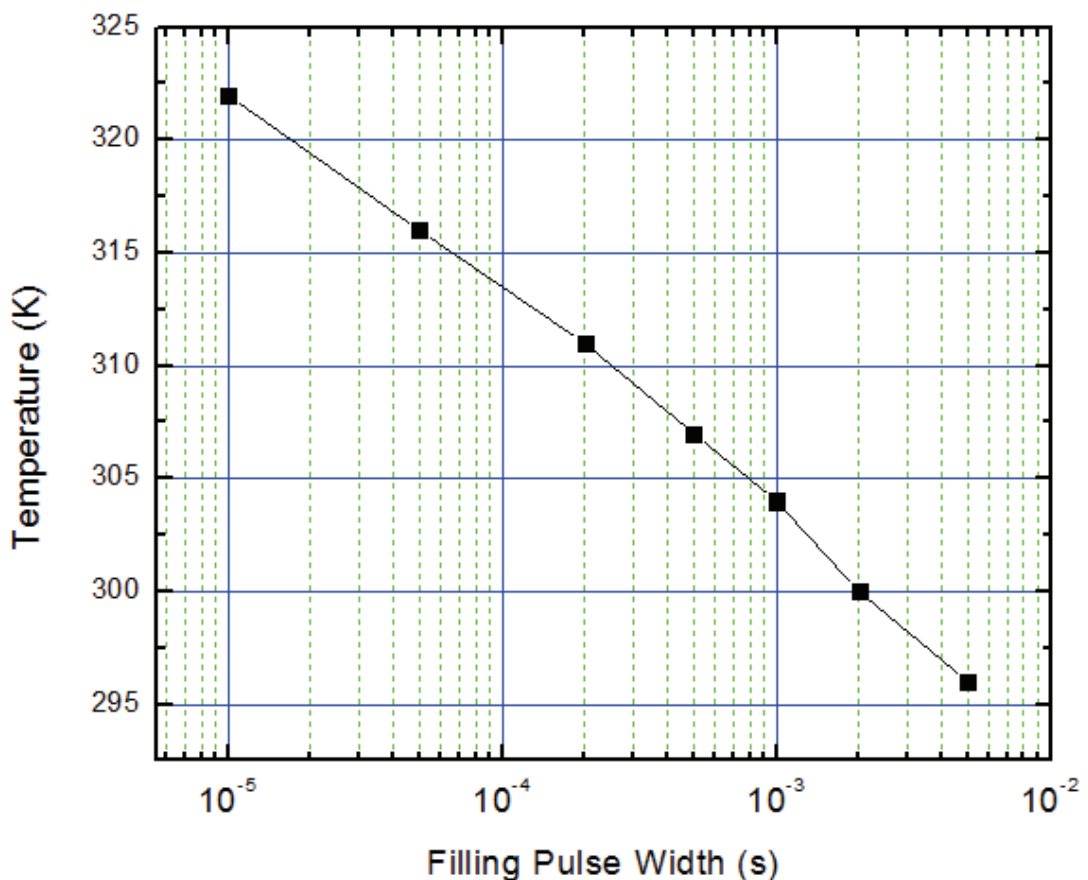


Figure 3-13: Temperature point of DLTS spectra peaks versus filling pulse width.

The above work can be summarized as follows. The traps in lattice matched $\text{In}_{0.53}\text{Ga}_{0.47}\text{As}/\text{InP}$ (samples S1 and S2) and lattice mismatched $\text{In}_{0.83}\text{Ga}_{0.17}\text{As}/\text{InP}$ (samples S3 and S4) were investigated by DLTS measurement. While one majority and one minority carrier point trap were detected for S1 and S2, two minority carrier traps were observed in S3 and S4. The minority carrier traps in the lattice mismatched $\text{In}_{0.83}\text{Ga}_{0.17}\text{As}$ photodetectors were distinguished as a point and an extended trap. Finally, the extended trap was classified as band-like dislocation defect. In the next part, results of the I-V characterization and dark current modeling on sample S3 are related to the DLTS measurement results obtained in this part.

3.6 I-V Characterization and Results

The I-V characterization of sample S3 was performed on small dimension test detectors fabricated with this material. Indeed, the test detectors with an area of approximately $20 \times 20 \mu\text{m}^2$ are identical to the pixels of an FPA which was fabricated by the other members of the Quantum Devices and Nanophotonics Research Group [32]. The test detector array was flip chip bonded to a fan out substrate and the detectors were connected in shunt for more reliable electrical characterization.

The dark current measurements were done on the lattice-mismatched $\text{In}_{0.83}\text{Ga}_{0.17}\text{As}$ heterojunction p-i-n photodiode (sample S3) by the other members of the research group at the Quantum Devices and Nanophotonics Research Laboratory using the pixels of a large format imaging sensor array fabricated with epilayer structure S3 [32]. The pixel pitch of the imaging sensor was $25 \mu\text{m}$ with pixel dimensions of approximately $20 \times 20 \mu\text{m}^2$. The work reported that the bulk generated dark current is the dominant component of the dark current by performing current measurements on test detectors with different areas. The obtained dark current activation energy illustrates that there is not considerable tunneling component above 200 K up to a reverse bias voltage of 3V which can be related to the low doping density in the absorber layer. The I-V characteristics (under dark) of a single test detector pixel ($\sim 20 \times 20 \mu\text{m}^2$) are shown in Figure 3-14 in the temperature range 140-300 K. As shown in the following sections, the bulk dark current components of the detectors under reverse bias are generation-recombination current (I_{gr}), diffusion current (I_{diff}) and shunt current (I_{sh}). For certain operating circumstances such as specific voltage and temperature, the dominancy of these components changes. To determine the dominant component mechanism of the dark current, a model is established by considering their descriptions. By using curve-fitting method, the model fits to the empirical results leading to the identification of the dominant dark current mechanisms.

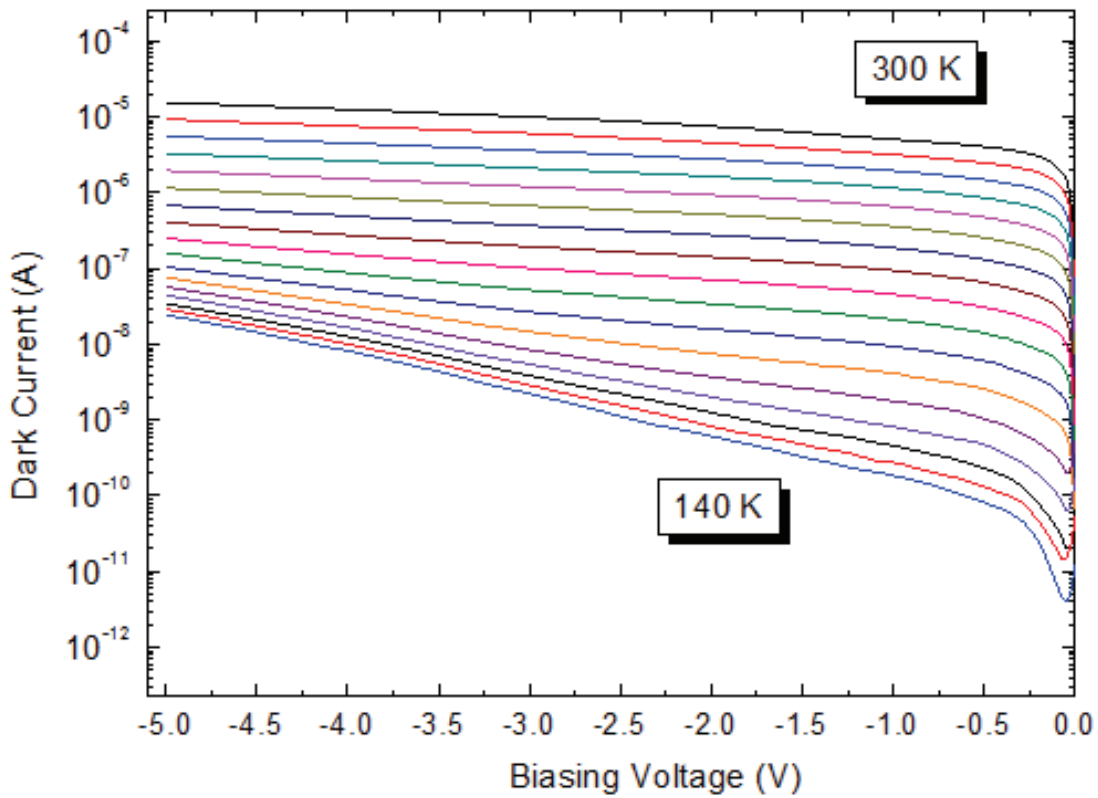


Figure 3-14: The IV-T characterization for S3.

The overall dark current equation can be written as;

$$I_{dark} = I_{diff} + I_{gr} + I_{sh} + I_{surface} \quad (3-6)$$

The diffusion current generates due to the diffusion of the thermally generated minority carriers toward the depletion region. It is highly temperature dependent mechanism and will be large for high temperatures. The diffusion current can be expressed as

$$I_{diff} = I_s \left(\exp \left(\frac{qV}{kT} \right) - 1 \right) \quad (3-7)$$

where I_s is named as the saturation current given by

$$I_s = n_i^2 A (qk_b T)^{1/2} \left[\frac{1}{n_n} \left(\frac{\mu_p}{\tau_p} \right)^{\frac{1}{2}} + \frac{1}{p_p} \left(\frac{\mu_n}{\tau_n} \right)^{\frac{1}{2}} \right]^{-1} \quad (3-8)$$

In the above expression, μ_n and μ_p are mobilities for electron and hole. τ_n and τ_p are recombination lifetime of electrons and holes in the p and n sides of the junction. n_i is the intrinsic carrier concentration which is defined by [11]

$$n_i = 2 \left(\frac{4\pi^2 m_e m_h k^2}{h^4} \right)^{3/4} T^{3/2} \exp \left(- \frac{E_g}{2k_b T} \right) \quad (3-9)$$

where h is the planck's constant and m_e and m_h are effective masses of electrons and holes. The temperature dependence of the diffusion current is obvious from Equation 3-9.

The generation-recombination of the EHPs in the depletion region leads to the G-R current. G-R current can be expressed as

$$I_{g-r} = \left(\frac{qn_i AW}{\tau_{eff}} \right) \left(\exp \left(\frac{qV}{2k_b T} \right) - 1 \right) \quad (3-10)$$

where τ_{eff} is effective lifetime. The depletion region width can be expressed as

$$W = \left\{ \frac{2\varepsilon_s}{q} \left(\frac{1}{N_A} + \frac{1}{N_D} \right) (V_{bi} + V) \right\}^{1/2} \quad (3-11)$$

where V_{bi} can be calculated by

$$V_{bi} = \frac{k_b T}{q} \ln \left(\frac{N_D N_A}{n_i^2} \right) \quad (3-12)$$

The surface G-R current is generated by the surface conditions. It is proportional to the surface recombination velocity. This current can be expressed by [38]

$$I_{sg-r} \propto \sqrt{V_{bi} + V} \exp\left(-\frac{E_g}{2k_b T}\right) \quad (3-13)$$

The final component dominant in our diodes is the ohmic leakage or shunt current. This current is mainly generated due to the dislocations and defects in the epilayers. It can be defined as

$$I_{shunt} = \frac{v}{R_{sh}} \quad (3-14)$$

where R_{sh} is the shunt resistance of the diode, and v is the applied bias voltage.

Under reverse bias, I_{diff} can be considered to be equal to I_s . Therefore, by taking the ratio of I_{diff} and I_{gr} under reverse bias, the following expression can be deduced [68]

$$\frac{I_{g-r}}{I_{diff}} = \frac{Wn\tau_p}{L_p n_i \tau_{eff}} \quad (3-15)$$

By Considering that, L_p , τ_p and τ_{eff} are not strongly temperature dependent parameters, the dependence of the above ratio on temperature can be written as [69].

$$\frac{I_{g-r}}{I_{diff}} \propto \frac{1}{n_i} \propto \exp\left(\frac{E_g}{2kT}\right) \quad (3-16)$$

Equation 3-16 illustrates that; the G-R current will be more dominant at low temperatures since the diffusion current decreases faster when the detector is cooled.

The dark current modeling of the test detectors fabricated with sample S3 was performed by the other members of the Quantum Devices and Nanophotonics Research Group [32]. The results of this modeling for two different operating temperatures are shown in Figure 3-15.

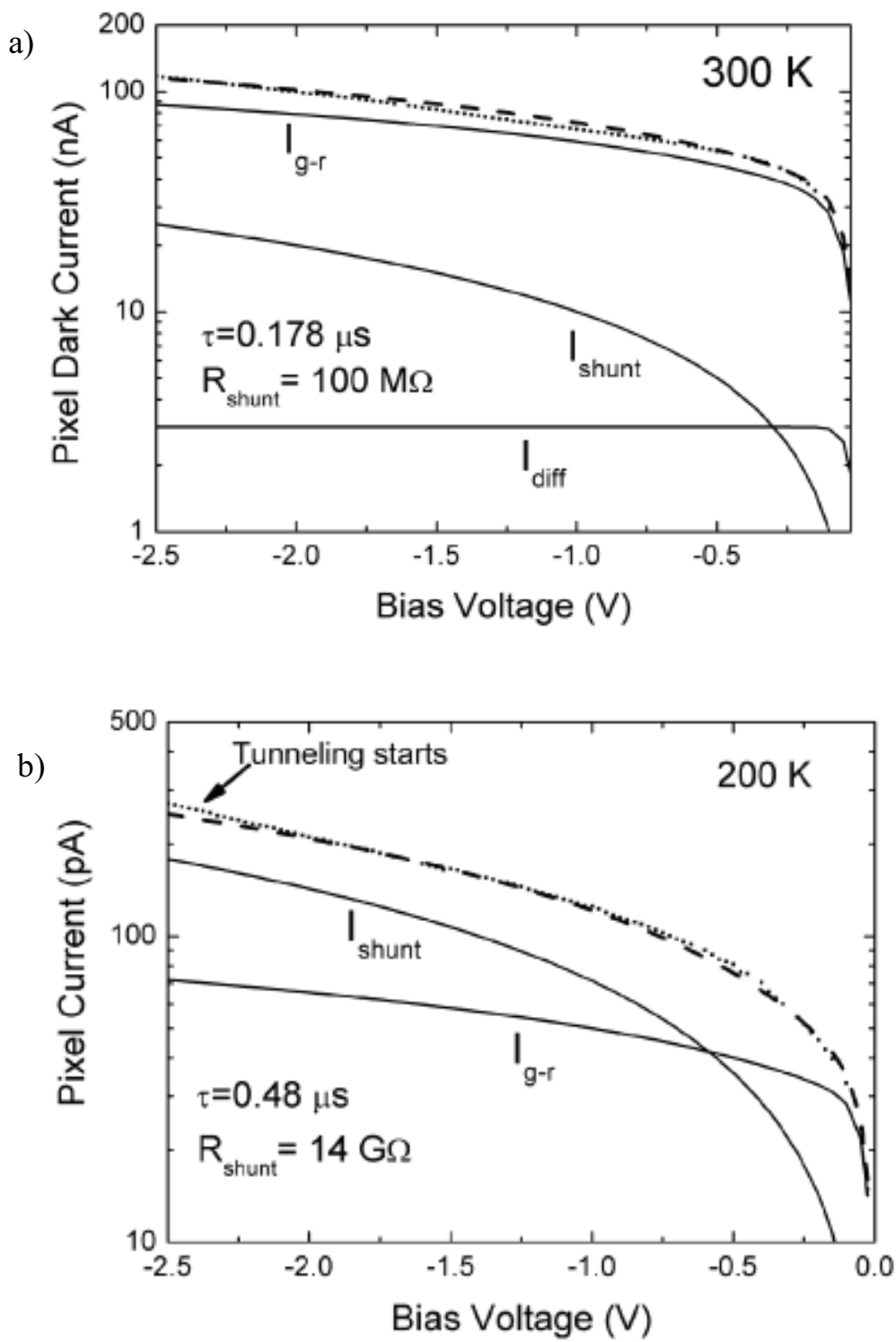


Figure 3-15: Distinguishing the dark current components by dark current modeling
a) at the operation temperature of 300K. b) at the operation temperature of 200K [32].

The dark current activation energy obtained in the work [32] was considerably below E_g/kT indicating that the diffusion component of the dark current was not the dominant component below room temperature. Activation energy obtained from R_0A variations versus the temperature was close to $E_g/2$ indicating that the dominant dark current mechanism was the G-R mechanism near zero bias.

The plot of the effective G-R lifetime versus temperature is presented in Figure 3-16 [32].

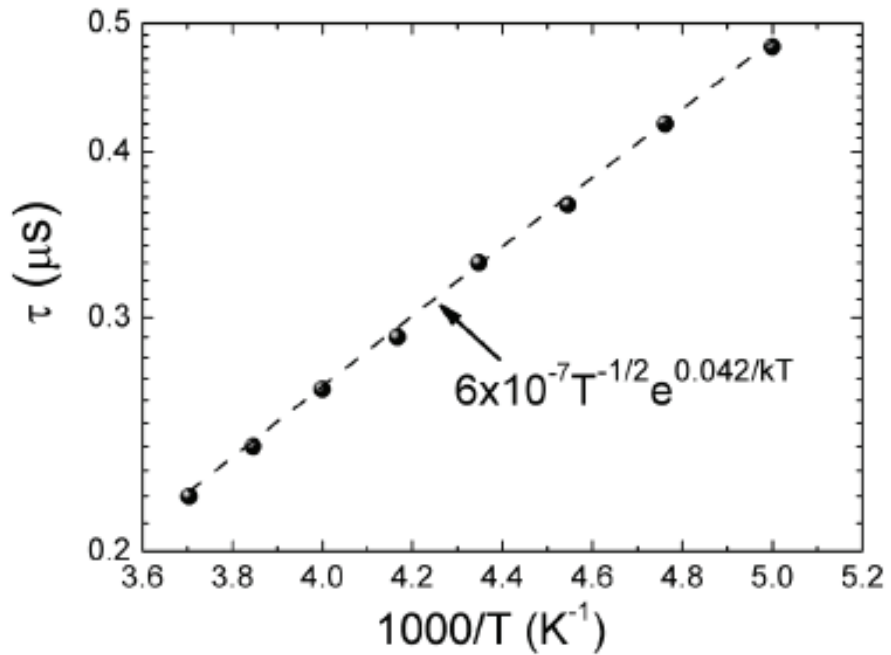


Figure 3-16: Variation of the G-R lifetime with respect to the temperature [32].

The effective G-R lifetime (τ) expression contains both electron and hole lifetimes (τ_n and τ_p). In presence of a dominant trap level, τ can be deduced as [32]

$$\tau = \frac{1}{\sigma_t \nu_{th} N_T} e^{E_T - E_i / kT} \quad (3-17)$$

The activation energy of 42 meV in Figure 3-16 illustrates a trap located at energy level of 0.042 eV with respect to the E_i .

Looking back at the DLTS measurement results, two minority traps with activation energy of 0.1 eV and 0.31 eV were detected in sample S3. The second trap, which was an extended trap with larger capture cross section and density was located at $E_i+0.06\text{eV}$ at ~ 300 K. In conclusion, the energy level of the trap detected by the DLTS measurements is close to the trap level extracted from I-V characterization. The point trap with activation energy of 0.1eV was detected in both lattice-matched and lattice-mismatched samples with similar densities and capture cross sections. We believe that this trap contributes to dark current equally in the lattice matched and lattice mismatched samples. Therefore, considerably larger dark current in the lattice-mismatched samples can be attributed to the extended trap observed only in the lattice-mismatched samples. The agreement in the trap characteristics obtained through dark current modeling and DLTS measurements supports this proposal.

By inserting the properties of the extended trap detected by the DLTS measurements into Equation 3-17, the G-R lifetime of the trap is found as $0.125\ \mu\text{s}$ at ~ 370 K. According the dark current modeling, the G-R lifetime at the same temperature can be obtained as $0.116\ \mu\text{s}$ [32]. This good agreement also supports the solidity of the approach proposed by Omling *et al.* [56].

CHAPTER 4

CONCLUSION AND FUTURE WORK

Comprehensive study of deep levels in MBE grown lattice-matched $\text{In}_{0.53}\text{Ga}_{0.47}\text{As}$ and lattice-mismatched $\text{In}_{0.83}\text{Ga}_{0.17}\text{As}$ SWIR photodetectors has been undertaken in the present work. Deep level traps were identified and characterized by employing the DLTS method. Two homojunction lattice-matched $\text{In}_{0.53}\text{Ga}_{0.47}\text{As}$ SWIR photodetectors, one with undoped $\text{In}_{0.53}\text{Ga}_{0.47}\text{As}$ absorber layer and the other with Si doped $\text{In}_{0.53}\text{Ga}_{0.47}\text{As}$ absorber layer were studied. One electron trap at $E_c - 0.33$ eV and one hole trap at $E_v + 0.15$ eV were detected in the lattice-matched $\text{In}_{0.53}\text{Ga}_{0.47}\text{As}/\text{InP}$ p-i-n photodiodes with different absorber doping densities. The results show that Si doping density of the absorber layer does not affect the trap properties in the semiconductor. The other samples under investigation were a heterojunction and a homojunction lattice-mismatched $\text{In}_{0.83}\text{Ga}_{0.17}\text{As}$ extended SWIR photodetector with InAlAs and InGaAs buffer layers, respectively. Two hole traps were detected in both of the samples. The sample with the AlInAs buffer layer yielded hole traps with energy levels of $E_v + 0.10$ eV and $E_v + 0.31$ eV. Based on the relationship between the peak amplitude of the DLTS spectra and the filling pulse width, the types of the traps were distinguished. While the trap detected at lower temperature seems to be due to a point defect, the second trap is related to the extended defects due to the lattice-mismatch between the layers, and this trap seems to be responsible for the degradation in the detector characteristics due to the lattice mismatch. The activation energy, density and the capture cross section of this trap were found to be 0.31 eV, $1.8 \times 10^{15} \text{ cm}^{-3}$ and $5.31 \times 10^{-16} \text{ cm}^2$, respectively. The DLTS

measurement results for the extended trap were in a good agreement with the trap properties obtained by the dark current analysis.

Due to the large dark current, trap detection was not possible for the extended wavelength SWIR photodetector with InGaAs buffer layer. Once this problem is overcome, the same dark current and DLTS spectra analysis can be performed on the detector in order to find out the difference between the trap characteristics in the samples with different buffer layers as further work.

REFERENCES

- [1] <https://9-4fordham.wikispaces.com/> [Last accessed on. 10.05.2016]
- [2] A. K. Sreedhar, K. S. R. Koteswara Rao, “Infrared Detectors Materials and Technology”, Defence Research & Development Organisation, New Delhi, pp. 110-111, 2006.
- [3] C. Beşikci, “Infrared Devices and Systems Lecture Notes”, Ankara: METU, 2012.
- [4] Y. Arslan, “High Performance Focal Plane Array Technologies from Short to Long Wavelength Infrared Bands”, MSc Thesis, Middle East Technical University, Turkey, Sep. 2014.
- [5] A. Rogalski, “Infrared Detectors: an Overview”, *Infrared Physics & Technology*, vol. 43, pp. 187-210, 2002.
- [6] M. Razeghi, “Current Status and Future Trends of Infrared Detectors”, *Optoelectronics Review*, no. 3, pp. 155-194, 1998.
- [7] R. Hudson, “Infrared System Engineering”, New York: Wiley, 1969.
- [8] www.octsensors.com [Last accessed on. 10.05.2016]
- [9] www.lrc.rpi.edu/programs/nlpip/lightingAnswers/photovoltaic/04-photovoltaic-panels-work.asp [Last accessed on. 10.05.2016]
- [10] L. Esaki, “Long Journey into Tunnelling”, *Proceeding of the IEEE*, vol. 62, no. 6, pp. 825-831, 1974.
- [11] O. Temel, “Molecular Beam Epitaxy Growth of InP/InGaAs Structures for Short Wavelength Infrared Photodetectors”, MSc Thesis, Middle East Technical University, Turkey, 2014.

- [12] P. Chorier, P. M. Trbolet, P. Fillon and A. Manissadjian, “Application Needs and Trade-offs for Short-Wave Infrared Detectors”, *Proceeding - SPIE, The International Society of Optical Engineering*, vol. 5074, pp. 363-373, September 30, 2003.
- [13] H. Martin, “SWIR Imaging: An Industrial Processing Tool”, www.photonics.com. [Last accessed on. 10.05.2016]
- [14] N. K. Dhar, R. Dat and A. K. Sood, “Advances in Infrared Detector Array Technology”, *Optoelectronics - Advanced Materials and Devices*, Chapter 7, INTECH, 2013.
- [15] A. Rogalski, “Infrared Detectors”, Second edition, New York: CRC Press, 2011.
- [16] M. Henini and M. Razeghi, “Handbook of Infrared Detection Technologies”, New York: Elsevier Advanced Technology, 2002.
- [17] W. D. Lawson, S. Nielson, E. H. Putley, and A. S. Young, “Preparation and Properties of HgTe and Mixed Crystals of HgTe-CdTe”, *Journal of Physics and Chemistry of Solids*, vol. 9, pp. 325–329, 1959.
- [18] H. Koçer, “Numerical Modeling and Optimization of HgCdTe Infrared Photodetectors for Thermal Imaging”, Ph. D. Thesis, Middle East Technical University, Turkey, 2011.
- [19] E. C. Piquette, D. D. Edwall, H. Arnold, A. Chen and J. Auyeung, “Substrate-Removed HgCdTe-Based Focal-Plane Arrays for Short-Wavelength Infrared Astronomy”, *Journal of Electronic Materials*, vol. 37, no. 9, pp. 1396-1400, 2008.
- [20] J. Wenisch, D. Eich, H. Lutz, T. Schallenberg, R. Wollrab and J. Ziegler, “MBE Growth of MCT on GaAs Substrates at AIM,” *Journal of Electronic Materials*, vol. 41, no. 10, pp. 2828-2832, 2012.

- [21] www.sensorsinc.com/technology/what-is-ingaas [Last accessed on. 10.05.2016]
- [22] S. Paul, J. B. Roy and P. K. Basu, “Empirical Expressions for the Alloy Composition and Temperature Dependence of the Band Gap and Intrinsic Carrier Density in $\text{Ga}_x\text{In}_{1-x}\text{As}$ ”, *Journal of Applied Physics*, vol. 69, no. 2, pp. 827- 829, 1991.
- [23] A. Rouvie, O. Huet, J. L. Reverchon, J. A. Robo, J. P. Truffer, J. Decobert, E. Costard and P. Bois, “15 μm Pixel-Pitch VGA InGaAs Module for Very Low Background Applications”, *Proceedings of SPIE - The International Society for Optical Engineering*, vol. 8176, pp. 81761A/1-81761A/7, 2011.
- [24] D. Humphreys, R. King, D. Jenkins and A. Moseley, “Measurement of Absorption Coefficients of $\text{Ga}_{0.47}\text{In}_{0.53}\text{As}$ over the Wavelength Range 1.0-1.7 μm ”, *Electronics Letters*, vol. 21, no. 25, pp. 1187-1189, 1985.
- [25] G. H. Olsen and M. J. Cohen, “Applications of Near-Infrared Imaging”, *Proceedings of SPIE - the International Society for Optical Engineering*, vol. 3379, pp. 300-306, 1998.
- [26] B. M. Onat, W. Huang, N. Masaun, M. Lange, M. H. Ettenberg and C. Dries, “Ultra-Low Dark Current InGaAs Technology for Focal Plane Arrays for Low-Light Level Visible-Shortwave Infrared Imaging”, *Proceedings of SPIE – the International Society for Optical Engineering*, vol. 6542, pp. 65420L/1- 65420L/9, 2007.
- [27] C. Li, Y. Zhang, K. Wang, Y. Gua, H. Li, Y. Y. Li, “Distinction Investigation of InGaAs Photodetectors Cut-off at 2.9 μm ”, *Infrared Physics & Technology*, vol. 53, pp. 173–176, 2010.
- [28] R. U. Martinelli, T. J. Zamerowski and P. A. Longeway, “2.6 μm InGaAs Photodiodes”, *Applied Physics Letters*, vol. 53, pp. 989-991, 1988.

- [29] G. H. Olsen, A. M. Joshi, S. M. Mason, K. M. Woodruff, E. Mykiety, V. S. Ban, M. J. Lange, J. Hladky, G. C. Erickson, G. A. Gasparian, "Room-Temperature InGaAs Detector Arrays For 2.5 μm ", *Proceedings of SPIE – the International Society for Optical Engineering, Infrared Technology*, vol. 1157, pp. 276-282, 1990.
- [30] M. D'Hondt, I. Moerman, P. Van Daele, P. Demeester, "Influence of Buffer Layer and Processing on the Dark Current of 2.5 μm -Wavelength 2%-Mismatched InGaAs Photodetectors", *IEEE Proceedings-Optoelectronics.*, vol. 144, no. 5, 1997.
- [31] T. Zhao-Bing, G. Yi, W Kai and Z. Young-Gang, "Gas Source MBE Grown Metamorphic InGaAs Photodetectors Using InAlAs Buffer and Cap-layer with Cut-off Wavelength of up to 2.7 μm ", *Chinese Physics Letters*, vol. 25, pp. 2292-2295, 2008.
- [32] Y. Arslan, F. Oguz, and C. Besikci, "640 \times 512 Extended Short Wavelength Infrared In_{0.83}Ga_{0.17}As Focal Plane Array", *IEEE Journal of Quantum Electronics*, vol. 50, no. 12, pp. 957-964, 2014.
- [33] D. K. Schroder, "Semiconductor Material and Device Characterization", Third edition, John Wiley & Sons, Inc. publication, 2006.
- [34] D. V. Lang. "Deep Level Transient Spectroscopy: A New Method to Characterize Traps in Semiconductors", *Journal of Applied Physics*, vol. 45, pp. 3023-3032, 1974.
- [35] D. V. Lang. "Recalling the origins of DLTS", *Proceedings of the 24th International Conference on Defects in Semiconductors*, vol. 401 and 402, pp. 7–9, 2007.
- [36] P. Blood, J. W. Orton, "The Electrical Characterization of Semiconductors: Majority Carriers and Electron states", Harcourt Brace Jovanovich publishers, 1992.

- [37] P. V. Kolev, "Development and Applications of a New Deep Level Transient Spectroscopy Method and New Averaging Techniques", MSc. Thesis, University of Sofia, 1979.
- [38] M. Razeghi, "Fundamentals of Solid State Engineering", Third Edition, Springer, 2009.
- [39] W. Shockley and W. T. Read, Jr. "Statistics of the Recombination of Holes and Electrons", *Physics Review*, vol. 87, no. 5, pp. 835-842, 1952.
- [40] C. T. Sah, "Fundamentals of Solid-State Electronics", World Scientific Publications, 1992.
- [41] A. Modafe, "Design and Fabrication of Capture Cross-Section Measurement Part of the DLTS Set-up ", MSc Thesis, Iran University of Science and Technology, 1996
- [42] Sula Technology, DLTS system, Tutorial Documents.
- [43] www.sulatech.com [Last accessed on. 10.05.2016]
- [44] Z. Chen, T. Wolf, W. Korb, and D. Bimberg, "Optical and Electrical Characterization of High Resistivity Liquid Phase Epitaxial $\text{In}_{0.53}\text{Ga}_{0.47}\text{As:Fe}$ ", *Journal of Applied Physics*, vol. 64, pp. 45-74, 1988.
- [45] Y. Lee, J. S. Kim, E. K. Kim, S. H. Pyun and W. G. Jeong, "DLTS Study of InGaAs/InGaAsP Double-Layered QDs with Various Spacer Layers", *Journal of the Korean Physical Society*, vol. 55, no. 3, pp. 1041-1045, 2009.
- [46] M. Sugawara, M. Kondo, T. Takanohashi, and K. Nakajima, "Fe Acceptor Level in $\text{In}_{1-x}\text{Ga}_x\text{As}_y\text{P}_{1-y}/\text{InP}$ ", *Applied Physics Letters*, vol. 51, pp. 834-842, 1987.
- [47] G. Guillot, G. Bremond, T. Benyattou, F. Ducroquet, B. Wirth, M. Colombet, A. Louati, and A. Bencherifa, "Identification of the Fe Acceptor

- Level in $\text{Ga}_{0.47}\text{In}_{0.53}\text{As}$ ”, *Semiconductor Science and Technology*, vol. 5, pp. 391-394, 1990.
- [48] A. E. Kowalczyk, L. Ornoch, J. Muszaalski, J. Kaniewski, J Bak-Misiuk, “Deep Centers in InGaAs/InP Layers Grown by Molecular Beam Epitaxy”, *Optica Applicata*, vol. 35, no. 3, pp. 457-463, 2005.
- [49] A. C. Irvine and D. W. Palmer, “First Observation of the EL2 Lattice Defect in Indium Gallium Arsenide Grown by Molecular-Beam Epitaxy”, *Physical Review Letters*, vol. 68, no. 14, pp. 2168-2171, 1992.
- [50] R. V. Lang, J. D. Leslie, J. B. Webb, A. P. Roth, M. A. Sacilotti, and R. A. Masut, “Deep-Level Transient Spectroscopic Investigation of the EL2 Deep-Level in Metalorganic Chemical Vapour Deposited $\text{Ga}_{1-x}\text{In}_x\text{As}$ Epilayers” *Canadian Journal of Physics*, vol. 67, pp. 283-286, 1989.
- [51] A. Mircea, A. Mitonneau, J. Hallais, and M. Jaros, “Study of the Main Electron Trap in $\text{Ga}_{1-x}\text{In}_x\text{As}$ alloys”, *Physics Review B*, vol. 16, pp. 3665-3675, 1977.
- [52] R. Trommer and H. Albrecht, “Confirmation of Tunnelling Current via Traps by DLTS Measurement in InGaAs Photodiodes”, *Japanese Journal of Applied Physics*, vol. 22, part 2, no. 6, 1983.
- [53] Z. Chen, W. Korb, R. K. Bauer, and D. Bimberg, “First Observation of a Titanium Midgap Donor Level in $\text{In}_{0.53}\text{Ga}_{0.47}\text{As}$ p-n Diodes”, *Applied Physics Letters*, vol. 55, pp. 645-647, 1989.
- [54] T. H. Gfroerer, K. R. Simov, and M. W. Wanlass, “Observation of an Anomalous Minority Carrier Trap in n-type InGaAs”, *International Conference on Indium Phosphide and Related Materials*, pp. 657-659, 2005.

- [55] W. Schroter, J. Kronewitz, U. Gnauert, F. Riedel, and M. Seibt, “Bandlike and Localized States at Extended Defects in Silicon”, *Physical Review B*, vol. 52, no. 19, pp. 13726-13729, 1995.
- [56] P. Omling, L. Samuelson, and H. G. Grimmeiss, “Deep Level Transient Spectroscopy Evaluation of Non-Exponential Transients in Semiconductor Alloys”, *Journal of Applied Physics*, vol. 54, no. 9, pp. 5117-5122, 1983.
- [57] P. Omling, E.R. Weber, L. Montelius, H. Alexander and J. Michel, “Electrical Properties of Dislocations and Point Defects in Plastically Deformed Silicon”, *Physical Review B*, vol. 32, pp. 6571-6581, 1985.
- [58] D. Cavalcoli, A. Cavallini, E. Gombia, “Energy Levels Associated with Extended Defects in Plastically Deformed n-Type Silicon”, *Journal de Physique III, EDP Sciences*, vol. 7, pp. 1399-1409, 1997.
- [59] L. Gelczuk, M. Dąbrowska-szata, G. Jozwiak, “Distinguishing and Identifying Point and Extended Defects in DLTS Measurements”, *Materials Science-Poland*, vol. 23, no. 3, pp. 625-641, 2005.
- [60] G. P. Watson, D. G. Ast, T. J. Anderson, B. Pathaney, and Y. Hayakawa “The Measurement of Deep Level States Caused by Misfit Dislocations in InGaAs/GaAs Grown on Patterned GaAs Substrates”, *Journal of Applied Physics*, vol. 71, pp. 3399-3407, 1992.
- [61] L. Panepinto, U. Zeimerb, W. Seifertc, M. Seibt, F. Buggeb, M. Weyersb, W. Schrijter, “Temperature Dependent EBIC And Deep Level Transient Spectroscopy Investigation of Different Types of Misfit-Dislocations at MOVPE Grown GaAs/InGaAs/GaAs Single-Quantum Wells”, *Materials Science and Engineering B*, vol. 42, pp. 77-81, 1996.
- [62] D. Pal, E. Gombia, R. Mosca, A. Bosacchi, and S. Franchi, “Deep Levels in Virtually Unstrained InGaAs Layers Deposited on GaAs”, *Journal of Applied Physics*, vol. 84, no. 5, pp. 2965-2967, 1998.

- [63] T Wosinski, O Yastrubchak, A Makosa and T Figielski, “Deep-level Defects at Lattice-Mismatched Interfaces in GaAs-Based Heterojunctions”, *Journal of Physics: Condens. Matter*, vol. 12, pp. 10153–10160, 2000.
- [64] L. Gelczuk, M. Dabrowska-Szata, G. Jozwiak and D. Radziewicz, “Misfit Dislocations Study in MOVPE Grown Lattice-Mismatched InGaAs/GaAs Heterostructures by Means of DLTS Technique”, *Proceedings of the XXXIII International School of Semiconducting Compounds*, vol. 106, pp. 265-272, Jaszowiec, 2004.
- [65] L. Gelczuk, M. Dabrowska-Szata,, G. Jozwiak, D. Radziewicz, J. Serafinczuk and P. Duzewski, “Dislocation-Related Electronic States in Partially Strain-Relaxed InGaAs/GaAs Heterostructures Grown by MOVPE”, *Physica Status Solidi (c)*, vol. 4, no. 8, pp. 3037–3042, 2007.
- [66] L. Gelczuk, M. Dabrowska-szata, “Modification of Energy Bandgap in Lattice Mismatched InGaAs/GaAs Heterostructures”, *Optica Applicata*, vol. XXXIX, no. 4, pp. 845-852, 2009.
- [67] X. D. Wang, W. D. Hu, X. S. Chen, W. Lu, H. J. Tang, T. Li, and H. M. Gong, “Dark Current Simulation of InP/InGaAs/InP p-i-n Photodiode”, *Optical and Quantum Electronics*, vol. 40, pp. 1261-1266, 2008.
- [68] K. R. Linga, G. H. Olsen, V. S. Ban, A. M. Joshi, and W. F. Kosonocky, “Dark Current Analysis and Characterization of $\text{In}_x\text{Ga}_{1-x}\text{As}/\text{InAs}_y\text{P}_{1-y}$ Graded Photodiodes with $x > 0.53$ for Response to Longer Wavelengths ($> 1.7\mu\text{m}$)”, *Journal of Lightwave Technology*, vol. 10, no. 8, pp. 1050-1055, 1992.
- [69] H. J. Byron, “Molecular-beam epitaxial growth of low-dark-current avalanche photodiodes”, Ph. D. Dissertation, The University of Texas at Austin, 2007.